

UCSF

UC San Francisco Electronic Theses and Dissertations

Title

Hyperpolarized ^{13}C Magnetic Resonance Spectroscopic Imaging: Pulse Sequence Development for Compressed Sensing Rapid Imaging and Preclinical Liver Studies

Permalink

<https://escholarship.org/uc/item/4c574316>

Author

Hu, Simon

Publication Date

2009

Peer reviewed|Thesis/dissertation

Hyperpolarized ^{13}C Magnetic Resonance Spectroscopic Imaging: Pulse Sequence
Development for Compressed Sensing Rapid Imaging and Preclinical Liver Studies

by

Simon Hu

DISSERTATION

Submitted in partial satisfaction of the requirements for the degree of

DOCTOR OF PHILOSOPHY

in

Bioengineering

in the

GRADUATE DIVISION

of the

UNIVERSITY OF CALIFORNIA, SAN FRANCISCO

Acknowledgments

First and foremost, I owe a tremendous portion of my success in graduate school to my advisor, Dan Vigneron, from whom I've learned almost everything I know about conducting scientific research. Without his guidance and encouragement, I would not have been able to accomplish the amount of science that I did over the past few years. I must also thank all the talented people who have helped and worked with me on hyperpolarized carbon-13 research. They are almost too numerous to list, but here goes ...

From the UCSF Radiology labs: Peder Larson for helping me with pulse sequence design, EPIC, and experiments and for being helpful and patient in general, Robert Bok for his saintly patience in teaching me about biology and helping me with animal experiments, Mark Van Crieking for teaching me about the polarizer and keeping it working, Kristen Scott for all the hours put in on animal experiments, Jenny Che for being the most helpful administrative assistant ever, Cornelius von Morze for assisting with experiments, Lucas Carvajal for discussions on coils/physics and for help fixing coils, Jason Crane for help with reconstructions and processing, Dave Wilson for preparing and debugging chemical preparations, Ilwoo Park for discussions on animal experiments, Paniz Vafaei for doing biochemical assays, Lynn DeLosSantos for preparing histology, Dave Joun and Hikari Yoshihara for agent preparation help, Duan Xu for assisting with experiments and for general lab help, Hagit Dafni for discussions on experimental procedures, Kayvan Keshari and Mark Albers for discussions on metabolism, Rahwa Iman for running NMR

samples, Matt Zierhut for discussions on modeling enzyme kinetics, Galen Reed for assisting with experiments, Peter Shin for assisting with experiments, Sri Veeraraghavan for assisting with experiments and for computer help, Albert Chen for his attention to detail, Vickie Zhang for assisting with experiments, and John Kurhanewicz, Sabrina Ronen, and Sarah Nelson for serving on my quals committee and for many helpful suggestions ...

From Stanford University: Miki Lustig for his many wonderful ideas during our collaboration on the compressed sensing projects, Adam Kerr for many very useful discussions on pulse sequences and for helping me figure out a tricky pulse sequence bug in my first carbon-13 project, and John Pauly for many helpful discussions and all the great classes I've taken from him ...

From the Goga Lab at UCSF: Asha Balakrishnan for helpful discussions and tending to many details on the liver cancer project and Andrei Goga for serving on my quals committee, helpful discussions, and being a great collaborator on the liver cancer project ...

And from GE Healthcare: Doug Kelley for many helpful discussions on the GE MRI system, Jim Tropp for many fascinating discussions on physics and for building and fixing all the coils I've used, Yi-Fen Yen for help with hyperpolarized basics when I was starting out, and Ralph Hurd for many helpful discussions and insights.

The amount of collaboration in my projects has been staggering and truly invaluable, as attested to by all the specific things each person listed above has done to help my research and accelerate the completion of my Ph.D. Finally, this

manuscript is dedicated to my loving parents, Senqi and Jin-Di, without whom none of my accomplishments in science or life would be possible.

Zhong-Min (Simon) Hu

October 1, 2009

Abstract

The use of *in vivo* ^{13}C nuclear magnetic resonance spectroscopy to probe metabolic pathways for the study of normal and disease physiology has traditionally been limited by low sensitivity. However, recent technological advances utilizing dynamic nuclear polarization have enabled on the order of 50,000-fold enhancement of liquid-state polarization of metabolically active ^{13}C substrates, allowing for rapid imaging detection of their metabolism *in vivo*. A key design challenge, though, for this type of metabolic imaging is the rapid decay associated with the hyperpolarized signal, which necessitates fast imaging strategies for optimal speed and spatial coverage. Through this dissertation research, a new random undersampling approach—compressed sensing—was applied for the first time to hyperpolarized MR imaging. An initial blipped, random undersampling pulse sequence was developed to enable 2-fold accelerated imaging. Subsequently, enhancements to the pulse sequence were developed to achieve ~7.5-fold acceleration, and the limits of undersampling with and without noise were explored in simulations. Numerous potential applications exist for hyperpolarized ^{13}C spectroscopic imaging, among which include studying normal liver metabolism and characterizing diseased liver physiology. In this work, hyperpolarized ^{13}C technology was used to detect a change in liver metabolic state for the first time, demonstrating decreased hyperpolarized alanine in fasted rat liver *in vivo*. Then in novel preclinical work, changes in hyperpolarized lactate and alanine were investigated in disease progression and regression studies with transgenic liver

cancer mice, demonstrating the potential for future patient studies with hyperpolarized ^{13}C spectroscopic imaging.

Table of Contents

1	Introduction	1
2	Background	5
	2.1 Fundamentals of Magnetic Resonance Imaging	5
	2.1.1 Spin, Magnetic Moment, Magnetization Vector, and Polarization	5
	2.1.2 Magnetization Vector Dynamics	8
	2.1.3 k-space Description of Signal Reception	12
	2.1.4 RF Excitation	17
	2.2 Fundamentals of Magnetic Resonance Spectroscopic Imaging	19
	2.2.1 Chemical Shift	19
	2.2.2 k-space Interpretation of Chemical Shift Imaging	21
	2.3 DNP Hyperpolarization	23
	2.3.1 Past and Recent Work on DNP	23
	2.3.2 Metabolic Pathways Probed with DNP Hyperpolarized ^{13}C -pyruvate	25
	2.3.3 Clinical Significance	26
3	An Initial Compressed Sensing Design for Hyperpolarized ^{13}C MRSI	28
	3.1 Background and Theory	28
	3.1.1 Motivation	28
	3.1.2 Existing Pulse Sequence	30
	3.1.3 Key Results from Compressed Sensing Literature	31
	3.1.4 3D-MRSI Signal	33
	3.2 Methods	35
	3.2.1 Pulse Sequence Development for 2-fold Acceleration	35
	3.2.2 Pulse Sequence and Hardware	38
	3.2.3 Reconstruction	39
	3.2.4 Phantom Methodology	40
	3.2.5 <i>In vivo</i> Methodology	41
	3.3 Results and Discussion	42
	3.3.1 Phantom Results	42
	3.3.2 <i>In Vivo</i> Results	45
	3.3.3 Limitations and Future Work	49
	3.3.4 Conclusion	50
4	<i>In Vivo</i> Carbon-13 Dynamic MRS and MRSI of Normal and Fasted Rat Liver with Hyperpolarized ^{13}C -Pyruvate	51
	4.1 Background	51
	4.2 Methods	55
	4.2.1 Overview	55
	4.2.2 Polarizer and Preparations	55
	4.2.3 Animal Handling	56
	4.2.4 MRI, MRS, and MRSI	56
	4.2.5 Data Processing	58
	4.3 Results	60
	4.3.1 Dynamic MRS of Normal and Fasted Rat Liver	60

4.3.2	3D-MRSI of Normal and Fasted Rat Liver	63
4.4	Discussion	67
5	Extensions to Compressed Sensing Hyperpolarized ^{13}C Rapid MRSI	71
5.1	Background and Theory	71
5.1.1	Motivation	71
5.1.2	Compressed Sensing Literature	73
5.1.3	Hyperpolarized Carbon-13 Signal	75
5.1.4	Simulation 1: Limits of Undersampling without Noise	75
5.1.5	Simulation 2: Reconstruction with Noise	79
5.2	Methods	82
5.2.1	Pulse Sequence Design for Highly Accelerated 3D-MRSI	82
5.2.2	Pulse Sequence and Hardware	85
5.2.3	Reconstruction Methodology	86
5.2.4	Phantom Methodology	87
5.2.5	<i>In Vivo</i> Methodology	87
5.3	Results	89
5.3.1	Phantom Results	89
5.3.2	<i>In Vivo</i> Results	89
5.4	Discussion	95
5.4.1	Compressed Sensing	95
5.4.2	Parameters for Human Studies	96
5.4.3	Other Accelerated Imaging Extensions and Approaches	98
5.4.4	Summary	98
6	<i>In Vivo</i> Assessment of Disease Progression and Regression in a MYC Transgenic Mouse Model of Liver Cancer Using Hyperpolarized ^{13}C MRSI	100
6.1	Background	100
6.2	Methods	104
6.2.1	Mouse Tumor Model	104
6.2.2	DNP and Injection of Hyperpolarized Pyruvate	104
6.2.3	MRI and MRSI	105
6.2.4	Liver Histology and Immunohistochemistry	106
6.2.5	LDH Expression	107
6.2.6	LDH Activity	107
6.2.7	Statistical Analysis	108
6.3	Results	109
6.3.1	3D-MRSI of Disease Progression	109
6.3.2	3D-MRSI of Disease Regression	113
6.3.3	Progression and Regression Data over All Mice	115
6.3.4	Histology and Immunohistochemistry	116
6.3.5	LDH Expression and Activity	118
6.4	Discussion	120
6.4.1	Advantages of Hyperpolarized Technology	120
6.4.2	Biomarkers	121
6.4.3	Future Work and Prospects	126
7	Application of HSn Low Peak B_1 Adiabatic Refocusing Pulses to Hyperpolarized ^{13}C Spectroscopic Imaging	129

7.1 Background	129
7.2 Methods	130
7.2.1 Pulse Design and Validation	130
7.2.2 C-13 Phantom and <i>In vivo</i> Validation with Animal Coils	132
7.2.3 Validation with Clinical Coil/Amplifier Configuration	133
7.3 Results	134
7.3.1 C-13 Phantom	134
7.3.2 Mouse	134
7.3.3 Volunteer	136
7.4 Discussion	137
8 Summary	138
9 References	140

List of Figures

Figure 2.1	Orientation of Spins	7
Figure 2.2	Precession and Relaxation	9
Figure 2.3	Gradient Magnetic Field	13
Figure 2.4	Coverage of k -space	16
Figure 2.5	RF Excitation	18
Figure 2.6	Chemical Shift	20
Figure 2.7	NMR/MRS Spectrum	21
Figure 2.8	k_x - k_y - k_f Space	22
Figure 2.9	Base Hyperpolarized Pulse Sequence	24
Figure 2.10	Metabolic Pathways Probed	26
Figure 3.1	Double Spin-echo Pulse Sequence	31
Figure 3.2	Wavelet Compressibility of a ^{13}C Signal	34
Figure 3.3	Blipped Scheme for k_f - k_x Sub-Sampling	36
Figure 3.4	Blipped Patterns and Coverage	37
Figure 3.5	Normal/Undersampled Phantom Data	44
Figure 3.6	Normal/Undersampled <i>In Vivo</i> Data	46
Figure 4.1	Metabolic Pathways Investigated	53
Figure 4.2	Quantification Procedures for MRS/MRSI	59
Figure 4.3	Normal/Fasted Rat Liver Dynamic Data	61
Figure 4.4	Lactate/Alanine Ratios for Dynamic Data	62
Figure 4.5	Normal/Fasted Rat Liver 3D-MRSI Data	64
Figure 4.6	Lactate/Alanine Ratios for 3D-MRSI Data	65
Figure 4.7	Lactate and Alanine to Total Carbon	66
Figure 5.1	Compressed Sensing Undersampling Simulations	77
Figure 5.2	Compressed Sensing Noise Simulations	80
Figure 5.3	Highly Accelerated Pulse Sequence Design	83
Figure 5.4	Compressed Sensing Phantom Results	90
Figure 5.5	Validation with Prostate Cancer Mice	91
Figure 5.6	Validation with Liver Cancer Mice	94

Figure 6.1	MYC Model Disease Progression	110
Figure 6.2	Alternate Visualization of MRSI Data	112
Figure 6.3	MYC Model Disease Regression	114
Figure 6.4	MYC Progression/Regression Data for All Mice	115
Figure 6.5	MYC Histology and Immunohistochemistry	117
Figure 6.6	LDH Activity and Expression in MYC Mice	119
Figure 6.7	Effect of MCT Inhibitor 4-CIN	125
Figure 7.1	HSn Adiabatic Pulse Design	131
Figure 7.2	Human ¹³ C Coil Configuration	134
Figure 7.3	HSn Adiabatic Phantom Data	135
Figure 7.4	HSn Adiabatic Mouse Data	135
Figure 7.5	HSn Adiabatic Volunteer Data	136

List of Tables

Table 2.1	Natural Abundance and Gyromagnetic Ratios	7
Table 3.1	Quantification of Normal/Undersampled Phantom Data	43
Table 3.2	Quantification of Normal/Undersampled <i>In Vivo</i> Data	48
Table 6.1	Histology and Immunohistochemistry of MYC Mice	121
Table 6.2	Pyruvate Uptake Inhibition with 4-CIN	125

Chapter 1: Introduction

Since its introduction over three decades ago, magnetic resonance imaging (MRI) has advanced tremendously, becoming an extremely powerful and very common medical imaging modality. The clinical uses for a typical MRI scanner are quite numerous, and in broad terms, they include anatomical imaging, angiography, diffusion mapping, functional brain imaging, guided intervention, and spectroscopic imaging, to name a few. The disease application areas are just as wide-ranging—cancers of various organs, neurodegenerative disease, cardiovascular disease, sports injuries, hepatobiliary disease, and so forth. Magnetic resonance spectroscopy/spectroscopic imaging (MRS/MRSI), which allows for the non-invasive assessment of metabolite concentrations in tissue, is among the many areas that continues to be actively researched, both in terms of technical development and applications. The general topic of this dissertation is hyperpolarized ^{13}C MRS and MRSI, a new area of bioengineering research that has great potential for eventual clinical applications.

Anatomical images produced by MRI are based on detecting proton signals primarily from water molecules in the body, which are quite abundant considering that the majority of the human body is composed of water. Proton MRSI, on the other hand, detects proton signals from non-water, cellular metabolites, which are far less abundant. In spite of this inherent signal-to-noise ratio (SNR) disadvantage, proton MRSI can differentiate normal and diseased tissues, such as cancer, based on their differing biochemical profiles. Traditional carbon MRSI, which detects carbon-

^{13}C signals and has the potential to probe a wider range of metabolites, suffers from even lower SNR due to a lower gyromagnetic ratio and only 1.1% natural abundance of the MR detectable ^{13}C isotope. However, a recent technological breakthrough—using dynamic nuclear polarization (DNP) and thermal cooling to hyperpolarize ^{13}C substrates in solid state and maintaining that hyperpolarization into the liquid state through a rapid dissolution process—has generated great excitement for the prospect of rapid, high SNR (~50,000-fold improvement over traditional ^{13}C MRSI) measurement of ^{13}C metabolism *in vivo*. In other words, metabolic substrates can be pre-polarized in solid state and then dissolved for *in vivo* injection to monitor uptake and metabolic conversion. Details on hyperpolarized technology and its applications, as well as general background on the fundamentals of MRI and MRSI, are given in Chapter 2.

The scientific work presented in this dissertation adds to the relatively brief current literature on hyperpolarized ^{13}C imaging. My dissertation includes four main contributions, organized chronologically in Chapters 3, 4, 5, and 6, each of which is a minor adaptation of either an already published, peer-reviewed manuscript or one in the process of being published. In Chapter 3, the topic is an initial pulse sequence design for the application of compressed sensing to hyperpolarized ^{13}C MRSI. A key design challenge for hyperpolarized imaging is the rapid decay associated with the hyperpolarized signal, which necessitates fast imaging strategies for optimal speed and spatial coverage. My approach was to apply compressed sensing, a relatively new mathematical technique based on random undersampling and a non-linear reconstruction. This entailed designing a

novel, blipped pulse sequence to accomplish random undersampling and testing it in phantoms followed by initial validation with animal studies. In Chapter 4, I describe the application of hyperpolarized MRS/MRSI to the liver, specifically demonstrating that hyperpolarized technology can detect a change in liver metabolism as shown by changes observed in normal versus fasted rat liver. Ultimately, hyperpolarized ^{13}C MRSI of the liver could be especially advantageous because of the ability to acquire rapid, breath-held assessment of metabolism. In Chapter 5, the topic of compressed sensing hyperpolarized ^{13}C MRSI is revisited, and I describe pulse sequence enhancements to significantly accelerate imaging as well as simulations to investigate the limits of undersampling. In Chapter 6, another application of hyperpolarized ^{13}C MRSI to the liver is presented. Transgenic mice in which the human MYC oncogene could be switched on and off in the liver were used for progression and regression studies in which the efficacy of hyperpolarized biomarkers for monitoring liver cancer was shown. The MYC oncogene has a critical role in cell cycle control and is dysregulated in many subtypes of liver cancer. MYC also acts as a transcription factor for many pro-growth enzymes, including lactate dehydrogenase (LDH). As described later, the hyperpolarized agent $[1-^{13}\text{C}]$ pyruvate probes LDH activity; thus, there is a direct link between an important liver cancer subtype and a hyperpolarized biomarker. In Chapter 7, I show how adiabatic refocusing pulses used in animal studies were redesigned to have the lower peak power values required for human applications. Finally, in Chapter 8, I conclude by giving a summary of the technique development and preclinical liver applications

presented in this dissertation and discuss clinical prospects and future directions for hyperpolarized ^{13}C technology.

Chapter 2: Background

Although nuclear magnetic resonance (NMR) and spin dynamics are fundamentally quantum mechanical phenomena, the classical description suffices for understanding all the work presented in this dissertation. Thus, for the sake of expediency, almost no mention of quantum mechanics will be made here. The interested reader is referred to texts that describe NMR and MRI from a quantum mechanical perspective (1,2). This chapter focuses on the MRI/MRS background, particularly the idea of “*k*-space”, necessary for understanding the compressed sensing pulse sequence development in Chapters 3 and 5. Detailed explanation of other aspects, including hardware and advanced radiofrequency (RF) pulse design, will not be given. Again, the interested reader is referred to other sources (3-5). Following the background on MRI/MRSI is an introduction to current DNP hyperpolarized technology, focusing mainly on practical aspects. Then a discussion of the metabolic pathways probed with DNP hyperpolarized technology and their physiological and medical significance is given.

2.1 Fundamentals of Magnetic Resonance Imaging

2.1.1 Spin, Magnetic Moment, Magnetization Vector, and Polarization

All elementary particles, e.g. quarks, possess a fundamental property called “spin”. Thus, protons and neutrons, which are made from quarks, also possess spin. Nuclei with an odd number of protons and/or an odd number of neutrons (e.g. ^1H

with 1 proton, ^2H with 1 proton + 1 neutron, ^{13}C with 6 protons + 7 neutrons, ^{31}P with 15 protons + 16 neutrons) have non-zero spin (1). Associated with non-zero spin is a dipole magnetic moment $\boldsymbol{\mu}$. As illustrated in Figure 2.1a, at thermal equilibrium, the magnetic moments are oriented randomly and have no net magnetization. However, when a static magnetic field \mathbf{B} (typically uniform throughout a large volume) is applied, the magnetic moments preferentially align with the field to create a net magnetization vector $\mathbf{m} = \sum \boldsymbol{\mu}$ (Figure 2.1b). The potential energy of a magnetic moment in the static magnetic field is given by:

$$E = -\boldsymbol{\mu} \cdot \mathbf{B} \quad [2.1]$$

The energy difference (Figure 2.1c) between the lowest energy configuration ($\boldsymbol{\mu}$ parallel to \mathbf{B}) and the highest energy configuration ($\boldsymbol{\mu}$ antiparallel to \mathbf{B}) is given by:

$$\Delta E = h \frac{\gamma}{2\pi} B_0 \quad [2.2]$$

where h is Planck's constant, B_0 is the strength of the static magnetic field in units of Tesla, and γ is the gyromagnetic ratio, a unique constant for each isotope (5). Table 2.1 below lists γ for several isotopes.

At a specific temperature T (in Kelvin), the ratio of magnetic moments in the antiparallel (N_-) to parallel (N_+) populations is given by:

$$\frac{N_-}{N_+} = e^{-\frac{\Delta E}{kT}} \quad [2.3]$$

where k is Boltzmann's constant (5).

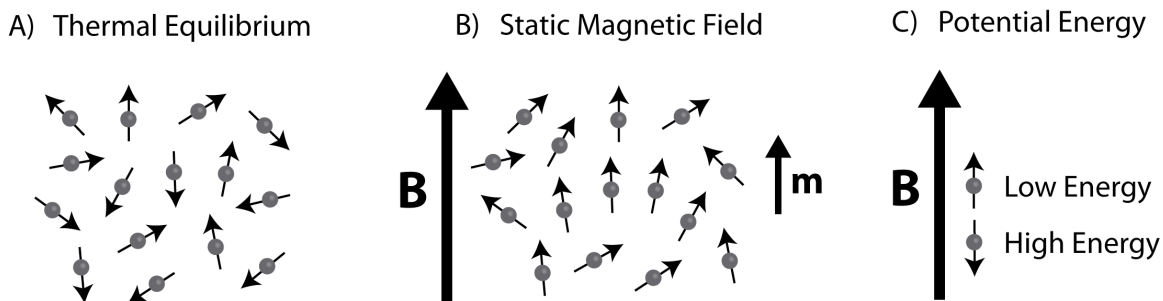


Figure 2.1: A) Spins are oriented randomly at thermal equilibrium. B) When a static magnetic field is applied, there is a net magnetization vector \mathbf{m} . C) The lowest energy configuration for the dipole magnetic moment is parallel with \mathbf{B} .

Table 2.1: Natural abundance, gyromagnetic ratio, and NMR (Larmor) frequency at 3T for several isotopes commonly observed with NMR and MRI.

Isotope	Natural Abundance	Gyromagnetic Ratio ($\text{rad s}^{-1} \text{T}^{-1}$)	NMR (Larmor) Frequency at $B_0 = 3\text{T}$ (MHz)
^1H	~100%	267.522×10^6	127.732
^2H	0.015%	41.066×10^6	19.608
^{13}C	1.1%	67.283×10^6	32.125
^{19}F	~100%	251.815×10^6	120.233
^{23}Na	~100%	70.808×10^6	33.808
^{31}P	~100%	108.394×10^6	51.754

If polarization is defined as the following, in other words the proportion of excess spins in the lower energy configuration:

$$P = \frac{N_+ - N_-}{N_+ + N_-} \quad [2.4]$$

then combining equations [2.3] and [2.4] gives:

$$P = \frac{e^{\frac{\Delta E}{kT}} - 1}{e^{\frac{\Delta E}{kT}} + 1} \quad [2.5]$$

Using Eqn. [2.5], then at body temperature (310 K) and at a magnetic field of 3T, the polarization for ^{13}C is 2.49×10^{-6} , meaning that out of a million spins, only a few more are parallel to the magnetic field than antiparallel. This small effect is the basis for the net magnetization vector and detected signal in MRI. The polarization for ^1H , at 9.88×10^{-6} , is better, yet still small; however, there is such a high concentration of water molecules in the human body that proton MRI enjoys relatively high SNR. As described in a later section, polarization for ^{13}C can be dramatically enhanced through a combination of dynamic nuclear polarization and thermal cooling.

2.1.2 Magnetization Vector Dynamics

As mentioned in the previous section, the net magnetization vector \mathbf{m} , which lines up with \mathbf{B} , is the basis for the MRI signal. The following is a discussion of the dynamics of \mathbf{m} . If, somehow, \mathbf{m} were made to point away from \mathbf{B} , then precession of \mathbf{m} about \mathbf{B} occurs (Figure 2.2a). This precession can be described succinctly by:

$$\frac{d\mathbf{m}}{dt} = \mathbf{m} \times \gamma \mathbf{B} \quad (5) \quad [2.6]$$

The solution to Eqn. [2.6] is for \mathbf{m} to precess (rotate) around \mathbf{B} with an angular frequency (Larmor frequency, See Table 2.1) of:

$$\omega_0 = \gamma B_0 \quad \text{rad/s} \quad (1,5) \quad [2.7]$$

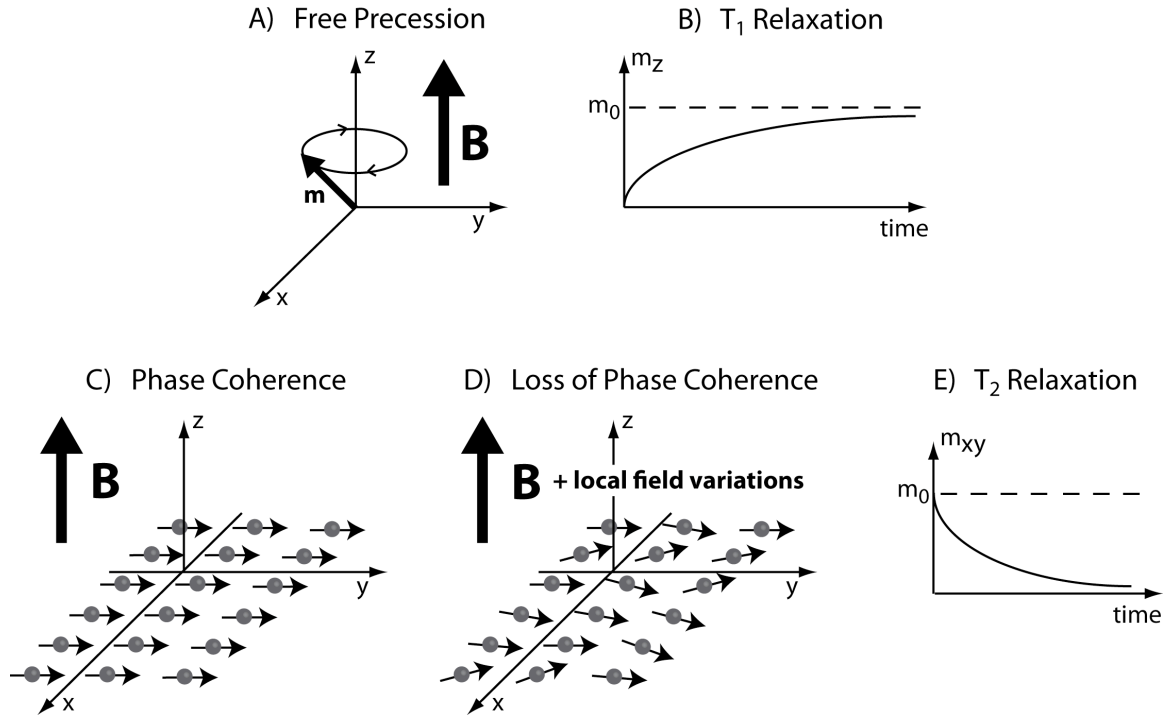


Figure 2.2: Precession and relaxation. A) When tipped from the z-axis, the magnetization vector precesses about the static magnetic field direction (z-axis). B) After being tipped away from the z-axis, the magnetization along z gradually returns (T_1 relaxation). C) Without local variations in magnetic field, all spins in a volume precess at the same rate and have phase coherence. D) Dephasing occurs when there are local variations in magnetic field. E) The dephasing is referred to as T_2 relaxation.

As shown in Eqn. [2.7] and Table 2.1, each nucleus, having its own unique γ , has its own unique frequency of precession. A later section will describe how \mathbf{m} can be tipped away from \mathbf{B} and cause this sort of precession. In the coordinate system of Figure 2.2, the magnetization is originally along +z, i.e. only has an m_z component.

After tipping it away from +z, m_x and m_y components appear. Notationally, these two components can be conveniently written as a complex number:

$$m_{xy} = m_x + im_y \quad [2.8]$$

Two other dynamic phenomena will be discussed. The first is T_1 relaxation. It is also called longitudinal relaxation and spin-lattice relaxation. After \mathbf{m} is tipped away from the +z axis, the remaining m_z component is less than the original magnetization along +z, which is denoted m_0 . However, m_z recovers exponentially back to m_0 over time according to:

$$\frac{dm_z}{dt} = -\frac{m_z - m_0}{T_1} \quad (5) \quad [2.9]$$

The solution to Eqn. [2.9] is:

$$m_z(t) = m_0 + (m_z(0) - m_0)e^{-t/T_1} \quad (5) \quad [2.10]$$

Eqn. [2.10] shows that after a sufficiently long time, i.e. $t \rightarrow \infty$, m_z returns to m_0 .

Figure 2.2b shows the time course of m_z after \mathbf{m} has been completely tipped into the transverse plane. The relaxation constant T_1 in Eqns. [2.9] and [2.10] is thus related to how the magnetization returns to its thermal equilibrium value. The precise physical mechanisms behind T_1 relaxation are quite complex, and the interested reader is referred to more in-depth treatments of the subject (1,2). For practical purposes, T_1 can be regarded as a constant to be empirically determined for each molecule studied. It varies depending on the type of nucleus, the position within a molecule, and the biological environment. The T_1 s of protons in water molecules are typically around 0.5-1 seconds depending on the tissue type. The T_1 s for the carbon

atoms studied with hyperpolarized ^{13}C MRS/MRSI are about 30-60 seconds. The significance of this disparity will be discussed later.

The other dynamic phenomenon is T_2 relaxation, also called transverse relaxation and spin-spin relaxation. T_2 relaxation is simpler to understand and can be thought of as a destructive interference phenomenon. As indicated by Figure 2.2a and Eqns. [2.6] and [2.7], the behavior of the magnetization vector is to precess about the z-axis. When \mathbf{m} is decomposed into m_z and m_{xy} , one sees that it is actually the m_{xy} component that rotates about z. Per unit volume, there are countless tiny magnetization vectors, one for each molecule in the volume. As shown in Figure 2.2c, ideally all the tiny magnetization vectors precess at the same rate because they are all under the influence of the same main magnetic field (Eqn. [2.7]). Thus, the m_{xy} signal detected from such a volume would be the constructive sum of all the tiny magnetization signals. However, if small variations in the magnetic field occur within the volume, then as shown by Figure 2.2d, the individual magnetization vectors would not precess at exactly the same rate and would eventually lose phase coherence. m_{xy} would decrease in signal amplitude as shown in Figure 2.2e and change over time according to:

$$\frac{dm_{xy}}{dt} = -\frac{m_{xy}}{T_2} \quad (5) \quad [2.11]$$

The solution to Eqn. [2.11] is:

$$m_{xy}(t) = m_0 e^{-t/T_2} \quad (5) \quad [2.12]$$

Thus, T_2 is an exponential time constant related to magnetic field inhomogeneity.

Combining the effects of precession (Eqn. [2.6]), longitudinal relaxation (Eqn. [2.9]), and transverse relaxation (Eqn. [2.11]) gives the Bloch equation:

$$\frac{d\mathbf{m}}{dt} = \mathbf{m} \times \gamma \mathbf{B} - \frac{m_x \hat{x} + m_y \hat{y}}{T_2} - \frac{(m_z - m_0) \hat{z}}{T_1} \quad [2.13]$$

The Bloch equation is a phenomenological description of magnetization vector dynamics and is extremely valuable for understanding MRI.

2.1.3 *k*-space Description of Signal Reception

As mentioned above, in MRI, only the m_{xy} component of \mathbf{m} is detected. In a volume such as the one shown in Figure 2.2c, the detected signal is the summation:

$$s_r(t) = \int_x \int_y \int_z m_{xy}(x, y, z, t) dx dy dz \quad (5) \quad [2.14]$$

Note that the integrand in Eqn. [2.14] does not include the time varying precession factor (written as a complex number $e^{-i\omega_0 t}$) because it is assumed that the magnetization signal is demodulated to baseband before detection. Of course, the magnetization density varies over space according to biological environment, which is the type of change MRI detects, but Eqn. [2.14] does not reflect this local spatial distribution. In order to capture local variations in m_{xy} , i.e. to create a spatial image based on magnetization differences, a trick is needed. Figure 2.3 illustrates the use of a gradient magnetic field on top of the main B_0 field to create intentional spatial variations in magnetic field to achieve spatial localization. As shown in Figure 2.3a, in the presence of only the B_0 field, which does not vary spatially, all magnetization vectors over x precess at the same rate. When a small B_z field that varies along the x direction (Figure 2.3b) is applied (an x -gradient), a variation in precession along the

x direction occurs (5). In other words, the gradient field changes the local resonance frequencies according to:

$$\omega(x) = \gamma B_0 + \gamma x G_x \quad (5) \quad [2.15]$$

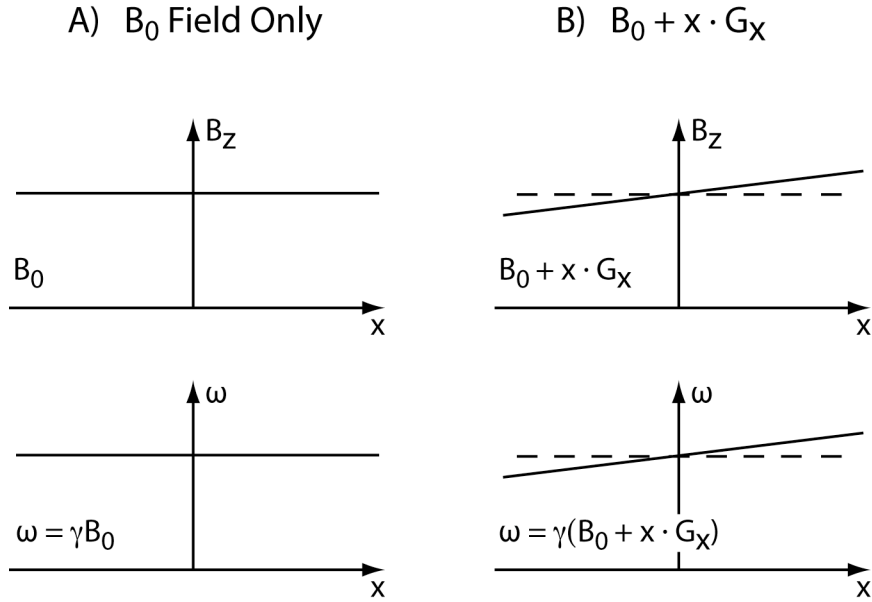


Figure 2.3: A) When only the main magnetic field is present, all spins across x precess at the same frequency. B) When a gradient field is added to the main field, spatial variation of the precession frequency occurs.

Eqn. [2.15] is a modification of Eqn. [2.7] to include the gradient term. With this change, and assuming for now that there is only signal along the x direction, Eqn. [2.14] becomes:

$$s_r(t) = \int_x m_x(x) e^{-i\gamma G_x x t} dx \quad (5) \quad [2.16]$$

In other words, the received signal is the superposition of magnetization density multiplied by a phase that depends on spatial location. Eqn. [2.16] can be re-written as:

$$s_r(t) = \int_x m_x(x) e^{-i2\pi k_x(t)x} dx \quad \text{where} \quad k_x(t) = \frac{\gamma}{2\pi} G_x t \quad (5) \quad [2.17]$$

The interpretation of Eqn. [2.17] is that the received signal $s_r(t)$ is the Fourier transform of the magnetization m_x . In terms of this Fourier transform interpretation, Eqn. [2.17] can be recast as:

$$s_r(t) = F\{m_x(x)\} = M(k_x(t)) \quad (5) \quad [2.18]$$

Eqn. [2.18] shows that the received signal is the readout over time of the Fourier coefficients (capital M denotes Fourier transform) of the magnetization density and that the frequency variable is k_x . Thus, MRI is an example of Fourier imaging, i.e. a modality where the raw data are collected in the frequency domain. In MRI, the frequency domain is termed “ k -space”, and one must traverse k -space to acquire the data. It is apparent from Eqn. [2.17] that the frequency component collected at any given point in time ($k_x(t)$) depends on the term $G_x t$. Thus, the key idea for acquisitions in MRI is that the operator manipulates gradient fields over time to control the collection of frequency domain data. Eqns. [2.17] and [2.18] can be extended to two dimensions, and the frequency component $\frac{\gamma}{2\pi} G t$, i.e. the phase accrued, can be generalized to an integral for cases where G is not constant. The final signal equation is thus:

$$s_r(t) = \int_x \int_y m_{xy}(x, y) e^{-i2\pi[k_x(t)x + k_y(t)y]} dx dy \quad (5) \quad [2.19]$$

$$\text{where} \quad k_x(t) = \int_0^t \frac{\gamma}{2\pi} G_x(\tau) d\tau \quad \text{and} \quad k_y(t) = \int_0^t \frac{\gamma}{2\pi} G_y(\tau) d\tau. \quad [2.20]$$

Figure 2.4 illustrates the graphical interpretation of the signal equation with a Cartesian k -space readout trajectory. As shown by Figure 2.4a-b, the integral of the

gradients determines the region of k -space covered. In Figure 2.4a, the y -gradient is a “phase encode”; it moves the acquisition to a specific k_y position, after which the x -gradient accomplishes traversal of a horizontal line in k -space. During the traversal of the k -space line, the detection circuitry is activated and data are collected (green line). The phase encode can then be repeated with different gradient amplitudes to cover different lines in k -space. Figure 2.4c shows lines being read out in 2D k -space, but one could easily imagine 3-dimensional lines if the k_z dimension were added. Figures 2.4c and 2.4d also show that as expected the extent to which k -space, i.e. the Fourier domain, is covered determines the coverage and resolution in the object domain. Using standard Fourier relations (5), the object domain resolution is:

$$\text{resolution} = \frac{1}{2k_{\max}} \quad [2.21]$$

Higher resolution can be achieved by going out further in k -space and capturing the higher spatial frequency components. As illustrated in Figure 2.4, to accomplish this, the product $\frac{\gamma}{2\pi} G \cdot t$ has to increase. Object domain field of view (FOV) is given by:

$$\text{FOV} = \frac{1}{\Delta k} \quad [2.22]$$

FOV can be increased by sampling k -space more finely, which is limited in the k_y direction by the number of lines collected and is related to the phase encode step size.

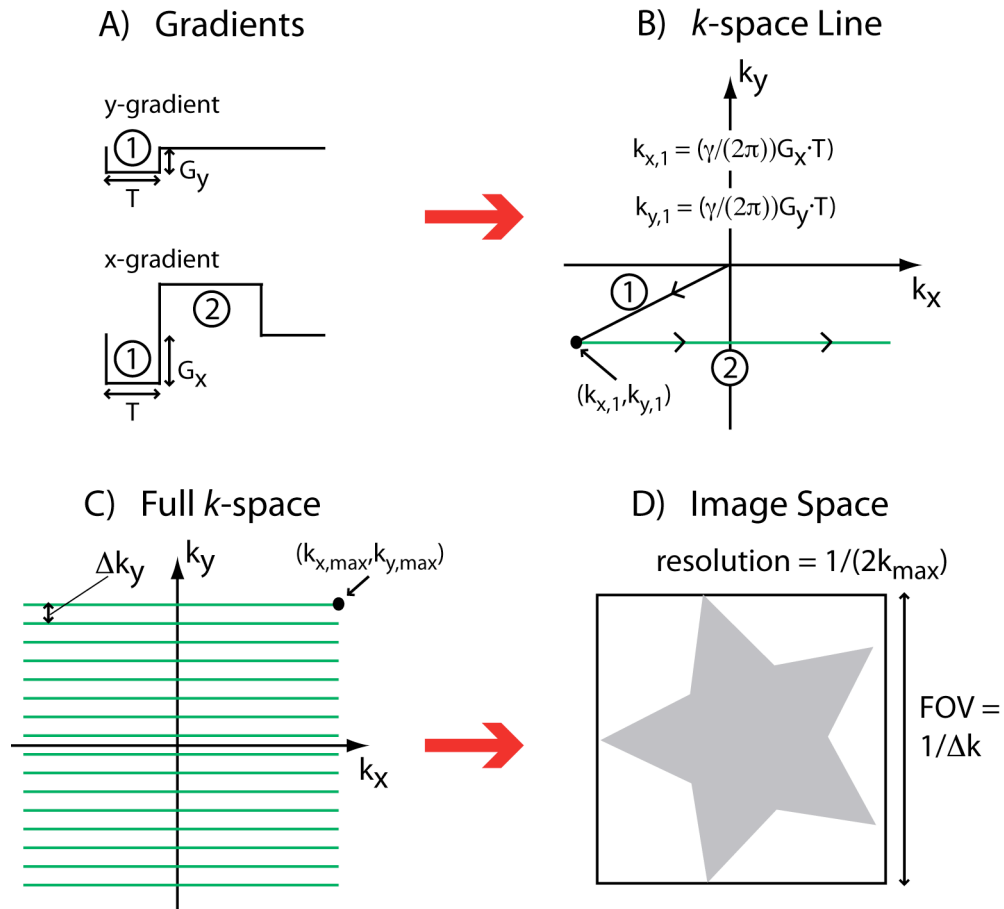


Figure 2.4: Coverage of k -space. A)-B) Time course of gradients and resulting k -space traversal. The running integral of the gradients determines how k -space is traversed. The first portion of the x/y gradients moves the k -space “cursor” to $(k_{x,1}, k_{y,1})$. Then the second portion of the x -gradient traverses a horizontal line in k -space. During that time, the detection circuitry is activated to acquire a line of k -space data. C) The gradients in A) are repeated with the phase encode amplitude G_y stepped incrementally to cover a grid in k -space. D) The k -space data are inverse Fourier transformed to recover the original image. Field of view depends on how finely k -space is sampled, and resolution depends on the extent of k -space coverage.

The k_x dimension (readout direction) does not have these limitations, but FOV_x is generally chosen to match FOV_y . Of course, the FOV chosen should be larger than the size of the object to be imaged, i.e. Δk needs to be sufficiently small (Nyquist criterion); otherwise, aliasing would occur (5). In short, to obtain an image with a specific resolution and FOV, a certain number of samples (requiring time) are needed. An accelerated imaging method to overcome this limitation—compressed sensing—will be discussed in Chapter 3.

2.1.4 RF Excitation

The previous sections assumed \mathbf{m} could be tipped away from the z-axis. Excitation is accomplished by applying a time varying magnetic field (termed the B_1 field) whose carrier frequency equals the Larmor frequency (ω_0) of the species under observation (1,4,5). This B_1 field is implemented as a circularly polarized magnetic field in the transverse plane and acts to make the magnetization vector rotate about it in a manner similar to the precession described by Eqn. [2.6] (1,4,5). Figure 2.5a illustrates the effect of the B_1 field. Note that the rotation of \mathbf{m} and \mathbf{B}_1 at the Larmor frequency is not drawn. In other words, because they both rotate with frequency ω_0 , a rotating reference frame is used, and both are drawn as vectors in this rotating frame. For a B_1 field with constant amplitude, the angle that the magnetization is tipped is given by:

$$\theta = \gamma|B_1|t \quad (4,5) \quad [2.23]$$

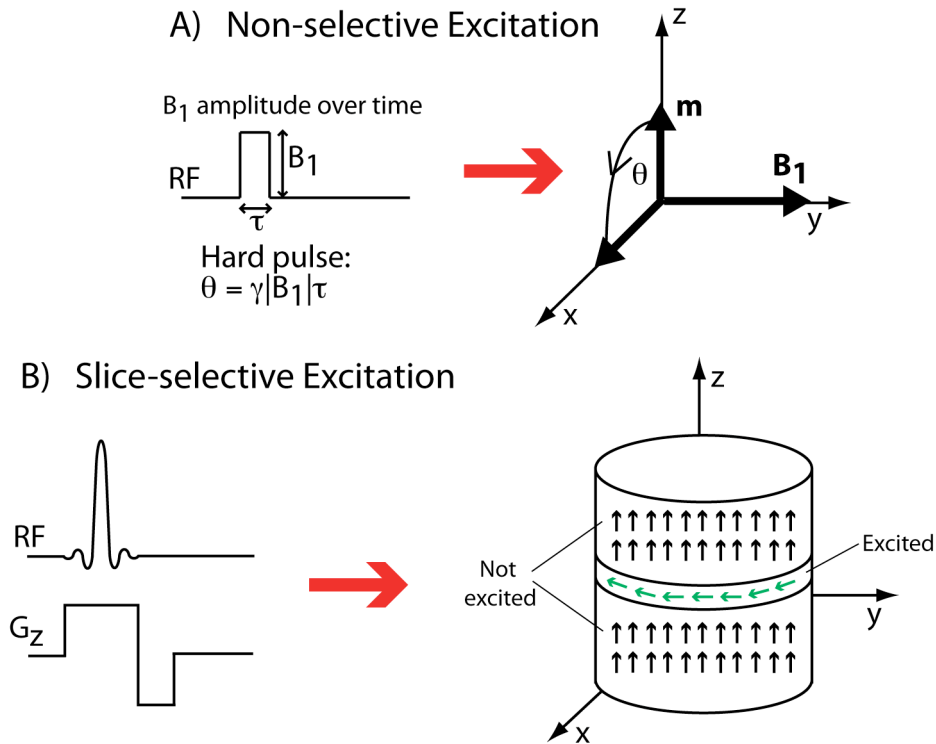


Figure 2.5: A) Non-selective excitation can be achieved with a hard pulse. B) To excite only a slice from a volume, a sinc pulse and a gradient in the slice select direction are needed.

For example, a 90° ($\pi/2$) excitation for carbon could be accomplished with 0.1 gauss (1 Tesla = 10^4 gauss) B_1 amplitude and 2.33 ms duration. From the basic vector geometry shown in Figure 2.5a, the signal strength, i.e. m_{xy} component, is given by the sine of the flip angle (e.g. maximum of $\sin(90^\circ) = 1$), and the remaining m_z component is given by the cosine of the flip angle (e.g. $\cos(90^\circ) = 0$). For hyperpolarized applications, in which m_z magnetization does not recover (Section 2.3.1), the flip angle should be small (much less than 90°) in order to preserve magnetization for all the required phase encodes. In Figure 2.5a, the constant

amplitude “hard” pulse accomplishes non-selective, i.e. whole volume excitation. To achieve selective excitation, i.e. a single slice, the B_1 profile is given a sinc shape and a gradient in the slice select direction is used (Figure 2.5b) (4,5). It turns out that the excitation profile is the Fourier transform of the B_1 profile (4,5), at least for small tip angles ($< 90^\circ$) (a correction for large flip angles is available (6)). The Fourier transform of the sinc function is a rect function, thus allowing for a selection profile with sharp edges. A thorough description of slice selection can be found in many texts (3-5). In addition, there is also a k -space interpretation for excitation (7). In any case, the excitation pulses used in this dissertation are standard designs (6,7), so they will not be described any further.

2.2 Fundamentals of Magnetic Resonance Spectroscopic Imaging

2.2.1 Chemical Shift

MRS/MRSI detects signals from a *spectrum* of molecules in a single acquisition, with each molecule having its own specific resonance frequency, i.e. chemical shift (1). Figure 2.6a illustrates a molecular explanation of this chemical shift. Electrons surrounding a nucleus can be thought to generate small electric currents, which in turn generate local magnetic fields. These magnetic fields add to or subtract from the B_0 field, thus changing the resonant frequency in Eqn. [2.7] to:

$$\omega = \gamma B_0(1 - \sigma) \quad [2.24]$$

The exact contribution of σ to the main field depends on the specific electron environment, i.e. molecular bonding structure. Chemical shift is reported as:

$$\delta_i = \frac{\omega_i - \omega_{TMS}}{\omega_0} \quad (1) \quad [2.25]$$

In other words, the chemical shift of a species is the frequency difference from a known reference, such as tetramethylsilane (TMS), and normalized by field strength so that it is not system dependent. This fraction is usually small and is reported on a parts per million (ppm) scale. Of course, given the ppm of a species, the chemical shift in terms of Hz can be calculated as:

$$\text{shift in Hz} = \frac{\gamma}{2\pi} B_0 \cdot \delta_i \quad [2.26]$$

Figure 2.6b shows a sample carbon-13 spectrum with pyruvate, pyruvate-hydrate, alanine, and lactate with their chemical shifts indicated.

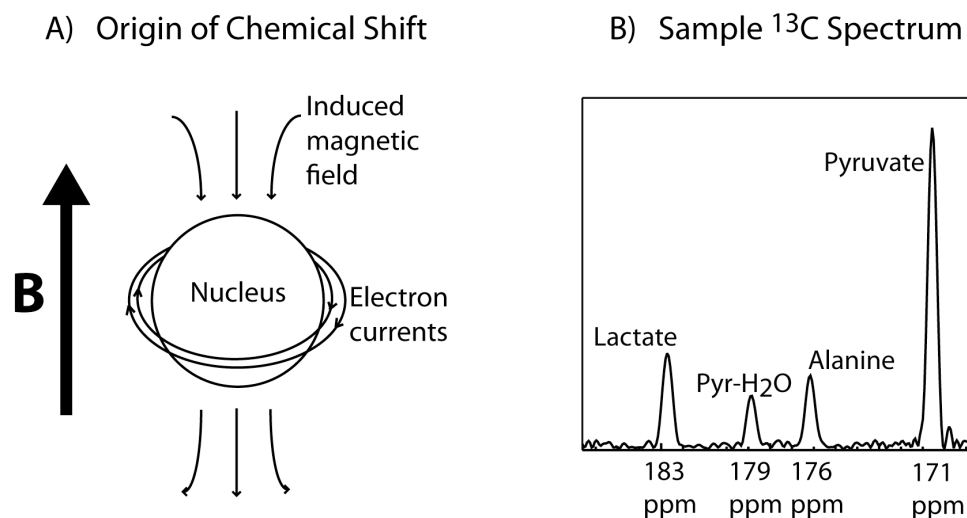


Figure 2.6: A) Chemical shift is an induced magnetic field on top of the main field, resulting in a molecule dependent shift of the Larmor frequency. B) A typical hyperpolarized ¹³C spectrum is shown with the chemical shifts of the different species.

2.2.2 *k*-space Interpretation of Chemical Shift Imaging (CSI)

In a volume excitation of a sample with three chemical shift species—one species at $\omega_0 + \alpha$, another at $\omega_0 + \beta$, and the last at $\omega_0 + \varepsilon$, the detected signal would be (by extension of Eqn. [2.14]):

$$s_r(t) = \int_V (m_{xy1} \cdot e^{-i\alpha t} + m_{xy2} \cdot e^{-i\beta t} + m_{xy3} \cdot e^{-i\varepsilon t}) dV \quad [2.27]$$

The signal would be a superposition of several complex exponentials at different frequencies, and the Fourier transform of $s_r(t)$ would be a spectrum with three peaks. Figure 2.7 graphically illustrates the contributions of the three signal terms to the resulting NMR/MRS spectrum.

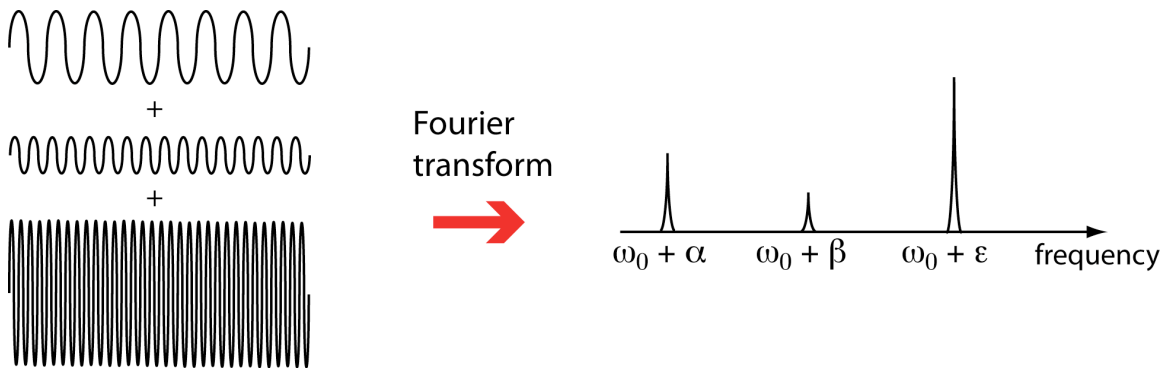


Figure 2.7: In the time domain, a superposition of several complex exponentials (real part shown and ω_0 oscillations not shown) leads to peaks in the frequency domain.

According to standard Fourier relations, the spectral resolution, i.e. the extent to which adjacent frequencies can be distinguished from each other, is determined by the duration of the acquisition:

$$\text{spectral resolution (Hz)} = \frac{1}{T_{\text{readout}}} \quad [2.28]$$

Also according to standard Fourier relations, the spectral FOV is given by:

$$\text{spectral FOV (Hz)} = \frac{1}{\Delta t_{\text{readout}}} \quad [2.29]$$

where Δt is the time between samples during the readout of the signal. In other words, to achieve higher spectral resolution, a longer sampling time is required, and to achieve a larger spectral FOV, a higher sampling rate is needed. Eqns. [2.28] and [2.29] are very similar to Eqns. [2.21] and [2.22]. Thus, the following k -space interpretation can be applied to the spectral, i.e. chemical shift, domain:

$$k_f = t; \quad (5) \quad [2.30]$$

In this interpretation, time is treated as another k -space dimension, so higher spectral resolution is achieved with a longer acquisition time (going further out in k_f), and larger spectral FOV is obtained with a smaller Δt (sampling k_f more finely). Figure 2.8 shows a depiction of k -space with the k_f dimension added. Thus, an MRSI data set can be obtained by acquiring data in a k -space that includes the k_f dimension and taking the inverse Fourier transform.

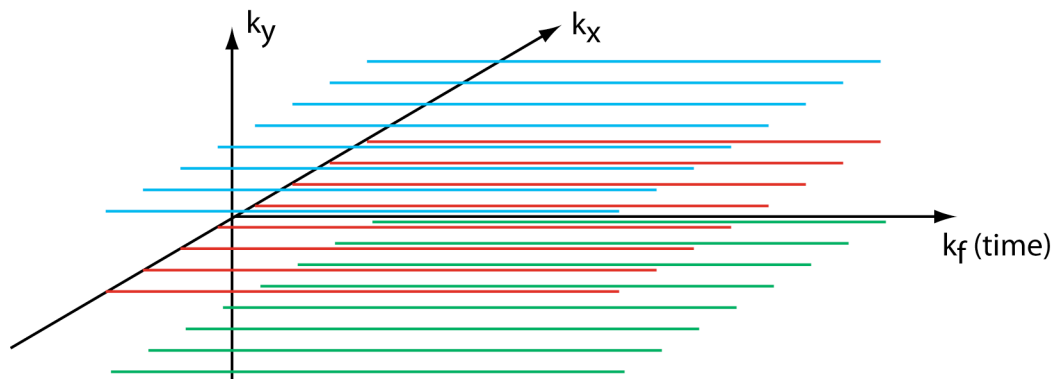


Figure 2.8: Lines being covered in k_x - k_y - k_f space. Three k_x - k_y planes are shown with different colors for easier viewing.

2.3 DNP Hyperpolarization

2.3.1 Past and Recent Work on DNP

As noted in Section 2.1.1, the thermal equilibrium polarization for ^{13}C at 3T and at room/body temperature is only a few parts per million, i.e. about 0.00025%. Through a combination of dynamic nuclear polarization and thermal cooling, the polarization can be increased dramatically. The detailed physics of dynamic nuclear polarization, a technique discovered in the 1950s, are described in a review by Abragam and Goldman (8). Essentially, polarization from electrons (free radicals) can be transferred to nuclei through irradiation with microwaves (at low temperature and in the presence of a strong magnetic field) at a frequency of $\omega = \omega_e \pm \omega_0$, where ω_e is the electron Larmor frequency (in the GHz range) and ω_0 is the nuclear Larmor frequency (8). In the past, DNP was only used for solid state NMR because the polarization could not be retained in liquid state. Recently, a technological breakthrough was made in which a method was developed to rapidly heat and dissolve a DNP polarized sample without losing signal enhancement (9,10). Currently, commercial polarizers can routinely produce enhancements on the order of 100,000-fold, i.e. polarizations of $\sim 25\%$. Parameters such as the precise microwave frequency and concentration of free radical affect the polarization but can be easily optimized empirically. The time it takes to polarize a compound depends on its solid state T_1 , but ~ 1 hour is a typical polarization time for many compounds. In addition, and very importantly, once a compound has been dissolved, its magnetization relaxes from the hyperpolarized value back to the thermal equilibrium value according to the liquid state T_1 . Thus, a major challenge is to

acquire data quickly while the polarization remains. Lastly, it must also be noted that not every compound can be polarized. This dissertation focuses on applications with $[1-^{13}\text{C}]$ pyruvate, the most commonly used substrate so far for *in vivo* hyperpolarized research.

Figure 2.9 shows the base hyperpolarized pulse sequence (11) used for all the studies presented in this dissertation. The sequence is described in more detail in the reference above and in Chapter 3, but in essence, it is used to cover 4D k -space (k_f , k_x , k_y , and k_z).

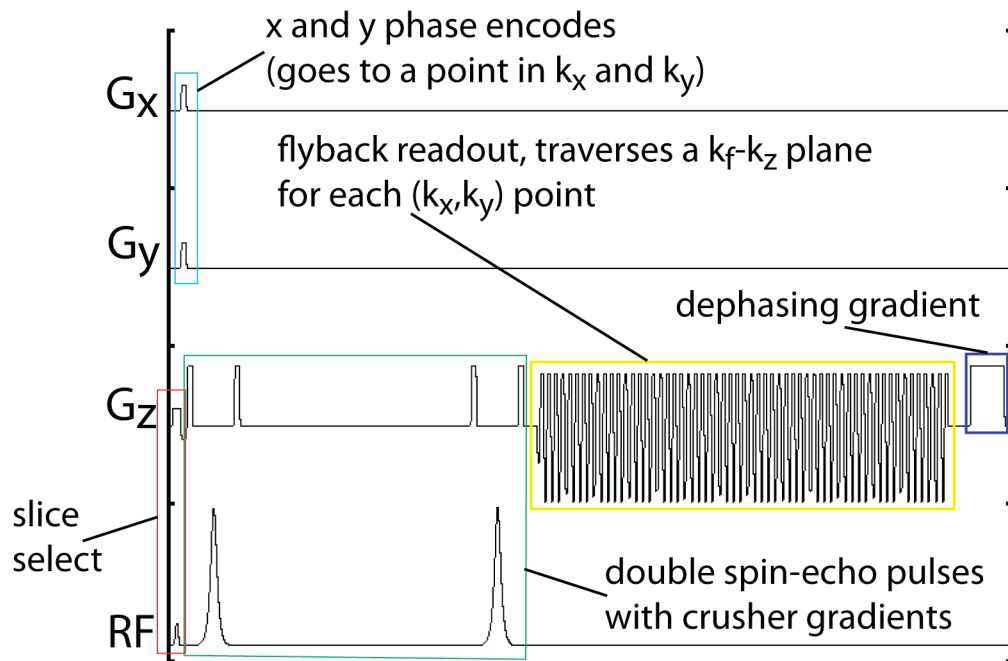


Figure 2.9: Base hyperpolarized pulse sequence. This pulse sequence covers 4D k -space (k_f , k_x , k_y , and k_z). Phase encodes in x and y move the “cursor” to a point in k_x and k_y . Then the flyback gradient traverses a plane in k_f and k_z .

The excitation consists of a small flip angle pulse that excites spins from a large slab. Phase encodes on the x and y gradients cover k_x and k_y , and a flyback waveform (12) reads out k_z and k_f data (k_f data also collected because time progresses during the flyback readout). A dephasing gradient is used at the end of each repetition time (TR), i.e. phase encode cycle, to clear any remaining transverse magnetization that might interfere with the next TR. Lastly, as shown in Figure 2.9, a pair of adiabatic refocusing pulses (with crusher gradients) (11) is used to push the echo time (TE) out in order to collect full echo (both sides of k_f space) data. The adiabatic pulses are robust against a variety of experimental imperfections, and a longer TE does not negatively impact signal strength due to the relatively long T_2 s for pyruvate, alanine, and lactate (13). Adiabatic pulses and full echo data collection are discussed in more detail in Chapter 7.

2.3.2 Metabolic Pathways Probed with DNP Hyperpolarized ^{13}C -pyruvate

Figure 2.10 illustrates the metabolic pathways probed with $[1-^{13}\text{C}]$ pyruvate. As shown in Figure 2.10, after hyperpolarized pyruvate is taken up by cells, it is converted to hyperpolarized lactate and hyperpolarized alanine by lactate dehydrogenase (LDH) and alanine aminotransferase (ALT) respectively. The creation of hyperpolarized lactate has been attributed to a label redistribution phenomenon in which LDH shuttles the ^{13}C label back and forth from pyruvate to a pre-existing pool of lactate (14). Thus, detected hyperpolarized lactate most likely reflects a combination of LDH expression, LDH activity, and endogenous lactate concentration. Hyperpolarized bicarbonate and CO_2 , on the other hand, are

synthesized directly from hyperpolarized pyruvate because the enzyme pyruvate dehydrogenase (PDH) acts only in one direction.

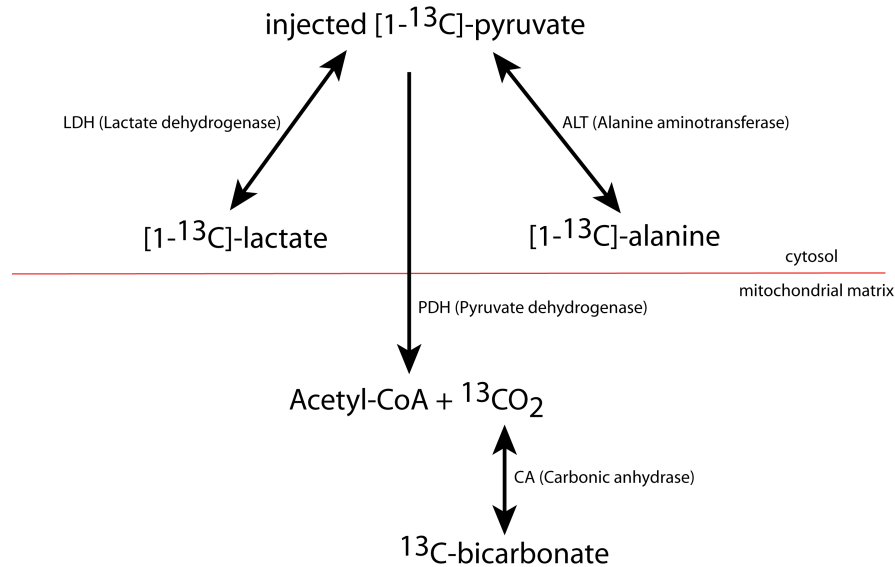


Figure 2.10: Metabolic pathways probed with $[1-^{13}\text{C}]$ pyruvate. Reactions involving LDH, ALT, and PDH are shown.

2.3.2 Clinical Significance

Hyperpolarized ^{13}C technology has great clinical potential to diagnose and monitor pathologies based on detecting abnormal metabolism. A number of research studies have focused on observing hyperpolarized lactate production via LDH following injection of $[1-^{13}\text{C}]$ pyruvate. Preclinical studies have shown an elevated lactate to pyruvate ratio in prostate cancer (15,16), lymphoma (14), and brain cancer (17). Elevated lactate is a powerful biomarker of cancer because tumors go into hyperglycolysis in order to meet their bioenergetic needs (18,19). It should be noted that lactate is one of the metabolic biomarkers being used in clinical

proton MRSI (20,21), but hyperpolarized ^{13}C MRSI would have advantages in terms of SNR and avoiding lipid contamination, and most importantly detects just metabolically-active lactate (from living cells) that was generated from the injected ^{13}C -pyruvate. In general, hyperpolarized technology has many potential advantages over other metabolic imaging modalities, including extremely rapid data acquisition, no ionizing radiation, use of endogenous compounds such as pyruvate, no heavy isotope effects (e.g. deuterium), high signal contrast due to no background ^{13}C signal, and simple data processing resulting from well-separated peaks. Furthermore, a variety of other metabolic processes relating to disease can be probed with agents other than $[1-^{13}\text{C}]$ pyruvate. These agents will be touched upon in the following chapters, but they are not the focus of this dissertation. In summary, hyperpolarized ^{13}C technology is an extremely powerful and potentially very clinically significant metabolic imaging modality, which explains the recent flurry of technical and preclinical research on the topic.

Chapter 3: An Initial Compressed Sensing Design for Hyperpolarized ^{13}C MRSI

The following chapter is adapted from: Hu et al. Compressed Sensing for Resolution Enhancement of Hyperpolarized ^{13}C Flyback 3D-MRSI. J Magn Reson 2008;192:258-264.

3.1 Background and Theory

3.1.1 Motivation

In vivo applications of carbon-13 magnetic resonance spectroscopy have traditionally been limited by low signal strength. With the development of techniques to maintain hyperpolarization of carbon-13 in liquid state (9), it has become possible to use ^{13}C substrates (tracers) for medical imaging (22). More recent studies have used the metabolically active substrate $[\text{l-}^{13}\text{C}]\text{pyruvate}$ to examine its conversion to $[\text{l-}^{13}\text{C}]\text{lactate}$, $[\text{l-}^{13}\text{C}]\text{alanine}$, and $^{13}\text{C}\text{-bicarbonate}$ (15,16,23,24). Spectroscopic examination of these metabolic pathways in the presence and absence of disease has enormous diagnostic potential. Specifically, it has already been shown that the levels of ^{13}C metabolic products differ between disease and non-disease states in a mouse model of prostate cancer (15,16). As pointed out in (15), partial volume effects may complicate the interpretation of non-disease spectra because of the small size of the normal mouse prostate. With the abundant SNR available in hyperpolarized studies, it would be beneficial to sacrifice

some signal for improved spatial resolution, but the time limitation imposed by T_1 relaxation severely restricts the possible number of phase encode steps.

Recent advances in mathematical theory have opened the door for accurate reconstruction of sparse signals from sub-nyquist sampling (25,26). Less technical descriptions from the same authors, focusing on the practical limits of compressed sensing, have shown reconstructions from realistic data sets (27,28). In addition, Lustig et al., in an exposition of the application of compressed sensing to MRI, shows that many MR images exhibit a high degree of sparsity and provides high quality proof of concept results drawn from multi-slice fast spin-echo brain imaging and 3DFT time of flight contrast enhanced angiography (29). Lustig lists three criteria for the successful application of compressed sensing: 1) the data have a sparse representation in a transform domain 2) the aliasing from undersampling be incoherent in that transform domain and 3) a non-linear reconstruction be used to enforce both sparsity of data and consistency with measurements. The successes in (29), coupled with the sparsity in hyperpolarized spectra, make hyperpolarized ^{13}C spectroscopic imaging a logical choice for the application of compressed sensing. In other words, for hyperpolarized ^{13}C , the first criterion is satisfied by the inherent sparseness of hyperpolarized spectra, and the third criterion can be met by using the same non-linear reconstruction from (29). The primary challenge then is to satisfy the second criterion: developing an undersampling approach to achieve suitable incoherent aliasing.

The sparsity of hyperpolarized spectra has been previously exploited for accelerated imaging (30,31) by using *a priori* knowledge of metabolite resonance

locations and linewidths (factor of 4 acceleration reported in a phantom demonstration (30)). Compressed sensing, however, requires no assumptions except that the underlying data are sparse in some domain.

A 3D-MRSI sequence using flyback echo-planar readout gradients (11,12) provides a fast method for acquiring hyperpolarized spectra and is less sensitive to timing errors, eddy currents and B_0 inhomogeneity than EPI and spiral readout schemes, especially *in vivo*. This chapter presents a methodology for accelerating the acquisition of hyperpolarized spectra by a factor of 2 using compressed sensing in conjunction with a modified flyback echo-planar 3D-MRSI sequence. A few initial phantom and *in vivo* examples are presented as proof of concept.

3.1.2 Existing Pulse Sequence

The pulse sequence developed for this study builds on the one diagrammed in Figure 3.1, which is a double spin-echo sequence with a flyback echo-planar readout (11). Details of the flyback design are given in (12). As explained in (11), a spin-echo sequence was desired in order to mitigate the effects of B_0 inhomogeneity and allow for a full echo acquisition. Owing to its insensitivity to transmit gain, this double adiabatic sequence outperforms a conventional spin-echo sequence in preserving hyperpolarization over the repeated excitations needed for the phase encodes in an MRSI acquisition (11). Ultimately, this sequence reads out a rectilinear k-space trajectory, with a typical result being $59 \times 8 \times 8 \times 16$ (k_f - k_x - k_y - k_z) 4D k-space data.

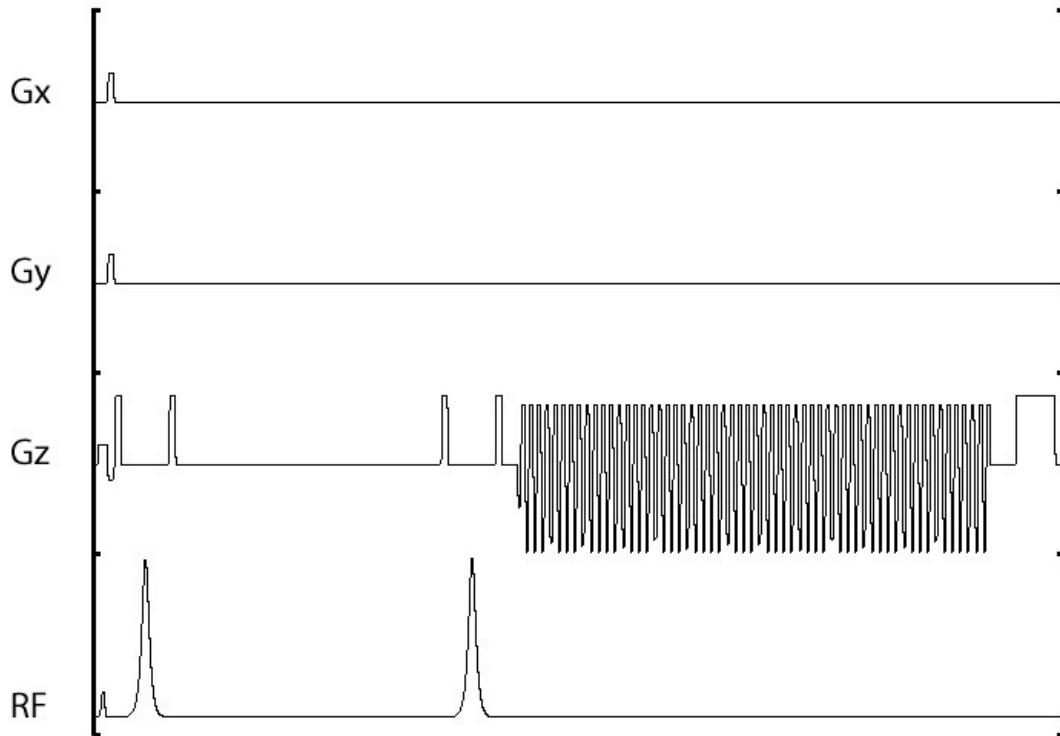


Figure 3.1: Double spin-echo sequence timing diagram. The RF consists of a small tip excitation followed by two adiabatic pulses (phase channel not shown). Phase encoding is along x and y while the 59-lobe flyback readout is along z . An echo is formed during the middle of the flyback readout with $TE = 140ms$.

3.1.3 Key Results from Compressed Sensing Literature

Fundamentally, compressed sensing claims to perfectly reconstruct sparse signals of length N from a subset of samples. For example, suppose a length N discrete signal f consists of M non-zero points. Then, with extremely high probability, f can be recovered exactly from K Fourier measurements where

$$K \geq \text{Const} \cdot M \log N \quad [3.1]$$

and the solution is found by solving the convex minimization problem

$$\min \sum_n |g[n]| \quad s.t. \quad F_K\{g[n]\} = y \quad [3.2]$$

where F_k is the Fourier transform evaluated at K locations and y is the set of K measured Fourier coefficients (27). In words, Eqn. [3.2] states that for all reconstructions $g[n]$ whose Fourier coefficients match those at the K measured positions, the unique and correct solution is the one that minimizes the absolute sum of g , i.e. the ℓ_1 norm in the object domain. The theorems of compressed sensing are actually much more general than this concrete example suggests. In other words, the signal f only needs to be sparse in some domain, not necessarily the object domain, and the K measurements do not necessarily have to be Fourier measurements. From a practical standpoint, the application specific values for M , N , and the constant multiplier determine the feasibility of compressed sensing. Additionally, a real-world signal will never consist of just M non-zero points in any domain, but it *will* usually be well approximated by M sparse transform coefficients. For example, the fidelity with which compressed sensing reproduces an M -term wavelet approximation, i.e. the sparse domain being the wavelet domain, could serve as a benchmark for real-world signals such as NMR spectra (28). For various $N = 1024$ test signals in (27), Candes empirically determined that for compressed sensing to match the accuracy of an M -term wavelet representation, $K \approx 3M-5M$ measurements were required, which was also observed in (29). As mentioned previously, for the actual implementation of compressed sensing, the K measurements must be collected with a sampling pattern that produces incoherent

aliasing in the domain, such as the wavelet domain, where the signal shows sparsity (29). A random sampling pattern in k-space almost always meets this criterion.

At this point, it is interesting to consider the connection between compressed sensing and existing techniques in NMR, such as maximum entropy (32,33) and minimum area (34) reconstruction, used for the related problem of computation of spectra from short, noisy data records. Recently, Stern et al. showed that a specific form of iterative thresholding, a technique similar to maximum entropy and minimum area reconstruction, is equivalent to the minimum ℓ_1 norm reconstruction in compressed sensing (35). Additionally, Stern explains how ℓ_1 norm reconstruction gives insight into the performance of maximum entropy and minimum area reconstruction. Thus, compressed sensing could be viewed as a generalization of existing NMR techniques.

3.1.4 3D-MRSI Signal

The most straightforward application of compressed sensing to hyperpolarized 3D-MRSI would be to undersample in k_x and k_y . For example, to achieve 16×8 spatial resolution in the time of 8×8 phase encodes, i.e. a speedup factor of 2, one could simply collect 8×8 of the phase encodes in a conventional 16×8 scan ($K = 64$, $N = 128$). However, our wavelet simulations have shown that such a small N leads to a relatively large M and thus does not provide enough sparsity to exploit. A better strategy would be to attempt undersampling in the k_f and k_x dimensions, considering that typical hyperpolarized acquisitions are inherently sparse in the spectral dimension. As shown in the wavelet simulations of Figure 3.2,

a signal of this type (spectral dimension and one spatial dimension) exhibits considerable sparsity.

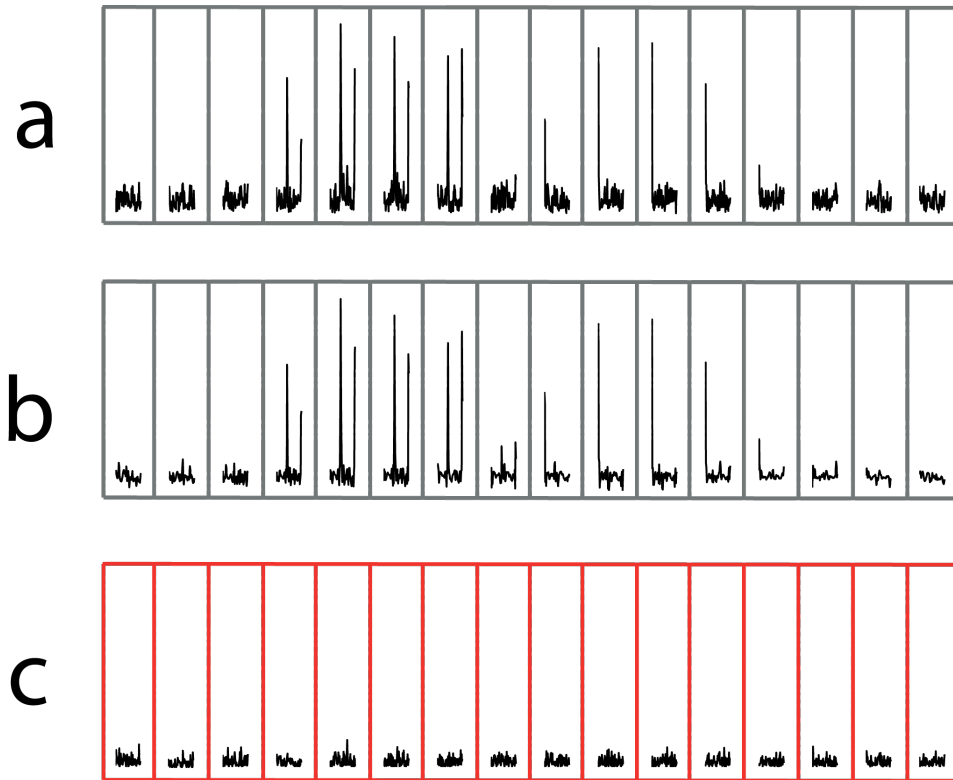


Figure 3.2: Demonstration of wavelet compressibility of a ^{13}C spectroscopic signal. A row of magnitude spectra (64×16) from a 3D-MRSI phantom data set (see Figure 3.5 for examples of rows of spectra) was taken as the test signal. Note that the 59 spectral points from the 59 flyback lobes were zero-padded to 64 because the wavelet software we used required dyadic numbers. a) The 16 original spectra. b) A 2D Daubechies wavelet transform was applied to the 64×16 data, after which the top 10% wavelet coefficients were retained and the inverse 2D wavelet transform taken. c) The magnitude error between a) and b). Note that a), b), and c) have the same y-axis scale. The 64×16 data were reconstructed very accurately from only 10% of their wavelet

coefficients, showing that the signal of interest exhibits considerable fundamental sparsity.

(Note that wavelet transforms were chosen because they do a good job of sparsifying NMR spectra (28), though other choices are possible as well.) The key point is that the majority of the sparsity occurs in the spectra and therefore the time domain should be undersampled. However, the implementation of time domain undersampling is not at all straightforward, as the next section demonstrates. A scheme to undersample in the time domain as well as in one spatial domain was employed, mainly exploiting spectral sparsity but some spatial sparsity as well.

3.2 Methods

3.2.1 Pulse Sequence Development for 2-fold Acceleration

The key to implementing a k-space trajectory that randomly undersamples in k_f - k_x lies in the random sampling of $k_f = t$ using blips. Figures 3.3 and 3.4 illustrate a scheme that achieves k_f sub-sampling by hopping back and forth between adjacent k_x lines during a flyback readout. In this manner, data from two k_f - k_x lines are acquired during a single phase encode, in effect randomly undersampling in time. Thus, 16×8 resolution can be achieved in half the time by collecting 8×8 of the readouts in a conventional 16×8 scan. This approach is somewhat similar to the k - t sparse scheme in (36,37), but here we apply gradients to move around in k_f space instead of reordering phase encodes.

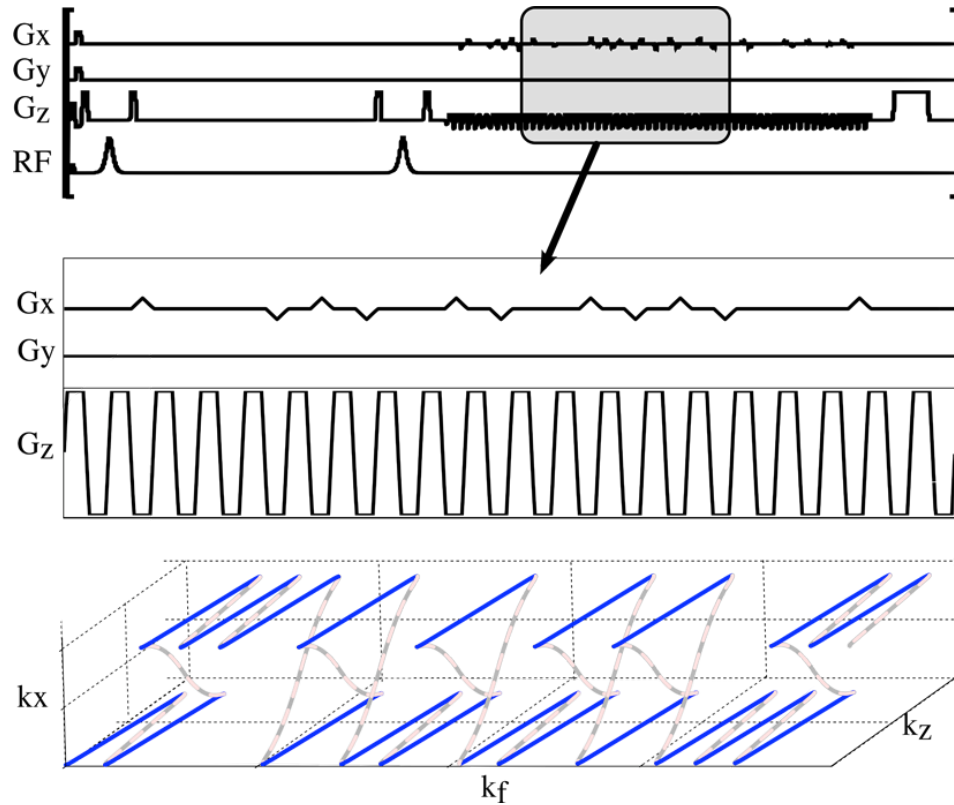


Figure 3.3: Blipped scheme for k_f - k_x sub-sampling. Top: The only modification to the pulse sequence shown in Figure 3.1 is the addition of blips during the rewind portions of the flyback readout. The area of each blip is the area in an x -phase encode step. Bottom: Associated order of k -space readout. A single readout now covers two k_f - k_x lines.

This blipped scheme addresses the design challenge of generating sufficient incoherent aliasing through random undersampling, in other words meeting the second criterion for the successful application of compressed sensing. Without the blips, there would be too much structure to the undersampling, which would lead to coherent aliasing. To reiterate, the design in Figure 3.3 achieves two-fold undersampling by jumping between two lines.

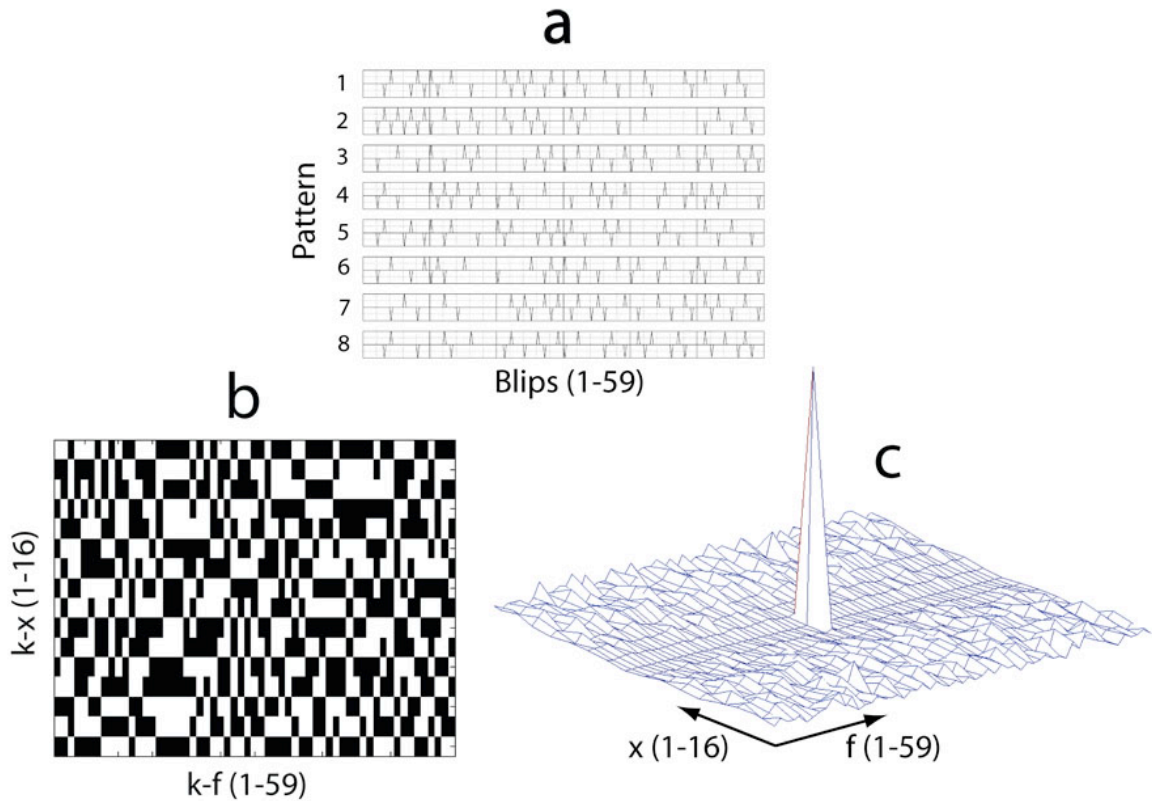


Figure 3.4: Blipped patterns to cover 16 k_f - k_x lines, resulting coverage, and point spread function. a) Actual 8 blipped patterns used to cover 16 k_f - k_x lines in a pseudo-random manner. b) Associated k -space sampling. Because twice as much k -space is covered in the time of 8 phase encodes, half of the 59×16 k_f - k_x points are missing (missing points are black). c) 2D point spread function of pseudo-random pattern in b).

A design to achieve three-fold undersampling would have to jump between 3 lines, and a design to achieve four-fold undersampling would have to jump between 4 lines. Finally, we used the Duyn method (38,39) to measure the actual k -space trajectory traced out by our blips. As expected, on a modern clinical scanner with eddy current compensation, the measured k -space trajectory closely matched the

intended one. In other words, the blips produced minimal side effects, and unintended k-space deviations were negligible.

3.2.2 Pulse Sequence and Hardware

The source code from (11), originally a free induction decay (FID) MRSI sequence, was modified to incorporate triangular gradient blips. In an attempt to minimize eddy current effects, the blips were made 0.8 ms, relatively wide considering the time between adjacent flat flyback portions was 1.16 ms. The amplitude of the blips was calculated by the source code so that each blip's area equaled the area in a phase encode increment. As in (15), a variable flip angle (VFA) scheme (40), i.e. increasing flip angle over time to compensate for the loss in hyperpolarized signal, was used in the *in vivo* experiments. The actual n^{th} flip angle $\theta[n]$ precalculated in the source code for a given acquisition of N flips was as follows:

$$\theta[n] = \begin{cases} 90^\circ & \text{if } n = N \\ \arctan(\sin(\theta[n+1])) & \text{if } n < N \end{cases} \quad [3.3]$$

For example, in our acquisition with $N = 8 \times 8 = 64$ readouts, $\theta[64] = 90^\circ$, $\theta[63] = \arctan(\sin(90^\circ)) = 45^\circ$, $\theta[62] = \arctan(\sin(45^\circ)) = 35.3^\circ$, ... $\theta[1] = 7.2^\circ$. Calibration of the pulse angles was performed on the day of each study using a prescan of a corn oil phantom. In addition, for the *in vivo* experiments, as in (15), reordering of phase encodes to collect data near the k-space origin first was also employed. For all experiments, T_2 -weighted images were acquired with a fast spin-echo sequence, after which MRSI data, phase encode localized in x/y with flyback readout in the S/I

direction z , were collected. All experiments were performed on a General Electric EXCITE 3T (Waukesha, WI) clinical scanner equipped with 40 mT/m, 150 mT/m/ms gradients and a broadband RF amplifier. Custom built, dual-tuned $^1\text{H}/^{13}\text{C}$ transmit/receive coils were used for all phantom and animal experiments.

3.2.3 Reconstruction

For acquisitions without blipped gradients, the reconstruction procedure, carried out with custom MRSI software (41), was as follows: 1) sample the raw flyback data to obtain a 4D matrix of k -space data 2) apodize each FID and apply a linear phase correction to the spectral samples as described in (12) to account for the tilted k -space trajectory characteristic of a flyback readout and 3) perform a 4D Fourier transform with zero-padding of the spectra. For blipped acquisitions, the processing pipeline was modified in that the flyback sampling was performed in MATLAB (Mathworks Inc., Natick, MA) and the k -space points missed by the blipped trajectory were iteratively filled in using a non-linear conjugate gradient implementation of Eqn. [3.2] (29). Specifically, the reconstruction procedure for blipped acquisitions was as follows: 1) order the raw blipped flyback data to obtain a 4D matrix of k -space data missing half of its k_f - k_x points 2) inverse Fourier transform the fully sampled k_y and k_z dimensions 3) iteratively fill in the missing k_f - k_x points in the 4D matrix using the algorithm from (29) 4) forward Fourier transform the k_y and k_z dimensions to put the data back into the form of a filled k_f - k_x - k_y - k_z set 5) apodize each FID and apply a linear phase correction and 6) perform a 4D Fourier transform with zero-padding of the spectra. Transforming in the fully

sampled k_y and k_z dimensions allowed us to separate the multi-dimensional reconstruction problem into many separable 2D reconstructions, reducing the memory requirements and allowing parallel processing as was done for the 3D angiography example in (29). The total reconstruction time for the normal and compressed sensing reconstructions were ~ 5 seconds and ~ 20 minutes respectively on a 1 GHz, 2 GB RAM Sun workstation running Red Hat Linux. The compressed sensing reconstruction was implemented in MATLAB. We expect significant speed improvement with code optimization.

3.2.4 Phantom Methodology

Experiments on a cylindrical phantom (Figure 3.5a) ($n = 3$, with repositioning for separate trials) containing ^{13}C -labeled pyruvate/pyruvate- H_2O , lactate, and alanine in three respective inner spheres, were performed to verify the accuracy of the compressed sensing reconstruction. For both unblipped and blipped acquisitions, a flip angle of 10 degrees, TE = 140 ms, TR = 2 seconds, FOV = 8cm \times 8cm, and 16 \times 8 resolution were used. The 16 \times 8 unblipped acquisition with the standard reconstruction served as the gold standard. For the 16 \times 8 blipped acquisition, acquired in half the time, the modified processing pipeline as discussed in the previous section was used. The sparsifying transform was a 1D length-4 Daubechies wavelet transform in the spectral dimension, meaning the algorithm presumed sparsity of the spectral peaks and tried to minimize the ℓ_1 norm of a wavelet transform of the k_f data. In addition, as is commonly done (29), a total variation (TV) penalty was added to promote sparsity of finite differences. The

weights given to the wavelet transform and TV penalty, and thus the amount of denoising and data fidelity, were selected manually by testing a few values on one phantom acquisition. The same weights were used for subsequent phantom and animal experiments. Specifically, using the software described in (29), which normalizes the maximum signal in the object domain to 1, the TV penalty and transform weights were both 0.01.

3.2.5 *In Vivo* Methodology

We performed normal and compressed sensing comparisons for three separate mice. For the in vivo experiment whose results are shown in Figure 3.6, a prototype DNP polarizer developed and constructed by GE Healthcare (Malmö, Sweden) was used to achieve ~23% liquid state polarization of [^{13}C]pyruvate. Due to unavailability of the prototype machine for the second and third in vivo comparisons, a HypersenseTM DNP polarizer (Oxford Instruments, Abingdon, UK), which is a commercial version of the prototype machine, was used to achieve polarizations of ~11% and ~18% respectively. The polarization was measured by extracting a small aliquot of the dissolved solution and measuring its FID intensity with a custom low-field spectrometer. ~300 μL (~80 mM) samples were injected into a surgically placed jugular vein catheter of a Transgenic Adenocarcinoma of Mouse Prostate (TRAMP) mouse (42,43) within ~20s of dissolution. The particular TRAMP mouse for the first trial had a large prostate tumor with many relatively homogenous tumor voxels across the FOV, making quantitative comparisons easier. The other two mice had smaller, yet still relatively homogeneous, tumors. For each

trial, two runs were done (~2 hours apart), once for an unblipped $59 \times 8 \times 8 \times 16$ standard acquisition and again for a blipped $59 \times 16 \times 8 \times 16$ compressed sensing acquisition. The acquisition parameters for both runs were TE = 140 ms, TR = 215 ms (total acquisition time of 14 seconds), variable flip angle activated, reordered phase encodes, and FOV = 4cm \times 4cm. The blipped acquisition, using 8×8 of the readouts from a conventional 16×8 scan, was acquired after the unblipped one. All animal studies were carried out under a protocol approved by the Institutional Animal Care and Use Committee. A more detailed description of the polarization and animal care procedures can be found in (15,24).

3.3 Results and Discussion

3.3.1 Phantom Results

Figure 3.5 shows a side-by-side comparison of a slice of final processed spectra from representative 16×8 unblipped and blipped acquisitions (corresponding to Trial 1 in Table 3.1), with the blipped acquisition taken immediately after the unblipped one. Qualitatively, the spectra match up extremely well. Table 3.1 gives a quantitative comparison of the two reconstructions for the three trials, listing SNR and metabolite peak ratios. The accelerated acquisition ratios were always within 10% of those from the fully sampled acquisitions, which was about the same as the accuracy reported in (30). Because we typically draw biological conclusions from final processed spectra, SNR was calculated with the magnitude spectra after apodization and zero-padding. Typically, halving the scan

time, as was done for the blipped acquisition, would reduce SNR by a factor of square root of 2.

Table 3.1: Comparison of SNR and metabolite peak ratios for normal vs. compressed sensing phantom data.

		Peak SNR	Ala/Lac Ratio	Pyr/Lac Ratio	Pyr-H₂O/lac Ratio
Trial 1	Normal 16x8	63.2	.55	.46	.43
	Compressed Sensing 16x8	64.8	.55	.47	.41
Trial 2	Normal 16x8	59.7	.94	.50	.47
	Compressed Sensing 16x8	68.7	.89	.46	.42
Trial 3	Normal 16x8	52.5	.66	.40	.40
	Compressed Sensing 16x8	62.4	.60	.37	.36

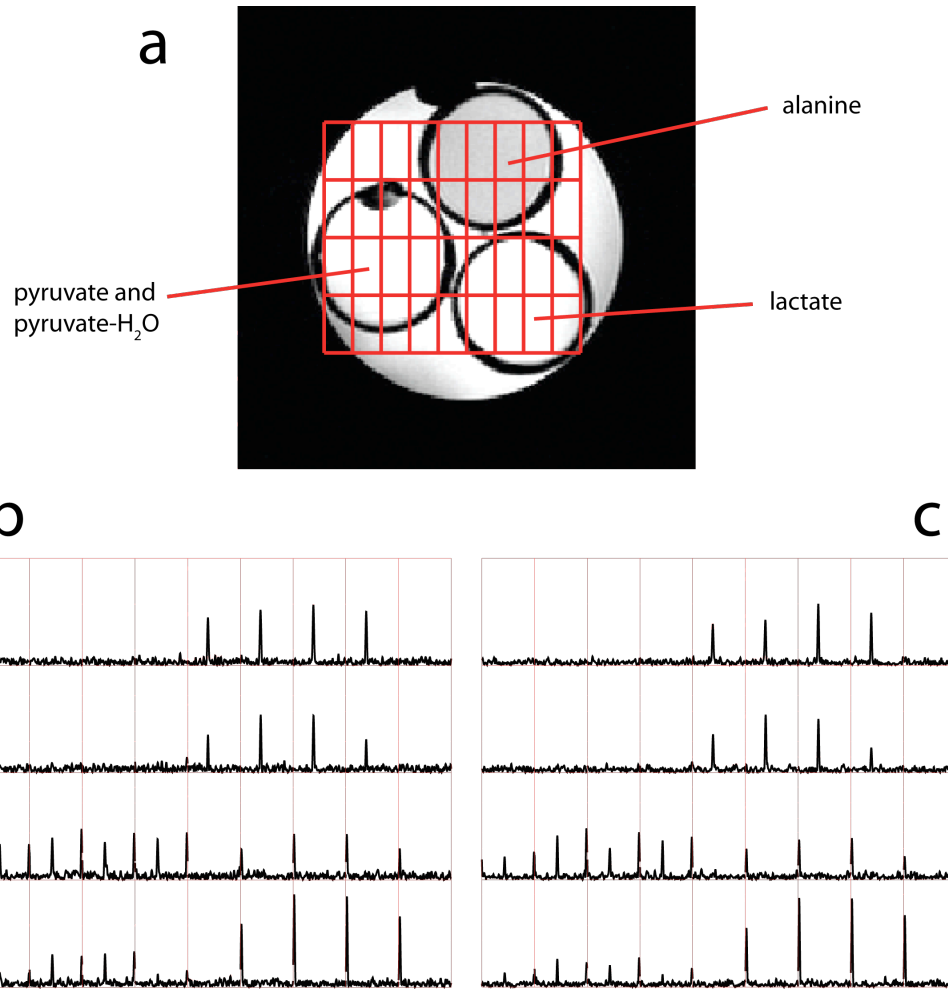


Figure 3.5: 16x8 phantom comparison of normal vs. undersampled. a) T_2 -weighted image of ^{13}C phantom done before spectral acquisitions. b) Spectra from normal, unblipped acquisition corresponding to the highlighted voxels from a). c) Spectra from compressed sensing reconstructed, blipped acquisition corresponding to the highlighted voxels from a).

Due to the denoising properties of the compressed sensing reconstruction combined with apodization, the SNR did not drop. The ℓ_1 penalty used in compressed sensing is essentially a denoising procedure, also referred to in the literature as basis-pursuit

denoising (44) and is closely related to wavelet denoising schemes (45-47). The ℓ_1 reconstruction transforms the signal into a domain in which the signal exists in only a few significant coefficients, whereas noise resides in the majority of coefficients, and filters the noise by heavily penalizing the small coefficients. In addition, in compressed sensing, the undersampling itself generates incoherent aliasing which appears as noise (29), which is penalized and filtered. Thus, the process of the ℓ_1 reconstruction picking a solution to the compressed sensing problem, in other words the underdetermined problem caused by undersampling, has the natural side effect of denoising. Therefore, the compressed sensing SNR is controllable in the sense that merely adjusting the ℓ_1 denoising parameters in the reconstruction would lead to higher SNR. However, too much denoising could lead to metabolite peak height distortion manifested by underestimating the true peak height. In this study, we tested denoising parameters within an order of magnitude as those in (29) and selected ones that performed well. As for the peak ratio calculations, the metabolite peak heights used were average peak heights over voxels with little or no partial voluming. The metabolite ratios for normal and compressed sensing data sets were similar, suggesting compressed sensing could be compatible with metabolite quantitation.

3.3.2 *In Vivo* Results

Figure 3.6 shows a comparison of 8×8 mouse tumor data from a conventional scan and data from the same mouse acquired ~2 hours later with a 16×8 compressed sensing acquisition.

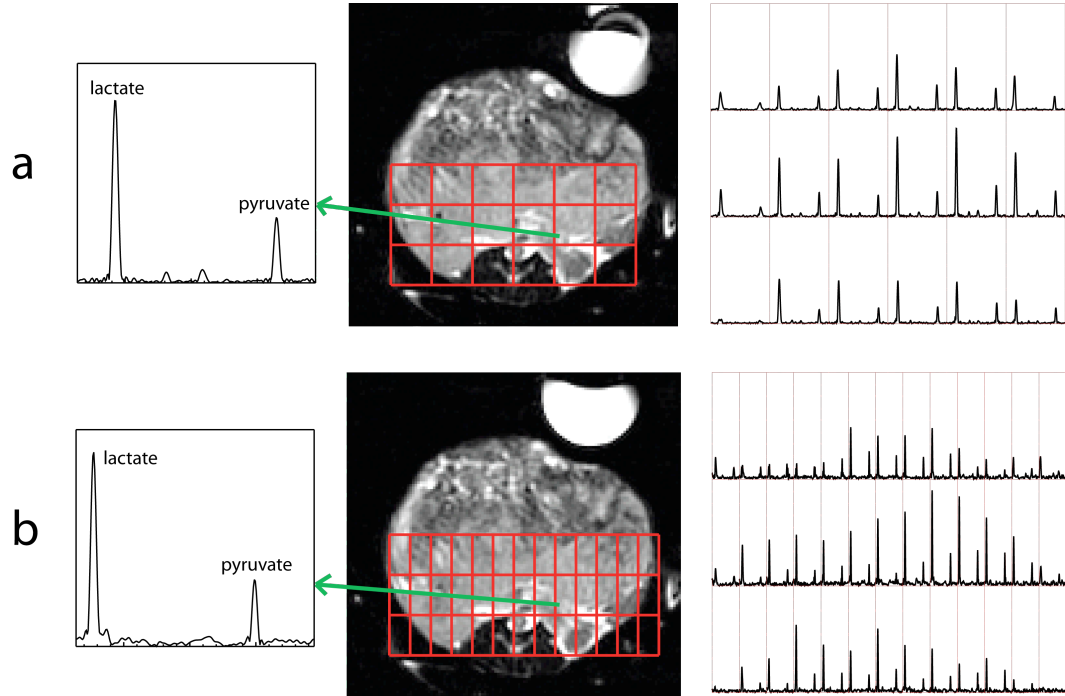


Figure 3.6: Comparison of 8x8 normal mouse data and 16x8 undersampled mouse data in a region of prostate tumor. a) Normal 8x8 data. The left shows the spectrum with the highest lactate peak, the middle shows the T_2 -weighted anatomical image, and the right shows spectra highlighted in the anatomical image. b) Corresponding 16x8 data acquired two hours after the 8x8 data.

Qualitatively, the two sets of data appear similar, both showing elevated lactate characteristic of cancer tissue in the TRAMP model. One difference is that due to lower starting SNR, residual coherent aliasing, and the sparsifying effect of the ℓ_1 reconstruction, the 16x8 mouse data do not show tiny peaks such as the alanine and pyruvate- H_2O bumps seen in the single spectrum of Figure 3.6a. The reason is that high contrast spectral peaks result in large distinct sparse coefficients which can be

recovered even when vastly undersampled, whereas very small peaks close to the noise floor could be submerged by both apparent noise caused by aliasing (29) and the true underlying noise that they would not be recoverable. As discussed in the artifacts section of (29), with increased undersampling the most distinct artifacts in compressed sensing are not the usual loss of resolution or increase in aliasing, but the loss of very small peaks. For the specific data shown in Figure 3.6, the SNR of the alanine and pyruvate-H₂O bumps in the 8×8 acquisition were 17.7 and 14.3. By going to half the voxel size with 16×8 resolution, the true SNR in each voxel would be halved, in other words reduced to about 8. In addition, the extra apparent noise caused by undersampling and reconstruction inaccuracies (29) would further hurt the ℓ_1 reconstruction. According to the literature, coefficients can be recovered up to a multiple of the noise variance (48,49), and Lustig et al. describes this phenomenon for MRI in more detail while providing some examples (29). For our spectra, we noticed that we needed an SNR of about 6 to 7 to distinguish a spectral peak from random spikes in the noise floor. Therefore, we believe the disappearance of the small peaks can be attributed to their being too close to the noise floor. In this scenario, no amount of denoising will recover the peaks, which is an important limitation of compressed sensing. Compressed sensing works best for applications with high SNR that are acquisition time limited such as measuring the lactate/pyruvate ratio in tumors. The second and third *in vivo* trials showed similar results except for a lower lactate/pyruvate ratio due presumably to the less advanced disease stage of those tumors. Table 3.2 gives a quantitative comparison of the two reconstructions for each trial, showing SNR and lactate/pyruvate peak

ratios. Halving the voxel size would normally reduce SNR by a factor of 2, but due to ℓ_1 denoising and apodization, as discussed in the previous section, the final SNR for the 16x8 data was only 14-20% lower than that of the 8x8. Finally, as shown in Table 3.2, the ratios and standard deviations of the ratios match up reasonably well.

Table 2: Comparison of SNR and metabolite peak ratios for normal vs. CS mouse data.

		Peak SNR	Lac/Pyr Ratio	Standard Deviation of Lac/Pyr Ratio
Trial 1	Normal 8x8	133.9	2.44	.432 (n = 16 voxels)
	Compressed Sensing 16x8	107.4	2.51	.558 (n = 14 voxels)
Trial 2	Normal 8x8	41.1	1.54	.315 (n = 4 voxels)
	Compressed Sensing 16x8	34.3	1.29	.353 (n = 8 voxels)
Trial 3	Normal 8x8	75.3	1.36	.246 (n = 4 voxels)
	Compressed Sensing 16x8	64.8	1.38	.522 (n = 8 voxels)

3.3.3 Limitations and Future Work

The parameters controlling the level of denoising, and thus the final SNR, in this work were chosen manually. The parameters were chosen to strike a balance between denoising and the data fidelity constraint of Eqn. [3.2]. In the future, an automatic parameter choice scheme would be desirable. In addition, by employing more of the techniques in (29), such as phase estimation and variable density sampling patterns, it should be possible to perform more denoising and recover a higher SNR percentage without sacrificing data fidelity. Since the distribution of energy in k-space is localized close to the k-space origin, variable density sampling corresponding to that distribution has a better initial signal to aliasing interference ratio than uniform undersampling. It was reported in (29) that variable density schemes result in faster convergence and significantly better overall reconstruction quality and we expect our case to perform in the same way. In addition, investigation into different wavelet sparsifying transforms could yield further performance enhancements. Building on the blipped methodology presented in this paper to develop a sampling pattern in which k_f , k_x , and k_y are undersampled could also provide a substantial performance gain by exploiting 3D sparsity and spreading aliasing into three dimensions, thus producing more incoherent aliasing. Lastly, combining parallel imaging and compressed sensing could be a viable avenue of investigation. With the abovementioned developments, much higher rates of acceleration might be obtainable in future hyperpolarized C-13 metabolic imaging studies.

3.3.4 Conclusion

An initial design and results for hyperpolarized ^{13}C compressed sensing were presented in this chapter. Key to the design was the exploitation of sparsity in hyperpolarized spectra and an implementation that used blips to undersample in k_f and k_x . Phantom experiments showed low SNR loss while preserving accuracy of metabolite peak ratios, and mouse trials demonstrated the in vivo feasibility of improving spatial resolution without increasing scan time in hyperpolarized ^{13}C flyback 3D-MRSI. In addition, we discussed the unique properties of the ℓ_1 reconstruction in compressed sensing, such as wavelet denoising and the tendency to lose low contrast features such as small peaks. This study has demonstrated feasibility and potential value for applying compressed sensing to hyperpolarized ^{13}C spectroscopy, and with further technique development even better performance is expected.

Chapter 4: *In Vivo* Carbon-13 Dynamic MRS and MRSI of Normal and Fasted Rat Liver with Hyperpolarized ¹³C-Pyruvate

The following chapter is adapted from: Hu et al. *In Vivo* Carbon-13 Dynamic MRS and MRSI of Normal and Fasted Rat Liver with Hyperpolarized ¹³C-Pyruvate. *Mol Imaging Biol* 2009; DOI: 10.1007/s11307-009-0218-z.

4.1 Background

Improved monitoring and measurement of metabolism in key biological processes, such as glycolysis and the citric acid cycle, both in the presence and absence of disease, have been long sought goals in the molecular and medical imaging communities. In particular, there has been great interest in pursuing carbon-13 NMR spectroscopy as a means of probing metabolic pathways to study normal metabolism and characterize disease physiology (50-52). While these *in vivo* studies of either endogenous or enriched ¹³C compounds have proved fruitful, such experiments have suffered from unique technical challenges, the most severe of which is low signal sensitivity, resulting in long acquisition times and large voxel sizes to obtain spectra with adequate signal-to-noise ratios (SNR) (50-52). However, a recent technological breakthrough, namely the development of techniques to maintain hyperpolarization of carbon-13 substrates in liquid state (9,10), has generated significant excitement for the prospect of rapid, high signal to noise

measurement of ^{13}C metabolism *in vivo*. Hyperpolarization (9,10) was achieved through the dynamic nuclear polarization (DNP) effect and thermal cooling, and liquid state (compatible with *in vivo* injection) polarization in excess of 50,000-fold was preserved using a novel rapid, heated dissolution process. The use of carbon-13 enriched substrates as molecular imaging agents with this technique is also attractive because ^{13}C is not radioactive and is only slightly heavier than carbon endogenous to the body, causing no significant isotope effects.

Initial applications of this technology were primarily focused on tracer based angiography (22) and perfusion mapping (53). More recent studies have included metabolic molecular imaging, using the metabolically active substrate [l- ^{13}C]pyruvate to examine its conversion to [l- ^{13}C]lactate, [l- ^{13}C]alanine, and ^{13}C -bicarbonate (14,15,23,24,54). Figure 4.1 provides a simplified summary of the metabolic pathways studied *in vivo* with hyperpolarized [l- ^{13}C]pyruvate. This hyperpolarized metabolic imaging approach enables not only the detection of the uptake of the injected, prepolarized substrate such as pyruvate, but also its conversion to lactate or alanine due to rapid exchange of the ^{13}C label (14) as catalyzed by lactate dehydrogenase (LDH) and alanine aminotransferase (ALT) respectively. In prior studies, significantly higher levels of [l- ^{13}C]lactate were found in implanted mouse tumors (14,54) and tumors in a mouse model of prostate cancer (15,16), which can be explained by the hyperglycolytic state and increased LDH activity common to most cancers (19,55). Furthermore, it was demonstrated that the rate constant for LDH flux decreased after drug treatment in an implanted tumor model (14).

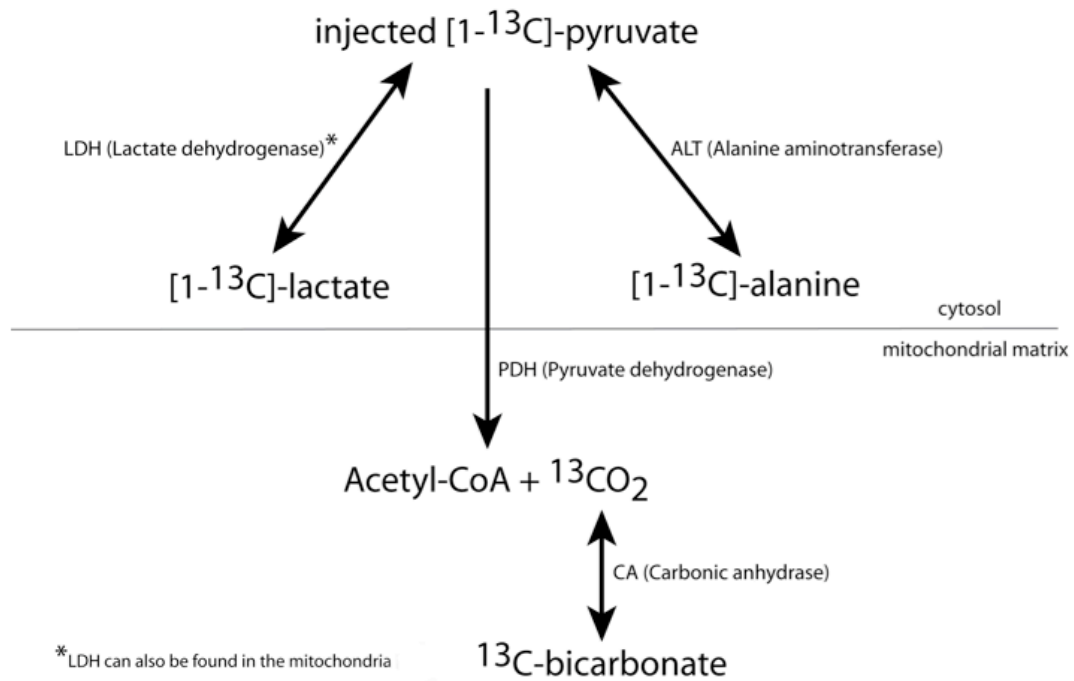


Figure 4.1: Diagram of metabolic pathways investigated with DNP hyperpolarized $[1-^{13}\text{C}]$ -pyruvate. Pyruvate/lactate conversion is catalyzed by lactate dehydrogenase (LDH), and pyruvate/alanine conversion is catalyzed by alanine transaminase (ALT). Pyruvate is irreversibly converted to acetyl-CoA and CO_2 by pyruvate dehydrogenase (PDH), and CO_2 is in a pH-dependent equilibrium with bicarbonate.

Thus, using hyperpolarized MRI technology to monitor LDH mediated lactate conversion could ultimately become a clinically viable metabolic molecular imaging method for measuring disease progression and tumor response to therapy as a complementary addition to anatomic imaging and ^1H MRS/MRSI. In cardiac research with isolated rat heart and *in vivo* experiments, others have demonstrated

the ability of hyperpolarized ^{13}C to directly evaluate pyruvate dehydrogenase (PDH) flux by way of bicarbonate conversion (56,57). PDH flux is a key step in normal and diseased cardiac metabolism, and there has been an initial report of altered bicarbonate levels during ischemia in the pig heart (58) and in a rat model of diabetes (57). Although all of the above metabolic imaging studies used [1- ^{13}C]pyruvate, hyperpolarization of other molecular agents is also possible. For example, hyperpolarized [1- ^{13}C]lactate can be used to examine the LDH back reaction (59). In addition, hyperpolarized bicarbonate ($\text{H}^{13}\text{CO}_3^-$), which converts to $^{13}\text{CO}_2$ in a pH dependent manner governed by the reaction catalyzed by the enzyme carbonic anhydrase, can be used to image pH (60), and this has great clinical potential because many disease processes, such as cancer, exhibit abnormal pH (61).

The initial research studies applying hyperpolarized ^{13}C metabolic imaging have focused on animal studies of cancer and cardiac metabolism, as described above. Thus far, there have been no published reports focusing on the investigation of liver metabolism with hyperpolarized ^{13}C technology. Therefore, the goals of this study were to characterize normal liver metabolism with hyperpolarized ^{13}C slice localized dynamic spectroscopy and 3D-MRSI and to investigate the ability of this technique to detect a change in metabolic state, specifically fasting. Whereas others have isolated changes based on LDH and PDH activity, in this work we aimed to focus on detection of alanine levels following injection of hyperpolarized pyruvate to probe ALT activity in the fasted state. Serum ALT levels have been shown to change in many liver diseases (62), so therefore ALT mediated flux could be an additional biomarker of interest for liver disease.

4.2 Methods

4.2.1 Overview

The overall process for the hyperpolarized imaging experiments was as follows: prepare a sample to be polarized, polarize with a DNP polarizer, perform anatomical imaging of the rat while waiting for the polarization to build up, dissolve and eject a liquid sample from the polarizer, inject the sample into a rat inside a clinical MR scanner, and perform either slice dynamic spectroscopy or 3D-MRSI. A total of 20 rat hyperpolarized MR experiments were conducted (5 normal dynamic, 5 fasted dynamic, 5 normal MRSI, 5 fasted MRSI).

4.2.2 Polarizer and Preparations

A HyperSense DNP polarizer (Oxford Instruments, Abingdon, UK) was used in this study. Following previously described methods (9,10), 32 μL (about 40 mg) of [l - ^{13}C]pyruvic acid (Isotec, Miamisburg, OH) with 15 mM OX63 trityl radical (Oxford Instruments, Abingdon, UK) was polarized in a field of 3.35T at approximately 1.4 Kelvin by irradiation with 94.116 GHz microwaves. After approximately 1 hour when the solid state polarization neared its exponential asymptote, an aqueous solution with 5.96 g/L Tris (40 mM), 4.00 g/L NaOH (100 mM), and 0.1 g/L Na_2EDTA was injected into the DNP polarizer, heated, and used for rapid thawing and dissolution of the solid state sample. The amounts of solvent, NaOH, and Tris-buffer used were calculated to produce a final polarized sodium pyruvate concentration of 100 mM and a pH of approximately 7.6. After the rapid thawing, the dissolved material was ejected into a flask resting on ice. Immediately

thereafter, a small aliquot (~0.5 mL) of the hyperpolarized [l - ^{13}C]pyruvate solution was used to measure the level of polarization achieved in solution, and at the same time another ~2.4 mL were taken to the MR scanner to be injected into a rat over a 12 s period followed by a normal saline flush.

4.2.3 Animal Handling

All animal studies were carried out under a protocol approved by the UCSF Institutional Animal Care and Use Committee. Male Sprague-Dawley rats weighing ~300 grams were either allowed to feed freely on standard rat chow (normal, non-fasted) or had their food removed 24 hours before each hyperpolarized study (fasted). For each experiment, the rat was placed on a heated pad and anesthetized with isoflurane (2-3%). A catheter was introduced into the tail vein for the eventual intra-venous administration of hyperpolarized pyruvate solution, and the rat was transferred to a heated pad in the RF coil in the MR scanner. While in the scanner, anesthesia was maintained by a continual delivery of isoflurane (1-2%) via a long tube to a nose cone, with an oxygen flow of 1 liter/min. The rat's vital signs (heart rate and oxygen saturation) were continually monitored. Care was taken to ensure that body temperature was maintained at 37^o C throughout the imaging procedures by maintaining a flow of heated water through the pad underneath the rat.

4.2.4 MRI, MRS, and MRSI

All studies were performed using a 3T GE Signa™ scanner (GE Healthcare, Waukesha, WI) equipped with the MNS (multinuclear spectroscopy) hardware

package. The RF coil used in these experiments was a dual-tuned ^1H - ^{13}C coil with a quadrature ^{13}C channel and linear ^1H channel construction based on an earlier design (63) and used in prior hyperpolarized ^{13}C pyruvate rat imaging studies (24). The inner coil diameter was 8 cm, and the length of the coil was 9 cm to accommodate rats of varying size.

T_2 -weighted anatomical images were obtained in all three planes using a fast spin-echo (FSE) sequence. Axial and sagittal images were each acquired in approximately 10 minutes with a 10 cm FOV, 192 x 192 matrix, 2 mm thick slices and NEX = 6. Coronal images were acquired with a 12 cm FOV, 192 x 192 matrix, 1.5 mm thick slices and NEX = 6 with a scan time of 10 minutes. The total imaging time required to obtain images in all three planes was thus approximately 30 minutes.

For the slice localized liver dynamic MRS experiments, a double spin-echo pulse sequence with a 5 degree flip selective RF excitation pulse (15 mm axial slice localization) and a pair of non-localized 180 degree hyperbolic secant refocusing pulses was used (11). A TE of 35 ms (half-echo collected), a repetition time (TR) of 3 s and a readout filter of 5000 Hz / 2048 pts were used for these studies. The acquisition localized to a slice through the liver started at the beginning of a 12 second duration, manual injection of [l - ^{13}C]pyruvate into the rat tail vein.

The 3D ^{13}C MRSI data were acquired in 14 seconds (starting 25 seconds after the start of injection) with a slab selective variable small tip angle excitation pulse, double spin-echo refocusing pulses, and a flyback echo-planar readout trajectory (11,15). An 8 x 8 phase encoding matrix with a flyback echo-planar trajectory on the z-axis (8 x 8 x 16 effective matrix) was used with 10 mm x 10 mm x 10 mm spatial

resolution (1.0 cc voxel resolution) with an 80 mm x 80 mm x 160 mm FOV to cover the rat torso and abdomen. The flyback echo-planar trajectory was designed for a 581 Hz spectral bandwidth to include ^{13}C lactate, ^{13}C alanine, and ^{13}C pyruvate without spectral aliasing. A total of 59 readout/rewind lobes were included during each readout for a spectral resolution of 9.83 Hz. With a readout filter of 25,000 Hz / 2,538 points, 16 k-space points were acquired during each TR (12). The TE for the MRSI acquisition was 140 ms (readout was centered on the center of the second spin-echo, full echo collected), and the TR was 215 ms. As described previously (15), a variable flip angle (VFA) scheme (40), with increasing flip angle over time to compensate for the loss in hyperpolarized signal, was used in the *in vivo* experiments. Reordering of phase encodes to collect data near the k-space origin first was also employed as previously (15).

4.2.5 Data processing

Figure 4.2 shows an example of the dynamic and spectral parameters for data processing in the slice MRS and 3D-MRSI experiments. The MRS example comes from data plotted in Figure 4.3, and the 3D-MRSI example comes from a voxel from Figure 4.5. Dynamic MRS data, processed with MATLAB™, were apodized in the time domain with a 10 Hz Lorentzian filter, Fourier transformed along the time dimension, and taken from the resulting magnitude spectra.

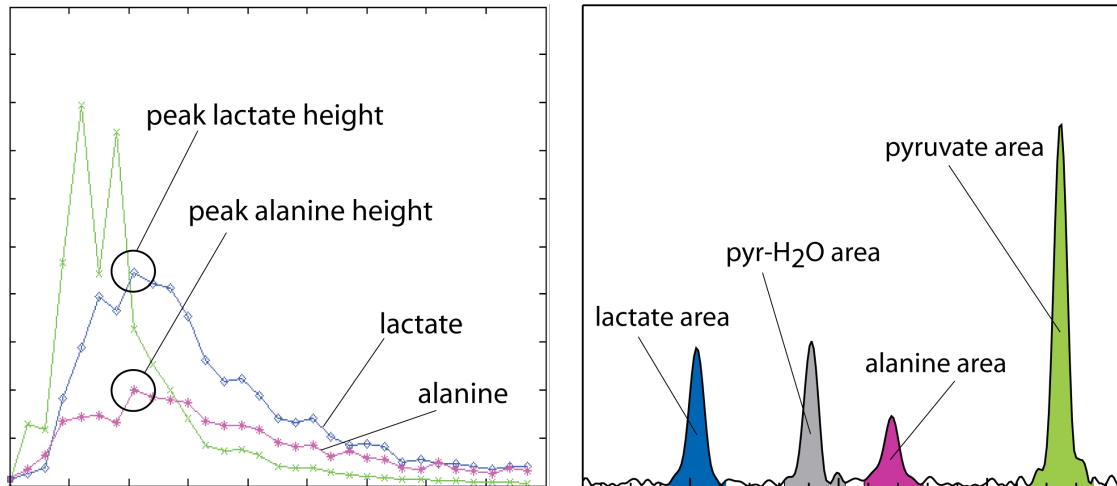


Figure 4.2: Example demonstrating the quantification procedures for slice MRS and 3D-MRSI. ^{13}C -lactate and ^{13}C -alanine peak heights were important parameters in the final processed dynamic curves (left). The areas of hyperpolarized ^{13}C resonances in the 3D-MRSI spectra were used in quantitative comparisons (right). The MRS example comes from data plotted in Figure 4.3, and the 3D-MRSI example comes from a voxel from Figure 4.5.

Magnitude dynamic curves were obtained for pyruvate, pyruvate-H₂O, lactate, and alanine, from which peak lactate to alanine ratios were calculated (Figure 4.2 left). A non-parametric statistical test (used to avoid any normality assumptions), the Mann-Whitney Rank-Sum test, was used to compare the peak lactate to alanine ratio between normal and fasted groups. For 3D-MRSI acquisitions, the reconstruction and analysis procedures, described previously in more detail (11,15), were carried out with specialized custom MRSI software (41) as follows: 1) the raw flyback data were sub-sampled and ordered to obtain a 4D matrix of k-space data 2) each FID was apodized and a linear phase correction was applied to the spectral samples as

described in (12) to account for the tilted k-space trajectory characteristic of the flyback readout and 3) a 4D Fourier transform with zero-padding of the spectra was performed. From the processed 3D magnitude spectral data, for each rat, the voxels localized to non-vasculature liver tissue were identified from the proton anatomical images and the ^{13}C spectra with sufficient signal-to-noise ratios (>5) were quantified. For each liver voxel, the area under the spectral resonances of pyruvate, pyruvate- H_2O , lactate, and alanine were calculated, with the sum of these four areas defined as the total carbon area (Figure 4.2 right). Lactate area to total carbon area and alanine area to total carbon area were calculated for each voxel and then averaged over all selected liver voxels to derive the test statistics average lactate to total carbon ratio and average alanine to total carbon ratio. The Mann-Whitney Rank-Sum test was used to compare these test statistics between normal and fasted groups.

4.3 Results

4.3.1 Dynamic MRS of Normal and Fasted Rat Liver

Figure 4.3 shows representative dynamic curves from slices localized to the livers of normal and fasted rats. These final dynamic curves were derived from the stack plot insets in which each horizontal line in a stack plot represents a separate magnitude spectrum of the hyperpolarized species collected every 3 seconds.

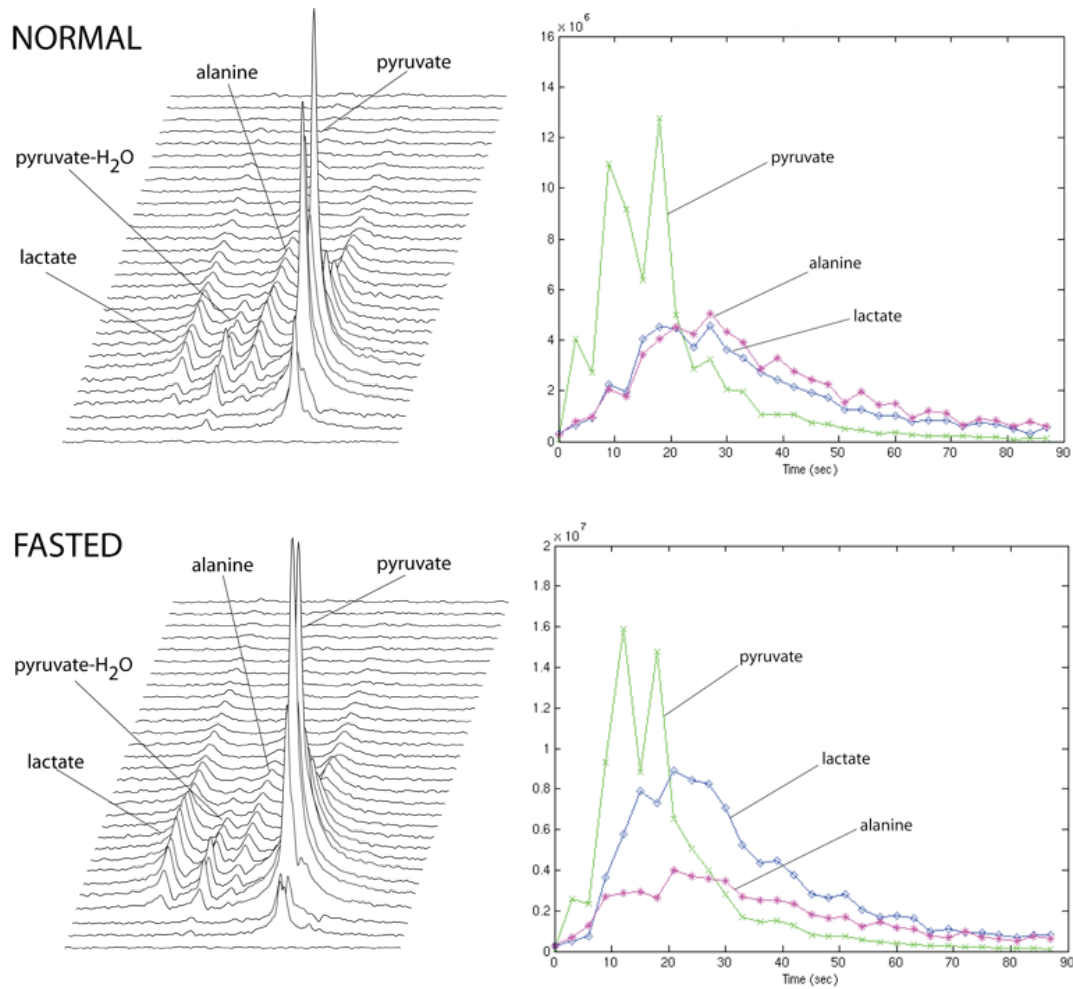


Figure 4.3: Comparison of normal (top) and fasted (bottom) rat liver representative dynamic data. The final processed dynamic curves were derived from the stack plots (left). The alanine and lactate levels were similar in the normal rat liver case (top right), but lactate levels were much higher than alanine levels in the fasted rat liver case (bottom right).

For easier viewing, the pyruvate curve has been scaled down by a factor of four and the non-metabolically active pyruvate-hydrate, which is in equilibrium with pyruvate, was omitted from the plots in Figure 4.3. In the dynamic curves, each

marked point represents the intensity of pyruvate (~171 ppm), lactate (~183 ppm), and alanine (~176 ppm) at that time point, i.e. a trace of those ridges in the associated stack plot, showing the uptake and conversion of pyruvate. Typically, the lactate and alanine curves showed a plateau around 20-30 seconds after injection, meaning the highest lactate and alanine SNR occurred in this range. This is important for picking an imaging window for the 3D-MRSI acquisitions, in which the SNR from each voxel is lower than in the slices in the MRS experiments. Qualitatively, the lactate and alanine curves in the normal rats had similar maximum amplitudes while there was a dramatic difference in the fasted rats. Figure 4.4 shows the peak lactate to alanine ratios for normal (1.18 ± 0.18 , [1.27, 1.39, 1.21, 1.09, 0.91]) and fasted rats (1.82 ± 0.40 , [2.28, 2.23, 1.54, 1.42, 1.64]).

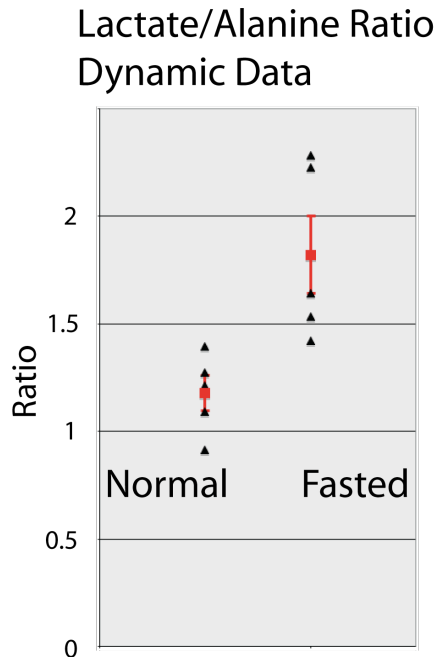


Figure 4.4: The data points and mean values for peak lactate to alanine ratios are shown from normal and fasted rat MRS slice acquisitions. Normal rat liver showed a

significantly lower lactate to alanine ratio ($P < 0.01$) than fasted rat liver. Mean/std - (normal: 1.18 ± 0.18 , fasted: 1.82 ± 0.40). Note: triangular markers show the collected data points and the square marker / error bars show the mean / standard errors.

Using a Mann-Whitney Rank-Sum test, there was a statistically significant difference in lactate to alanine ratio ($P < 0.01$). Also, these data demonstrated no overlap between the groups.

4.3.2 3D-MRSI of Normal and Fasted Rat Liver

Figure 4.5 shows representative axial slices from 3D-MRSI spectra with 1cm x 1cm x 1cm voxel resolution of normal and fasted rat liver (typically the rat liver spans a couple of slices). The proton images serve as anatomical references for the spectra and show vasculature regions in addition to liver parenchyma. All the fasted liver voxel spectra showed a high lactate to alanine ratio. Figure 4.6 shows the average lactate to alanine ratios for normal (1.18 ± 0.16 , [1.42, 1.12, 1.24, 1.11, 0.99]) and fasted rats (1.78 ± 0.15 , [1.85, 1.56, 1.85, 1.94, 1.65]) in a manner similar to Figure 4.4 except with 3D-MRSI data. The Figure 4.6 data corroborate the Figure 4.4 data, providing further evidence of an effect. In addition, the Figure 4.6 data show greater separation between the normal and fasted groups and less spread within the groups, which was probably due to selecting localized liver voxels instead of using tissue from a whole slice for the analysis.

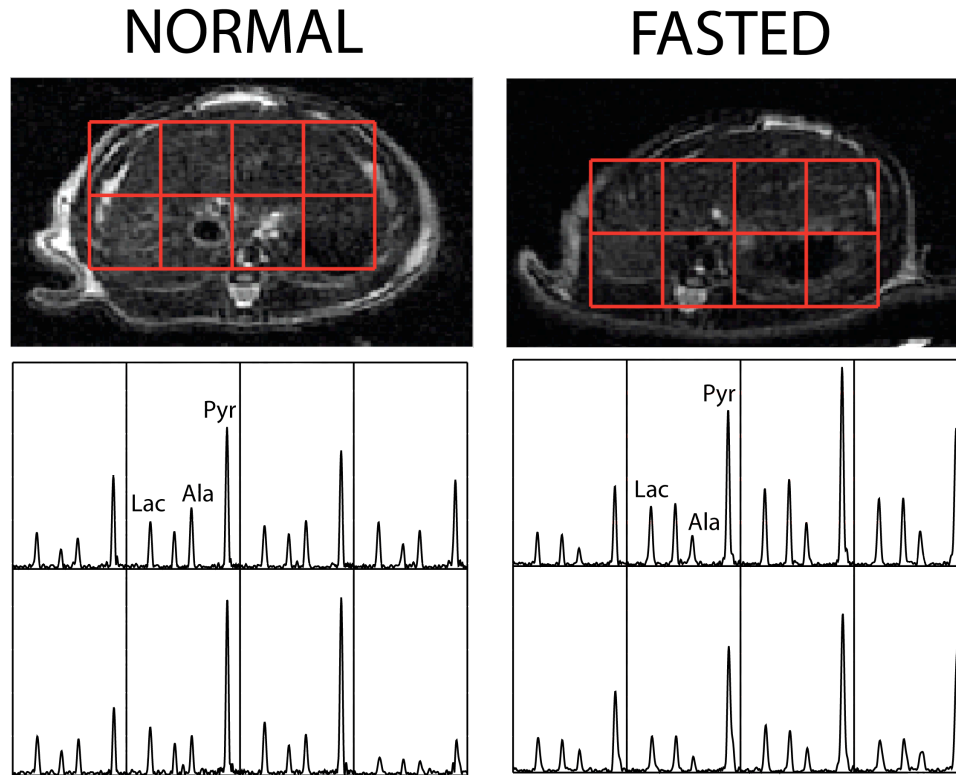


Figure 4.5: Comparison of representative liver slice spectra from 3D-MRSI acquisitions on normal (left) and fasted (right) rats. The spectra from normal liver showed similar levels of ^{13}C -lactate and ^{13}C -alanine. The spectra from fasted liver showed relatively lower levels of ^{13}C -alanine.

Qualitatively in the spectra, the liver lactate levels looked comparable between the normal and fasted states, but alanine seemed lower in the latter. As described in the methods section, the average lactate area to total carbon area and average alanine area to total carbon area ratios were calculated for each rat.

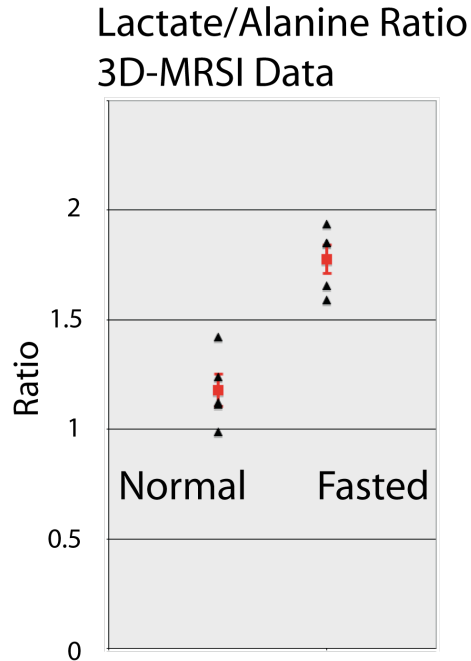


Figure 4.6: Lactate area to alanine area from 3D-MRSI studies (averaged over liver voxels per rat) of normal and fasted liver. Normal rat liver showed a significantly lower lactate area to alanine area ratio ($P < 0.01$) than fasted rat liver. These data corroborate the dynamic MRS data, with the means matching closely and indicating the same conclusion. Mean/std - (normal: 1.18 ± 0.16 , fasted: 1.78 ± 0.15). (Note: triangular markers show the collected data points and the square marker / error bars show the mean / standard errors.)

Figure 4.7 shows these lactate fractions (normal liver lactate to total carbon: 0.22 ± 0.026 , [0.264, 0.207, 0.211, 0.200, 0.229]; fasted liver lactate to total carbon: 0.23 ± 0.045 , [0.305, 0.232, 0.191, 0.212, 0.208]) and alanine fractions (normal liver alanine to total carbon: 0.19 ± 0.008 , [0.186, 0.185, 0.184, 0.190, 0.202]; fasted liver alanine to total carbon: 0.13 ± 0.026 , [0.165, 0.146, 0.103, 0.110, 0.126]).

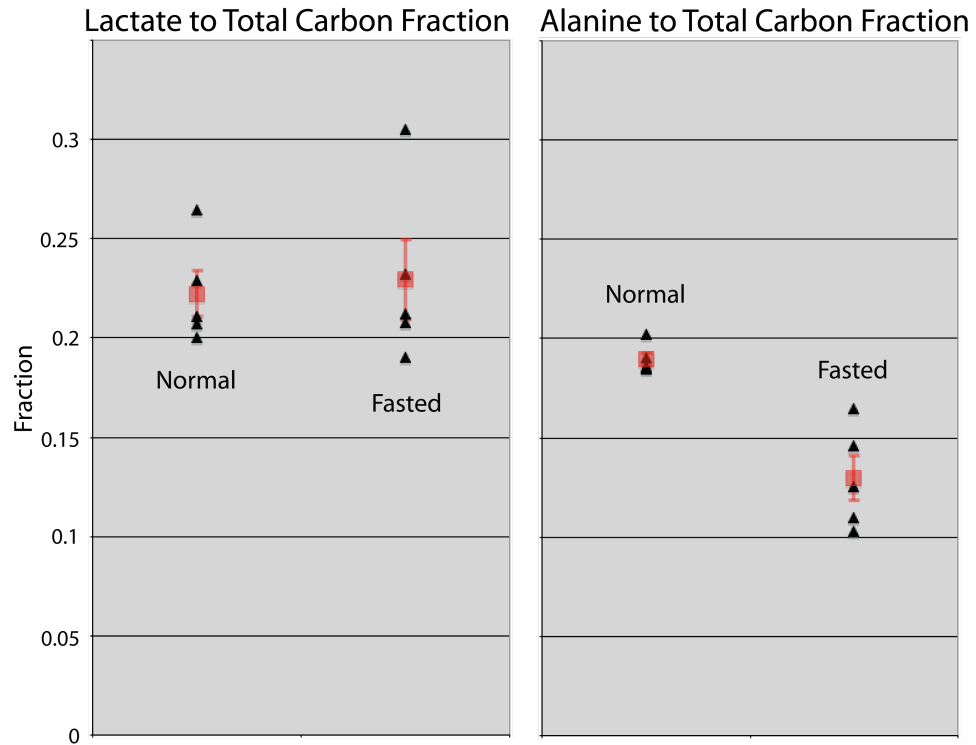


Figure 4.7: Lactate area to total carbon-13 fraction (left) and alanine area to total carbon-13 fraction (right) from 3D-MRSI studies (averaged over liver voxels per rat) of normal and fasted liver. The lactate to total carbon ratio was similar between normal and fasted groups, demonstrating that lactate levels were relatively constant. Mean/std - (normal: 0.22 ± 0.026 , fasted: 0.23 ± 0.045 , $P = 0.42$). The alanine to total carbon ratio was significantly lower for fasted rat liver. Mean/std - (normal: 0.19 ± 0.008 , fasted: 0.13 ± 0.026 , $P < 0.01$). Note: triangular markers show the collected data points and the square marker / error bars show the mean and standard errors. In addition, the five normal alanine to total carbon points overlap, thus obscuring some points.

Using a Mann-Whitney Rank-Sum test, there was no statistically significant difference in lactate to total carbon area between normal and fasted groups ($P =$

0.42), but there was a statistically significant difference in alanine to total carbon area between normal and fasted groups ($P < 0.01$). With the small sample size and low power, it is hard to say with complete certainty that fasting had no effect on lactate fraction, but the means/overlap in the data were strongly suggestive of lactate fraction being relatively constant for all rats. However, the decrease in alanine was statistically significant and specific, with no overlap between groups.

4.4 Discussion

There have been many recent reports that have shown hyperpolarized ^{13}C MR to be sensitive to physiological perturbations in enzyme-mediated flux involving LDH (14,15,54) and PDH (56,57). In this work, we have demonstrated that hyperpolarized ^{13}C MR is also sensitive to physiological perturbations in ALT flux and shown that it is possible to detect changes in metabolism in the liver with this technology. Day et al. (14) demonstrated that metabolic conversion from the injected pyruvate comes from rapid enzyme-mediated exchange of the ^{13}C label, i.e. isotope redistribution to endogenous pools of metabolites (14). It was specifically shown that the detected lactate spectra reflected the existing pool size of endogenous lactate. This study also demonstrated that by adding more unlabeled lactate to cells injected with hyperpolarized ^{13}C pyruvate, higher detected ^{13}C lactate was observed due to transfer of label to the unlabeled lactate pool (14). It was also shown that *in vivo* there was a decrease in detected lactate when the NADH coenzyme for LDH was inhibited, meaning flux toward lactate and thus transfer of hyperpolarized label to lactate was inhibited (14).

While prior published reports focused on the LDH pathway, this study demonstrated that the level of ^{13}C alanine produced in the murine liver from hyperpolarized pyruvate under the influence of ALT flux was sensitive to the physiologic perturbation of fasting. This alteration in alanine levels is supported by prior metabolic studies demonstrating that alanine is the key substrate utilized during gluconeogenesis, e.g. due to fasting (64). Gluconeogenic alanine conversion during fasting has also been shown in previous biochemical investigations involving perfused rat liver (65,66). By infusing labeled alanine, Cohen showed that alanine utilization and glucose production increased according to the degree of gluconeogenesis, specifically showing more glucose production in 24-hour fasted rats than 12-hour fasted rats and the highest production in drug-induced diabetic rats (65). In addition, Stromski et al. observed *in vivo* glucose production from alanine (67). Thus, the finding that alanine levels changed during fasting has been demonstrated in prior biochemical studies, but what is new in this study is the demonstration that this alteration can be detected *in vivo* using an MR metabolic imaging technique.

Hyperpolarized technology for the measurement of ^{13}C metabolic flux has many advantages, including high SNR, virtually zero background signal, and large chemical shift dispersion. The use of ^{13}C molecular imaging agents has the additional benefits of no radioactivity and no heavy isotope effects (e.g. deuterium which has twice the atomic weight of hydrogen). The method is general in the sense that many metabolic pathways could be probed, especially with the continued development of preparations for the hyperpolarization of agents other than pyruvate (59,60).

Hyperpolarized spectroscopy with ^{13}C pyruvate does employ injections of a pyruvate bolus well exceeding physiological concentrations. Regardless of the supraphysiological levels of the injected substrate, the reactions involving pyruvate have already shown promise in the assessment of glycolysis through LDH (14,15,54) and cardiac metabolism through PDH (56,57). The pyruvate to lactate pathway is extremely important for cancer applications because of the high lactate flux found in most tumors as dictated by the Warburg principle (19). For liver disease, flux through the ALT pathway might also have medical relevance. Clinical liver function tests routinely use measurements of ALT levels in the blood, with high levels correlating with disease. For example, high serum ALT levels (i.e. 2-fold to 10-fold normal) can indicate hepatitis, fatty liver, and hepatotoxicity (62). The presumed mechanism responsible for elevated levels of ALT is injury to hepatocytes and the consequent leakage of ALT into the bloodstream (62), making ALT levels dependent on the degree of liver injury. This does not necessarily represent a change in ALT concentrations in liver cells, but if there is indeed altered ALT and alanine concentrations in the liver resulting in altered flux of the ^{13}C label to alanine, then anatomically localized ^{13}C metabolic imaging with hyperpolarized pyruvate as the substrate could be a valuable technique to probe these changes. Using a hyperpolarized molecular probe to monitor changes in localized ^{13}C alanine distribution could potentially be a more specific assay than a serum ALT test, which can be complicated by high ALT levels occurring from nonhepatic causes (68). Additionally, using hyperpolarized [$1\text{-}^{13}\text{C}$]pyruvate to monitor ALT flux may be a useful biomarker of disease progression and response to therapy. The significant *in*

vivo change in liver metabolism during fasting observed in this study is an exciting initial demonstration of the potential value for liver hyperpolarized MR metabolic imaging, as well as an encouraging result for future liver disease studies using hyperpolarized MR.

In conclusion, normal and fasted rat liver were characterized with hyperpolarized ^{13}C slice-localized dynamic magnetic resonance spectroscopy and 3D magnetic resonance spectroscopic imaging. Fasted rat liver showed significantly lower levels of alanine in both the dynamic MRS and 3D-MRSI data, demonstrating the feasibility of hyperpolarized MR technology for detecting a change in metabolic state in the liver.

Chapter 5: Extensions to Compressed Sensing

Hyperpolarized ^{13}C Rapid MRSI

The following chapter is adapted from: Hu et al. 3D Compressed Sensing for Highly Accelerated Hyperpolarized ^{13}C MRSI with *In Vivo* Applications to Transgenic Mouse Models of Cancer. Magn Reson Med 2009; In Press.

5.1 Introduction

5.1.1 Motivation

High polarization of nuclear spins in liquid state through hyperpolarized technology utilizing dynamic nuclear polarization (DNP) has enabled the direct monitoring of ^{13}C metabolites *in vivo* at a high signal to noise ratio (SNR) (9,10). Metabolic imaging studies thus far have focused on injecting hyperpolarized [1- ^{13}C]pyruvate and observing its uptake and conversion to [1- ^{13}C]lactate, [1- ^{13}C]alanine, ^{13}C -bicarbonate, and $^{13}\text{CO}_2$ (14,15,23,24,54,56-58,69). These studies have shown the potential of hyperpolarized technology for the metabolic imaging of cardiac disease (57,58,69) and cancer (14-16,54). The hyperpolarized cancer studies have demonstrated that in tumors the lactate dehydrogenase (LDH) catalyzed reaction involving pyruvate and lactate results in dramatically higher levels of hyperpolarized ^{13}C lactate than in normal tissue (14-16,54). Mechanistically, LDH catalyzes rapid exchange of the ^{13}C label between pyruvate

and lactate; thus, detected ^{13}C lactate likely reflects the size of the preexisting endogenous lactate pool and LDH expression (14).

Hyperpolarization of clinically relevant substrates other than [1- ^{13}C]pyruvate is also an active area of research. Promising results have been reported for the hyperpolarization of [1- ^{13}C]lactate (59), [5- ^{13}C]glutamine (70), and ^{13}C bicarbonate (60). Regardless of the specific *in vivo* application or substrate being hyperpolarized, the overriding limitation in DNP hyperpolarized spectroscopic imaging is the rapid decay of the hyperpolarized signal, which decreases exponentially with the spin-lattice relaxation time (T_1) of the ^{13}C nucleus (on the order of 30 to 70 seconds for most substrates polarized). The hyperpolarized signal is also irretrievably lost due to saturation from RF excitation. These factors severely limit the number of phase encode acquisitions and thus the spatial resolution/coverage achievable, making accelerated imaging methods very important.

Our approach in this project was to apply compressed sensing, a recently developed technique based on random undersampling and a nonlinear reconstruction (25-28). Compressed sensing works well when underlying signals exhibit sparsity and have adequate SNR, but may fail if those conditions are not met (29). The key design challenge in implementing compressed sensing for specific MRI applications is the development of pulse sequences and acquisition schemes that incorporate “incoherent” sampling, which is achieved by pseudo-random undersampling (29). In a prior study, an initial design incorporated pseudo-random undersampling in one spatial dimension into a spectroscopic imaging sequence to

achieve two-fold acceleration for two-fold finer spatial resolution without increasing scan time (71) (Chapter 3 of this dissertation). In this project, this compressed sensing methodology was substantially enhanced to two spatial dimensions and developed a 7.53-fold accelerated sequence for 3D spectroscopic imaging, which was investigated through simulations, phantom testing, and *in vivo* experiments. In simulations, the limits of undersampling and the influence of noise on the compressed sensing nonlinear reconstruction were explored. We also applied this technique for hyperpolarized ^{13}C imaging research in transgenic mice that express human oncogenes and develop liver cancer, a new animal model in which the higher spatial resolution is particularly beneficial.

5.1.2 Compressed Sensing Literature

In essence, compressed sensing claims that signals that are sparse in some domain, not necessarily the time or frequency domains, can be recovered nearly perfectly even when sampled below the Nyquist rate. Candes et al. gave the following illustrative example (25,27): a length N discrete signal consisting of M non-zero points can be recovered exactly from K pseudo-random Fourier measurements where

$$K \geq \text{Const} \cdot M \log N \quad [5.1]$$

and the solution is found by solving the convex minimization problem

$$\min \sum_n |g[n]| \quad \text{s.t.} \quad F_K \{g[n]\} = y \quad [5.2]$$

where F_K is the Fourier transform, $g[n]$ is the proposed reconstruction of the length N discrete signal, and y are the K measured Fourier coefficients. The precise number of measurements needed (Eqn. [5.1]) depends strongly on the sparsity of the signal and weakly (logarithmic) on its size, and generally (for most pseudo-random sampling patterns) falls well below the number of samples required by the Nyquist criterion. In practice, a reasonable way to determine the extent to which a signal can be undersampled is through simulation. Eqn. [5.2] states that the correct algorithm to reconstruct the undersampled signal consists of finding a solution $g[n]$ with minimum ℓ_1 -norm in a sparse domain, with the constraint that it be consistent with the actual collected data (i.e. the Fourier coefficients of the reconstructed signal at positions where measurements occurred ($F_K\{g[n]\}$) should match the actual measured coefficients y). Real world signals usually exhibit the most sparsity in some domain other than the object domain, e.g. the wavelet domain, in which case the ℓ_1 -norm of the wavelet transform of $g[n]$ would be minimized (27-29). In addition, for real world signals with noise, the data fidelity constraint is modified by allowing $F_K\{g[n]\}$ to be within some noise standard deviations of y . Furthermore, as intuitively expected, reconstructions fail at very low SNR conditions where noise (in the sparse transform domain) dominates the signal (29). Again, the simulation approach was taken to evaluate the effects of noise. The last practical requirement, and the most important in terms of implementing compressed sensing for magnetic resonance imaging, is that the undersampled measurements K be acquired in a pseudo-random pattern (29). This can be interpreted as requiring the aliasing from undersampling to spread out randomly and incoherently so that minimal

interference with the underlying signal of interest occurs (29). In short, the practical requirements for applying compressed sensing are: 1) sparsity of the signal 2) adequate SNR and 3) random undersampling.

5.1.3 Hyperpolarized Carbon-13 Signal

Hyperpolarized ^{13}C MR spectroscopic imaging has several features that make it an excellent application for compressed sensing. First, hyperpolarized signals exhibit fundamental sparsity because typical spectra contain only a few peaks due to virtually no background interference from natural abundance carbon compounds (9,10). Second, with the >50,000-fold increase in signal due to hyperpolarization (9,10), spectra typically have high SNR. However, the rapid signal decay means data should be sampled quickly, i.e. in the limited time window during which SNR is high. Under conditions such as these, compressed sensing—a fast sampling strategy that works best for sparse and high SNR data—is very appropriate.

5.1.4 Simulation 1: Limits of Undersampling without Noise

To verify that typical hyperpolarized spectra have sufficient sparsity for highly accelerated compressed sensing acquisitions, undersampling with various acceleration factors was simulated (in the absence of noise for the first simulation), and errors for the reconstructions were recorded. The reconstruction methodology (also described in the methods section) was adopted from Lustig et al. (29). Briefly, the reconstruction software (based on SparseMRI: [75](http://www-</p></div><div data-bbox=)

mrsrl.stanford.edu/~mlustig/software/) implemented a nonlinear conjugate gradient algorithm for the solution of the following optimization problem:

$$\underset{m}{\operatorname{argmin}} \|F_u(m) - y\|_2 + \lambda \|\psi(m)\|_1 + \alpha TV(m) \quad [5.3]$$

Eqn. [5.3] formulates Eqn. [5.2] in so-called Lagrangian form, with the first term representing the data fidelity constraint in Eqn. [5.2], the second term representing the ℓ_1 -norm in Eqn. [5.2], and the third term representing a total variation penalty (ℓ_1 -norm of spatial finite-differencing) used to enforce some edge-preserving smoothness in the final solution (29). The weights given to ℓ_1 -norm minimization and smoothness can be manipulated by adjusting λ and α respectively, which also implicitly weights data fidelity.

The simulated data set shown in Figure 5.1a was created by thresholding the peaks from a ^{13}C phantom 3D-MRSI acquisition to remove the noise and then giving the peaks linewidths similar to those observed in phantom and animal experiments. The data dimensions for the simulated data set were 64x16x16x16 in f/x/y/z, with three of the z slices containing spectra (Figure 5.1a shows just one slice). The ^{13}C simulations/phantom contained pyruvate, pyruvate-hydrate, alanine, and lactate—the metabolites observed in actual *in vivo* hyperpolarized spectra with [1- ^{13}C]pyruvate as the injected substrate. This method for creating a simulated data set facilitated the replication of conditions from phantom experiments, including spatial resolution for testing of reconstruction of high spatial frequency components, making it straightforward to show that simulations matched experimental acquisitions with real MR hardware and pulse sequences. For these simulations, k-

k_x - k_y (64x16x16) were undersampled in a pseudo-random fashion except for the center 64x4x4 of k_f - k_x - k_y , which were fully acquired.

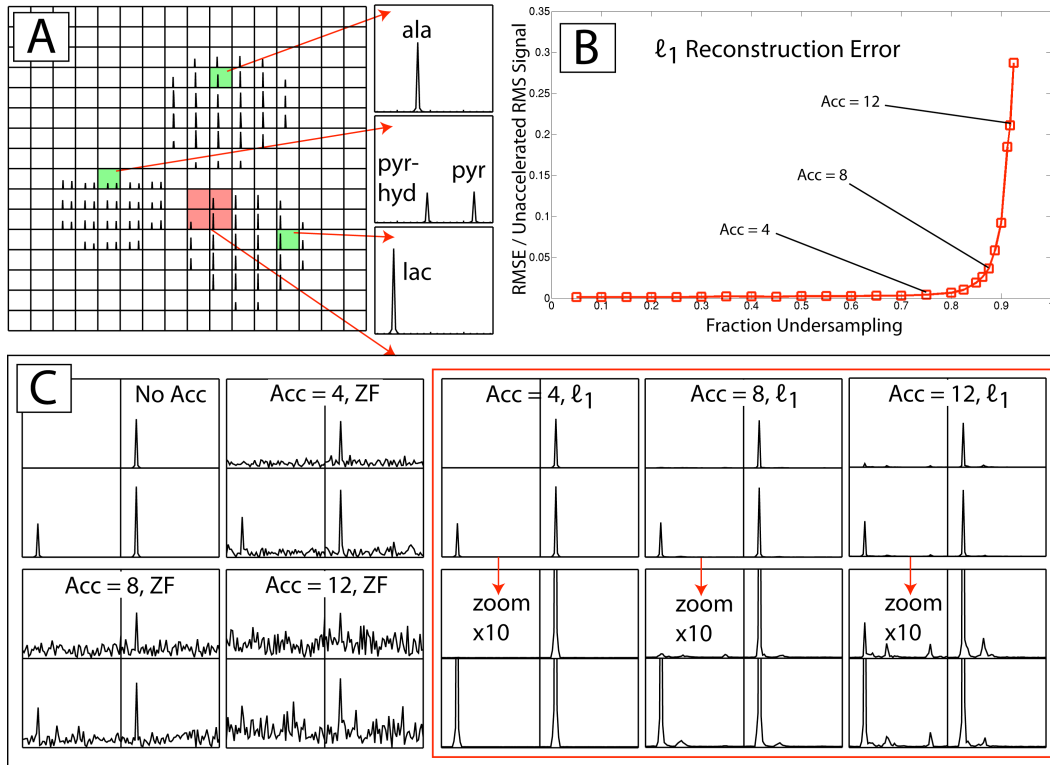


Figure 5.1: A) Simulated data set created by thresholding the peaks from a ^{13}C phantom 3D-MRSI acquisition to remove the noise and then giving the peaks a realistic linewidth. The data set contained three regions, each with different chemical species. B) The simulated data set was randomly undersampled with different undersampling factors, and ℓ_1 reconstructions were computed. The RMS errors between ℓ_1 reconstructed data and unaccelerated data were very low for a wide range of accelerations. C) Comparison of peaks from selected voxels. Zero-fill (linear) reconstructions exhibited incoherent aliasing that had a noise-like appearance and

increased with higher undersampling. ℓ_1 nonlinear reconstructions with accelerations as high as 8 were nearly perfect.

Fully sampling the high energy/SNR center of k-space, i.e. variable density sampling, has been empirically determined to enhance compressed sensing reconstructions (29). The readout dimension, k_z , was fully sampled without lengthening scan time using an echo-planar flyback scheme (described in the following sections). Figure 5.1b shows RMS errors between undersampled data sets and the original, with normalization by the RMS value for the original

$$\left(\sqrt{\frac{1}{n} \sum_{i=1}^n (x_{recon,i} - x_{original,i})^2} / \sqrt{\frac{1}{n} \sum_{i=1}^n x_{original,i}^2} \right).$$

As shown in Figure 5.1b, increasing the undersampling increased the reconstruction error in the ℓ_1 compressed sensing reconstruction. The RMSE for the ℓ_1 reconstruction rose rapidly starting at approximately 85% undersampling, indicating that the reconstruction started to break down due to an insufficient number of k-space samples. Figure 5.1c shows a comparison of spectra from unaccelerated, zero-fill x4 accelerated, zero-fill x8 accelerated, zero-fill x12 accelerated, ℓ_1 x4 accelerated, ℓ_1 x8 accelerated, and ℓ_1 x12 accelerated data sets. (Note: for the zero-fill reconstructions, density compensation was applied to the k-space points from undersampled regions. This was not needed for the compressed sensing acquisitions because the ℓ_1 algorithm synthesized the missing k-space data.) As expected, the zero-fill reconstructed spectra exhibited incoherent aliasing demonstrating a noise-like appearance. The ℓ_1 nonlinear reconstruction removed this incoherent aliasing, as shown on the right side of

Figure 5.1c. As shown in Figure 5.1c, the x4 accelerated ℓ_1 reconstruction was practically perfect, and the x8 accelerated ℓ_1 reconstruction yielded almost imperceptible distortions. The λ and α parameters in Eqn. [5.3] were chosen empirically (0.0005 and 0.0001 respectively), and over a reasonably broad range did not have a significant effect on reconstruction accuracy (data not shown). Note: the λ and α values are those used in the SparseMRI software package (29) (<http://www-mrsrl.stanford.edu/~mlustig/software/>); in other words, they are the λ and α weights in Eqn. [3] when the object domain signal (m) is normalized to have unity magnitude. The practical limitations of compressed sensing have been documented (27-29), but these application specific simulations with realistic data and concrete matrix sizes are important to provide a sense of the range of feasible accelerations.

5.1.5 Simulation 2: Reconstruction with Noise

The second set of simulations dealt with noise. The top left corner of Figure 5.2a shows the noiseless slice data from Figure 5.1a. The three rows show the alanine, pyruvate/pyruvate-hydrate, and lactate regions respectively. The first column of Figure 5.2a gives an example of magnitude spectra before undersampling, with additive white Gaussian noise (AWGN) added such that the maximum signal voxel had an SNR of 50 (SNR defined as the magnitude peak height divided by the standard deviation in the magnitude noise signal). The second column shows magnitude spectra after factor of 4 random undersampling and an ℓ_1 reconstruction

using the same parameters as in the first set of simulations. The last column gives the magnitude difference between the first two columns.

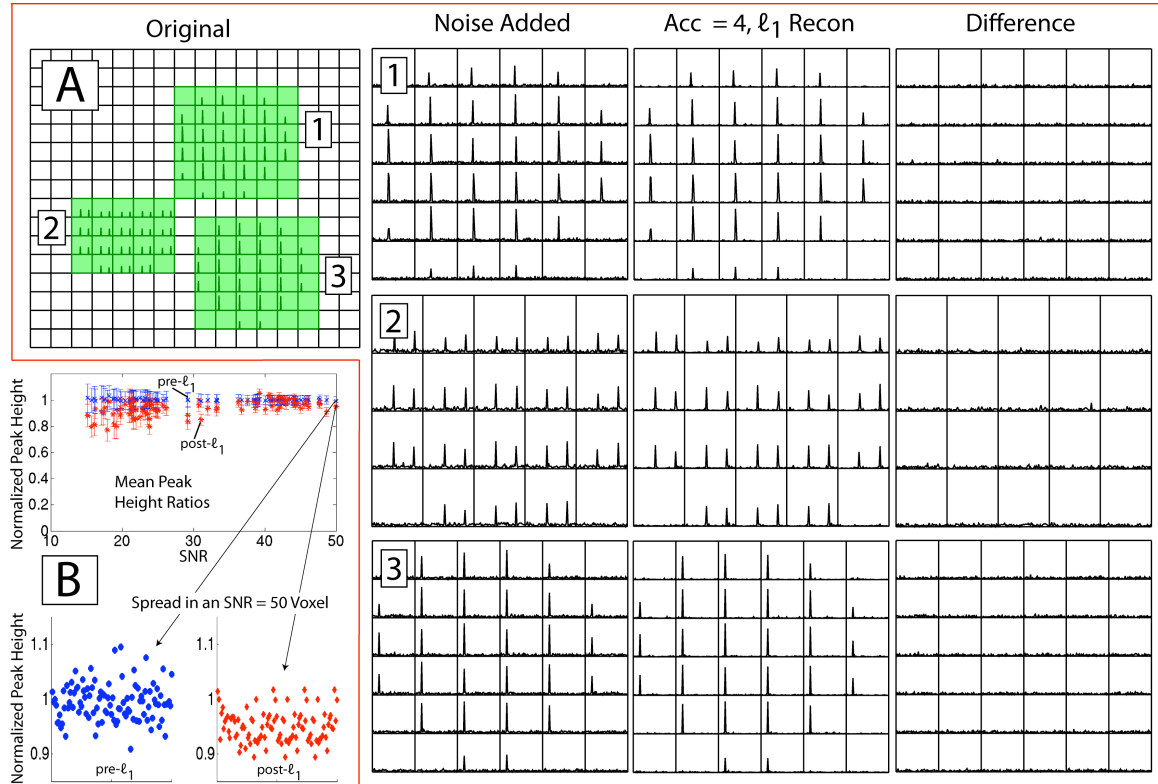


Figure 5.2: A) Reproduction of the noiseless data set from Figure 1a. The three regions containing 1) alanine 2) pyruvate/pyruvate-hydrate and 3) lactate respectively are highlighted. On the right side, in the first column, those three sets are shown again but with additive white Gaussian noise added. In the second column, an ℓ_1 reconstruction with factor of 4 undersampling of the noisy data is shown. The third column shows the magnitude difference. B) The noise simulation in part A) was run 100 times with distinct noise patterns each time. For each of the peaks across the many voxels, and for both the noise added ($pre\text{-}\ell_1$) and noise added with factor of 4 undersampling with ℓ_1 reconstruction ($post\text{-}\ell_1$) data sets, the mean/standard deviation of the ratio of peak

height to true-noiseless-peak-height was plotted. All pre- ℓ_1 ratios were centered on unity regardless of signal strength, but the post- ℓ_1 ratios were slightly skewed downward for peaks that had low starting SNR. The bottom part shows a scatter plot of pre- ℓ_1 and post- ℓ_1 peak height to true-noiseless-peak height ratios for a selected peak over the 100 runs.

The noisy data and the ℓ_1 reconstructed data agreed very well, with most peaks in the undersampled data set reproduced accurately. For each peak in each voxel, the ratios for noise-added-peak-height over noiseless-true-peak-height (pre- ℓ_1) and ℓ_1 -reconstructed-peak-height over noiseless-true-peak-height (post- ℓ_1) were computed, and the noise simulation was run 100 times with distinct random noise patterns each time. The means/standard deviations for the pre- ℓ_1 and post- ℓ_1 ratios for every peak were then computed and plotted (top of Figure 5.2b). A mean close to unity signifies agreement on average with true peak height, which, as shown by the blue x marks in the top of Figure 5.2b, was the case for all noisy peaks regardless of SNR before the ℓ_1 reconstruction. The red stars in the top of Figure 5.2b show the post- ℓ_1 mean ratios for all peaks in the data, with values for high SNR peaks (SNR > 25 after adding AWGN and before undersampling) coming close to unity (0.96 ± 0.04) and those for lower SNR peaks (SNR < 25) systematically reduced slightly (0.91 ± 0.07). (Note: in order to make the comparisons between unaccelerated and accelerated data sets equal in terms of SNR, the SNR for the ℓ_1 runs was scaled up to adjust for the SNR lost from undersampling.) The bottom of Figure 5.2b illustrates reconstruction variability in peak ratios over 100 runs for a particular peak in a

particular voxel, specifically the SNR 50 peak whose peak height means are indicated in the top of Figure 5.2b. The reduced peak ratios are most likely due to a slight bias in the ℓ_1 reconstruction itself. Specifically, it was shown that ℓ_1 -norm minimization is equivalent to iterative soft thresholding, which has a bias toward shrinking detected components (35). One possible future way to reduce the bias could be to try newer compressed sensing reconstructions, such as an iteratively reweighted ℓ_1 method proposed by Candes et al. (72)

5.2 Methods

5.2.1 Pulse Sequence Design for Highly Accelerated 3D-MRSI

To implement compressed sensing for MRSI, the main design challenge was to incorporate random undersampling into a practical pulse sequence. The starting point was a double spin-echo ^{13}C sequence (11) with phase encoding in x and y and a flyback echo-planar spectroscopic imaging (EPSI) readout (12) in z and frequency. (In the flyback readout, the time between flyback lobes controlled spectral bandwidth, and the number of lobes in conjunction with spectral bandwidth determined the spectral resolution possible.) To take advantage of the sparsity in hyperpolarized data, as was done in the simulations, a method was needed to undersample three k-space dimensions, including the frequency dimension (containing sparse spectra) but excluding the fully sampled k_z EPSI readout dimension. To accomplish this, the design trick of placing gradient blips during the rewind portions of the flyback readout was employed to randomly hop around in k-space (71). Figure 5.3a shows the complete pulse sequence with double spin-echo

adiabatic refocusing pulses, flyback readout, and x and y gradient blips. (Note: the x and y gradient waveforms have been zoomed in vertically for viewing purposes.)

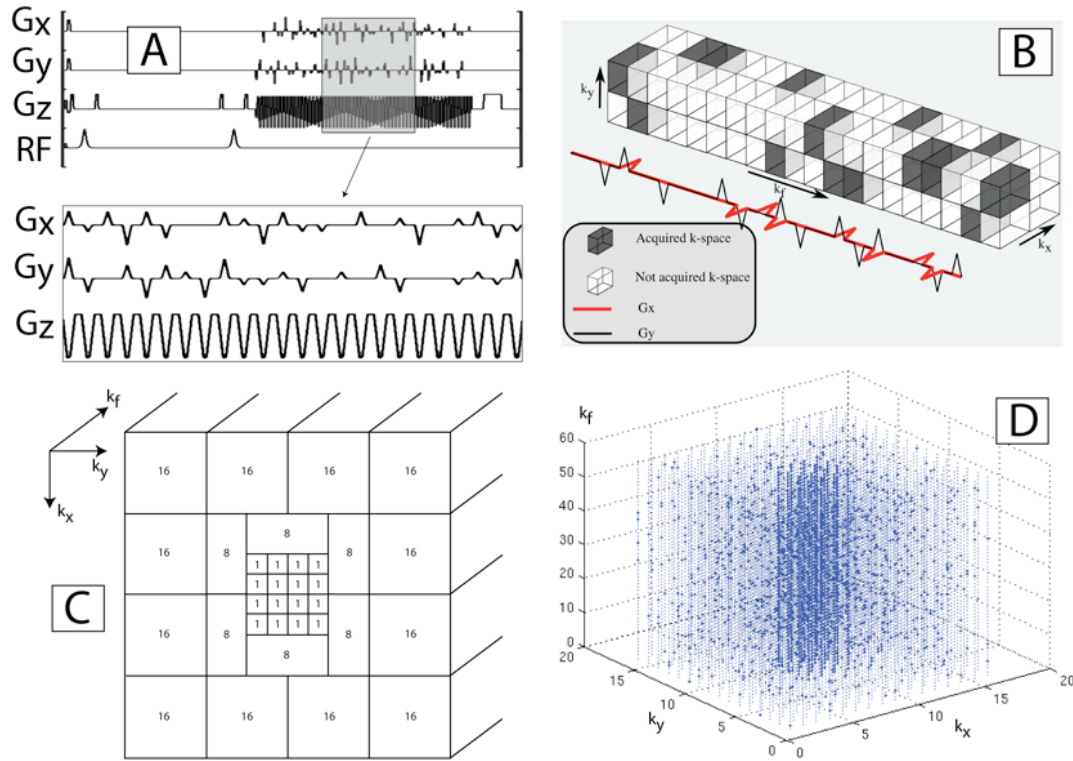


Figure 5.3: A) Compressed sensing 3D-MRSI pulse sequence. Phase encode localization occurred in x/y with flyback readout in z/f. Full echo data were collected by using twin adiabatic refocusing pulses. The key design trick was placing x/y gradient blips during the rewind portions of the flyback readout. The blip areas were integer multiples of phase encode steps, allowing for hopping around and random undersampling of k_f - k_x - k_y space. B) Illustration of random undersampling of a swath of k_f - k_x - k_y space using blips. The blips portioned out the acquisition over several lines in k-space during one TR. C) Depiction of variable density sampling resulting in a $\times 7.53$ accelerated sequence. Central regions of k-space were fully sampled, middle regions undersampled

by a factor of 8, and outer edges undersampled by a factor of 16. D) Resulting random undersampling pattern in k_f - k_x - k_y .

Figure 5.3b illustrates how such a blipped scheme can provide random undersampling of k_f - k_x - k_y space. In Figure 5.3b, the area of each x or y gradient blip equals the area in an x or y phase encode increment. In other words, Figure 5.3b shows a $num_lobes \times 2 \times 2$ region of k_f - k_x - k_y space where k_f data are read as time progresses and each x or y gradient blip moves the reading of k_f data up or down one phase encode step in k_x and k_y respectively. With the use of pseudo-randomly placed up/down x and y gradient blips, a region of k_f - k_x - k_y space covering 2×2 phase encodes can be randomly undersampled in the time of one TR—a factor of 4 acceleration. For a 16×16 phase encode matrix with a fully sampled 4×4 central region, the total acceleration would be $\frac{16 \times 16}{4 \times 4 + (16 \times 16 - 4 \times 4)/4} \approx 3.37$, which is

slightly less than 4. The use of the blipped design trick accomplished the counterintuitive goal of skipping around and undersampling in the time (k_f) dimension itself. If blip areas were allowed to equal the area of two or more phase encode steps, then even larger k_x - k_y blocks could be undersampled and acceleration increased. Thus, to undersample an $m \times n$ block of k_x - k_y space, the x and y gradient blips must go up to the areas of $m - 1$ and $n - 1$ phase encode increments respectively. Figure 5.3a and 5.3c illustrate this idea by showing blips of three different amplitudes and 2×4 , 4×2 , and 4×4 k_x - k_y blocks. The design in Figure 5.3c produces the random undersampling pattern shown in Figure 5.3d, which resulted

in an acceleration factor of 7.53. The methodology presented here, with the addition of blips on multiple gradient axes and arbitrary blip areas, significantly advanced the initial design method in which acceleration was limited to a factor of 2. Experimental validation of these new designs is described in the following sections.

5.2.2 Pulse Sequence and Hardware

All experiments were performed on a General Electric EXCITE 3T (Waukesha, WI) clinical scanner equipped with 40 mT/m, 150 mT/m/ms gradients and a broadband RF amplifier. The RF coils used were custom built, dual-tuned $^1\text{H}/^{13}\text{C}$ transmit/receive designs that were employed in previous studies (15,16,24,59). For all experiments, carbon-13 spectra were overlaid on T_2 -weighted proton images collected with a fast spin-echo sequence. Acquisition parameters for phantom axial proton images were: a FOV of 11cm, 256x192 matrix, 3mm slice thickness, and NEX = 6. Mouse proton axial images were acquired with a FOV of 8cm, 192x192 matrix, 2mm slice thickness, and NEX = 6. Coronal images for the mouse were the same except FOV was 10cm and slice thickness was 1.5mm. The ^{13}C 3D-MRSI spectra were acquired with the pulse sequence shown in Figure 5.3a. The base sequence with adiabatic refocusing pulses and flyback readout has been described in detail previously (11). In short, this sequence selects a slab in z, phase encode localizes in x and y, and uses a flyback waveform to read out full echo data in z and frequency for each x/y phase encode. Specific sequence parameters for phantom and *in vivo* experiments are given below. As was done previously (15,16,71), k_x - k_y data (in this case k_x - k_y blocks) were collected outward from the k-space origin in concentric

order. In addition, a variable flip angle scheme (40), i.e. increasing flip angle over time to compensate for the loss in hyperpolarized signal and ending with a 90 degree pulse, was used in the *in vivo* experiments. The actual n^{th} flip angle $\theta[n]$ precalculated by the source code for a given acquisition of N flips was as follows:

$$\theta[n] = \begin{cases} 90^\circ & \text{if } n = N \\ \arctan(\sin(\theta[n+1])) & \text{if } n < N \end{cases} \quad [5.4]$$

For example, in an acquisition with 64 readouts, $\theta[64] = 90^\circ$, $\theta[63] = \arctan(\sin(90^\circ)) = 45^\circ$, $\theta[62] = \arctan(\sin(45^\circ)) = 35.3^\circ$, ... $\theta[1] = 7.2^\circ$. Calibration for mouse scans was performed before each experiment using a small ^{13}C external standard placed with the animal in the coil. The blips in Figure 5.3a had a width of 0.8ms (time between flyback flat portions being 1.16ms), and their placement and amplitudes were set to achieve the desired sampling patterns.

5.2.3 Reconstruction Methodology

The steps to process undersampled ^{13}C 3D-MRSI data have been described previously (71). The major steps were as follows: 1) the readout data were reordered to pick out the data from flat portions of the flyback readout and organize all the data into a 4D k_f - k_x - k_y - k_z array 2) the missing k-space data in each undersampled k_f - k_x - k_y set were filled in with the iterative nonlinear ℓ_1 algorithm described previously (29) and 3) standard processing was performed, including apodization, linear phase correction for the flyback's tilted k-space trajectory (12), and a 4D Fourier transform. Step 2 was the additional component beyond conventional processing needed to account for the missing data from

undersampling. For all phantom and mouse experiments, the ℓ_1 reconstruction parameters were the same as for the simulations, namely $\lambda = 0.0005$ (wavelet transform weight) and $\alpha = 0.0001$ (total variation penalty weight).

5.2.4 Phantom Methodology

Figure 5.4 shows a proton image of a slice from the cylindrical phantom used to experimentally validate our acceleration schemes. The phantom contained three spheres filled with different ^{13}C -labeled compounds, pyruvate/pyruvate-hydrate in one, alanine in another, and lactate in the third. The validation consisted of comparing unaccelerated and accelerated 3D-MRSI acquisitions. For both, a flip angle of 10° , TE = 140ms, TR = 2s, in-plane FOV = 6cm x 6cm, 16x16 phase encode matrix, 1cm flyback z resolution, 581 Hz spectral FOV, 9.8 Hz spectral resolution, concentric phase encode order, and NEX = 16 were used with the sequence shown in Figure 5.3a. The accelerated acquisitions used the x3.37 and x7.53 undersampling designs.

5.2.5 *In Vivo* Methodology

All animal studies were carried out under a protocol approved by the UCSF Institutional Animal Care and Use Committee. For all *in vivo* experiments, a HypersenseTM DNP polarizer (Oxford Instruments, Abingdon, UK) was used. 24 μL (about 30 mg) of [^{1-13}C]pyruvic acid with 15 mM OX63 trityl radical, along with 0.5 mM (about 0.47 μL) of Prohance gadolinium for polarization enhancement (73), were polarized for one hour in a field of 3.35T at 1.4 Kelvin with irradiation by

94.097 GHz (determined by a frequency sweep) microwaves at 20 mW power. The dissolution medium consisted of an aqueous solution with 40 mM Tris, 80 mM NaOH, and 0.1 g/L Na₂EDTA. The final dissolved material had a concentration of 80 mM, pH ~7.5, and a polarization ~25% (measured by taking a small aliquot and injecting into a custom built polarimeter ~15 seconds after dissolution). 350 μ L were injected into mice through either a jugular or tail vein catheter followed by a 150 μ L saline flush. Detailed descriptions of our mice handling procedures, e.g. keeping animals warm and administering anesthesia, have been given previously (15,16). Two different animal models were used in our studies. The first was a transgenic adenocarcinoma of mouse prostate (TRAMP) model (42,43) that we have used previously for hyperpolarized ¹³C spectroscopic imaging studies of cancer (15,16,71). The other model was a Tet-o-MYC/LAP-tTA double transgenic mouse model of liver cancer in which the human MYC proto-oncogene is overexpressed only in the liver (74,75). Liver cancer is a new preclinical application for hyperpolarized ¹³C studies and is potentially an attractive clinical target for rapid hyperpolarized spectroscopic imaging. The x3.37 and x7.53 accelerated patterns described above were used in the *in vivo* experiments both to increase spatial resolution and decrease scan time. The ¹³C 3D-MRSI parameters were variable flip angle, TE = 140ms, TR = 215ms, in-plane FOV = 4cm x 4cm, 16x16 phase encode matrix, 5.4mm flyback z resolution, 581 Hz spectral FOV, 9.8 Hz spectral resolution, and concentric phase encode order. The lower resolution unaccelerated acquisitions used an 8x8 phase encode matrix.

5.3 Results

5.3.1 Phantom Results

Figure 5.4 shows a comparison of unaccelerated, x3.37 accelerated, and x7.53 accelerated acquisitions. The alanine sphere subset, with the frequency axis zoomed in, is also shown. The ℓ_1 reconstructed compressed sensing spectra were of high quality, matching up closely in spatial and spectral characteristics with the unaccelerated data. In addition, small peaks along the edges of the balls were accurately preserved. These peaks had SNRs on the order of 10 to 20 in the unaccelerated spectra.

5.3.2 *In Vivo* Results

Figure 5.5 shows *in vivo* validation of the x3.37 and x7.53 accelerated sequences in transgenic prostate cancer mice. Figure 5.5a compares a slice from an unaccelerated acquisition with 0.135 cm³ voxel size acquired in 14s with the same slice from a x3.37 accelerated acquisition with a quarter the voxel size acquired in 16s (~1.5 hours between acquisitions). As shown in Figure 5.5a, one benefit of the higher resolution afforded by the compressed sensing acquisition was better delineation of the outline of the mouse body. Even with the higher resolution, metabolic profiles were accurately preserved, as demonstrated by the highlighted voxels showing spectra from the same location for each acquisition.

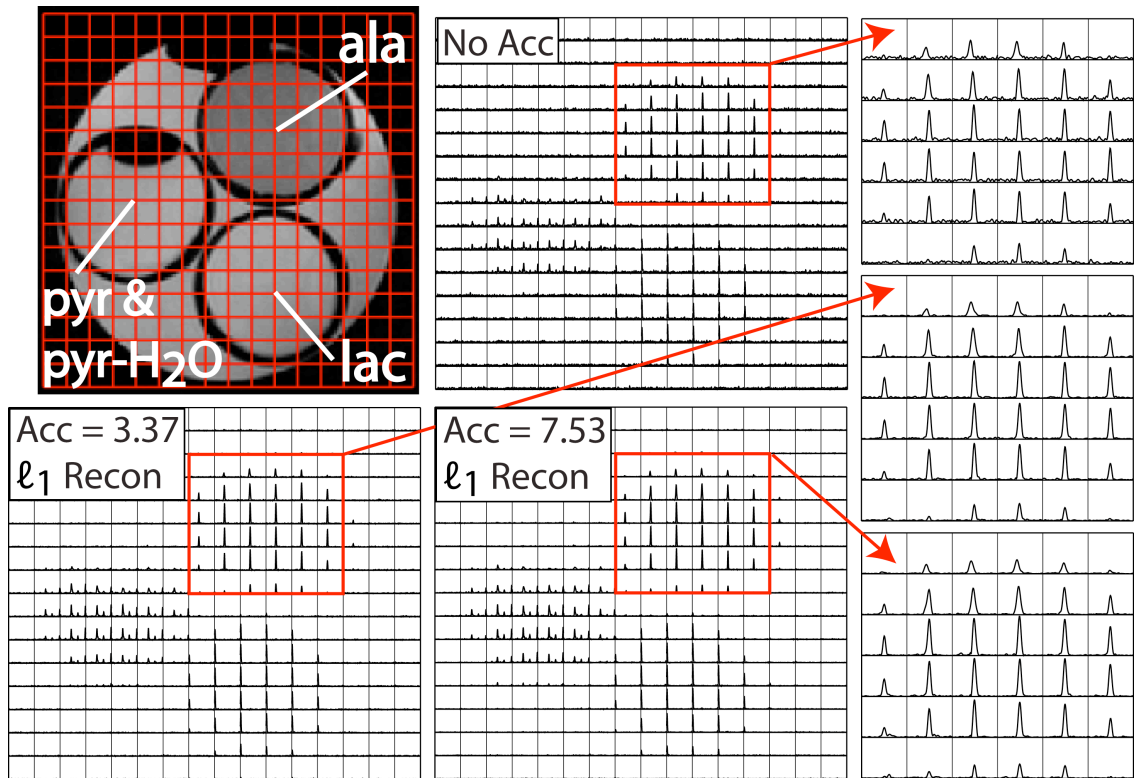


Figure 5.4: Results from phantom experiments. The upper left shows an image of a slice from a cylindrical phantom with spheres containing ^{13}C -labeled alanine, pyruvate+pyruvate-hydrate, and lactate. The adjacent boxes show comparisons of spectral grids from 3D-MRSI acquisitions with no undersampling, x3.37 undersampling, and x7.53 undersampling. The 16x16 voxels shown have 3.75mm x 3.75mm in-plane resolution. The 6x6 grids to the right show spectra from the alanine sphere only (frequency axis zoomed in). The ℓ_1 reconstructions for the accelerated acquisitions matched the unaccelerated acquisition, showing high spectral quality and the preservation of small peaks.

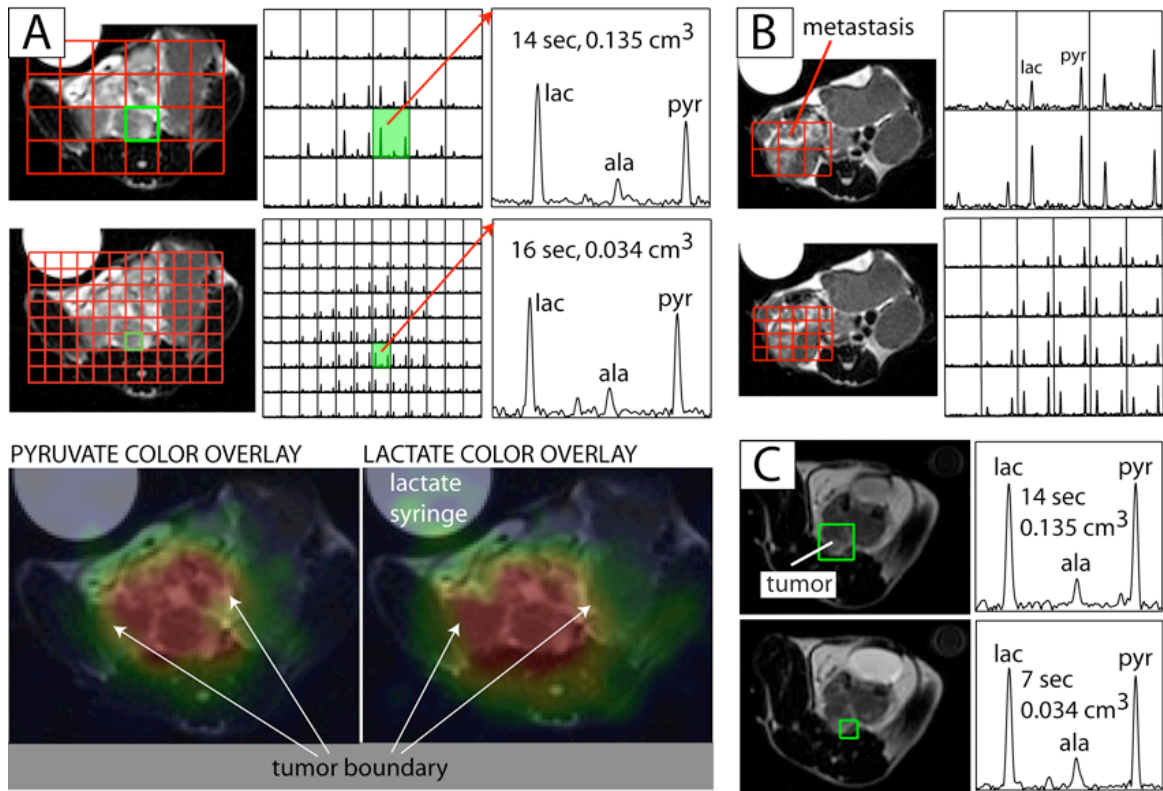


Figure 5.5: A) *In vivo* validation in a transgenic mouse model of prostate cancer showing a comparison of spectra from an unaccelerated acquisition and an accelerated one with a quarter the voxel size and acquired in about the same time. The accelerated acquisition with higher resolution allowed for better delineation of the mouse body and better depiction of tumor heterogeneity. The spectra in the accelerated acquisition were of high quality, and small peaks were preserved. The color overlay maps generated from the accelerated spectra show high intensity regions as brightly colored and highlight the spatial localization of metabolites according to tissue type. Tumor and non-tumor regions showed clear differences in metabolic profile, and the boundaries were clearly delineated. B) A comparison of spectra from a different slice in the same mouse with the higher resolution spectra depicting heterogeneity and the boundaries of a metastasis better than the lower

resolution spectra. The full 3D acquisition allowed for imaging disease in multiple slices. C) High quality spectra from a different prostate cancer mouse in which the $\times 7.53$ accelerated sequence was used to quadruple resolution and nearly halve acquisition time. Once again, small peaks were preserved.

Small peaks such as alanine were reproduced and, interestingly, in this example, pyruvate hydrate (peak between lactate and alanine) was seen in the compressed sensing voxel. The bottom part of Figure 5.5a shows pyruvate and lactate metabolite color maps generated from the accelerated spectra. Bright colors in the overlay map depict high signal intensity regions, allowing for easy visualization of the spatial localization of the metabolites. As demonstrated by these maps, pyruvate and lactate were localized to the tumor, and the tumor boundary was clearly delineated. Figure 5.5b shows a comparison of spectra from the kidney level in the same mouse where a metastasis was detected, once again demonstrating better delineation of the mouse body due to higher resolution and also better depiction of the heterogeneity in tissue that was previously obscured by partial voluming. Figures 5.5a-b highlight an advantage of full volumetric spectroscopic imaging—gathering data from multiple planes and allowing for investigation of the relationship between organs, tumors, and metastases in those separate planes. Figure 5.5c shows *in vivo* data collected from a different prostate cancer mouse, providing another example of high quality spectra obtained with the compressed sensing sequence. In the case of Figure 5.5c, the comparison was between a 0.135 cm^3 voxel from an unaccelerated

acquisition of 14s and a voxel a quarter the size in the same anatomic location from a x7.53 accelerated acquisition of 7s.

Figure 5.6 shows the first hyperpolarized spectroscopic images from a transgenic animal model of liver cancer (all examples with 0.034 cm³ resolution, x3.37 acceleration, and acquired in 16s). Figure 5.6a, depicting an early stage liver tumor in the upper left quadrant of the anatomic image, once again highlights the benefits of the enhanced resolution from accelerated imaging, showing the reduction of partial voluming with smaller voxels. There was a clear difference between the tumor voxels (upper left in the spectral grids), which exhibited a high lac/pyr ratio, and the normal tissue voxels (lower right in the spectral grids), which showed the opposite metabolic profile—a low lac/pyr ratio. The other voxels showed an intermediate pattern, with lactate and pyruvate levels being comparable, presumably due to the tissue in those voxels containing a mixture of tumor and normal cells. Figure 5.6b, showing another 3D-MRSI data set from the same mouse but acquired on a different date, underscores the abnormal metabolic profile in tumor tissue. It presents a coronal overlay slice of the data to highlight the dramatically elevated lactate in the tumor, which was not found in other organs, such as the kidneys. Figure 5.6b highlights the fact that with 3D-MRSI, where data are acquired in three spatial dimensions, overlays in any of the anatomical planes—axial, coronal, and sagittal—are readily available.

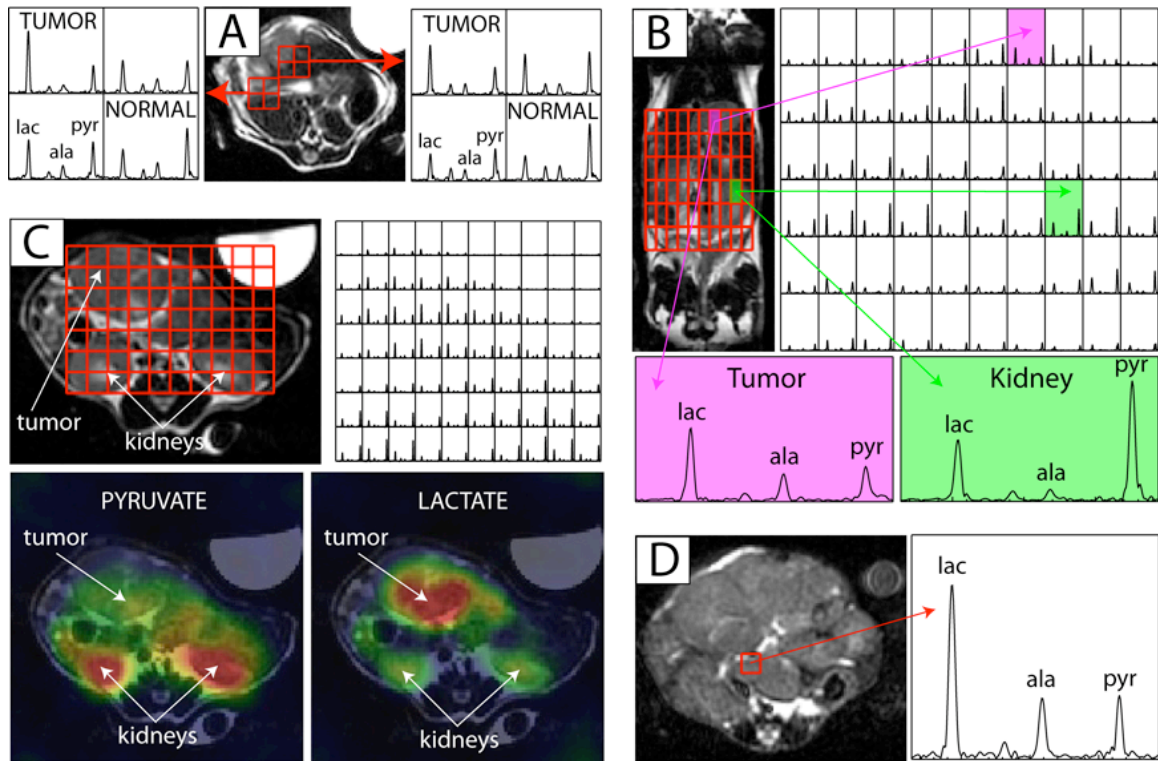


Figure 5.6: A) Spectra from a transgenic liver cancer mouse with an early stage tumor, as shown in the upper left of the anatomic image, in which acceleration was used to reduce voxel size by a factor of 4 ($\times 3.37$ acceleration, 0.034 cm^3 voxel size, 16s acquisition). Tumor voxels exhibited dramatically elevated lac/pyr ratios. The higher resolution reduced partial volume effects such that distinct metabolic profiles were observed in tumor and adjacent tissue voxels. B) A separate data set in the same mouse with the same acquisition parameters in which the 3D-MRSI data are presented coronally to emphasize the distinct metabolic profiles in tumor and other tissues. C) A 3D-MRSI data set from a different mouse with a moderate stage tumor at the level of the kidneys. Distinct differences between tumor and normal tissue are readily visualized in the color overlay maps. D) Data from a mouse with a large very late stage tumor. Elevated alanine as well as lactate was detected in the tumor mass.

Figure 5.6c shows another data set acquired from a different mouse in which a moderate stage liver tumor extended down to the level of the kidneys, once again demonstrating differences in metabolic profiles, which are easily visualized in the color overlay maps. Figure 5.6d shows a representative voxel from a third transgenic liver mouse with a very large, late stage tumor. As shown in Figure 5.6d, both lac/pyr and ala/pyr ratios were elevated in this mouse.

In summary, Figures 5.5 and 5.6 show high quality *in vivo* spectra from a total of five animals. Along with the phantom data, which matched simulations and showed high quality comparisons between accelerated and unaccelerated acquisitions, this *in vivo* data provided further evidence of the feasibility and robustness of applying compressed sensing to hyperpolarized spectroscopic imaging.

5.4 Discussion

5.4.1 Compressed Sensing

Hyperpolarized ^{13}C spectroscopic imaging has several key properties that make it an ideal application for compressed sensing, namely fundamental sparsity, high SNR, and a need for rapid imaging. Due to spin-lattice relaxation of hyperpolarized resonances to their thermal equilibrium levels, ^{13}C hyperpolarized spectroscopy is more a time-limited modality than an SNR-limited one. In this work, we devised and implemented a pulse sequence methodology to achieve up to a factor of 7.53 in acceleration for 3D spectroscopic imaging. In addition, we

performed simulation experiments to quantitatively assess the limits of acceleration and detection. This simulation and pulse sequence framework enables the straightforward design and testing of compressed sensing acquisitions with higher accelerations as desired by the user and permitted by the application. We validated our designs with both phantom and *in vivo* experiments. The data from the MYC transgenic mouse model of liver cancer provided initial preclinical evidence of the feasibility of using hyperpolarized ^{13}C technology for metabolic imaging of liver cancer. Hepatocellular carcinoma is estimated to cause a million deaths annually (76), and metastatic liver cancer is even more common. Novel targeted drug therapies are actively being developed (77), and metabolic imaging may play a significant role in assessing response to therapy. Hyperpolarized technology could become an important radiological modality for the liver because of the ability to acquire rapid metabolic images during a breath-hold.

5.4.2 Parameters for Human Studies

In the animal *in vivo* experiments presented in this work, compressed sensing acceleration was used to improve spatial resolution (to as fine as 0.034cm^3) and decrease acquisition time. In eventual clinical applications, compressed sensing could instead be used to cover a larger FOV. For example, for human liver imaging, to cover FOVs from 32cm up to 64cm with 1cm resolution, 32×32 to 64×64 phase encode matrices would be needed. The clinical scenario has several implications for compressed sensing pulse sequence design. First, there might be more sparsity to exploit with larger matrix sizes, and higher accelerations could result simply due to

more room for undersampling. To achieve higher acceleration, blips would need to jump a greater number of phase encode steps. Examining straightforward relations ($\Delta k = (\gamma/2\pi) \cdot \text{blip area} = \frac{1}{\text{FOV}}$, $\text{blip area} = \frac{1}{2} \cdot G \cdot 0.8ms$) and using the animal experiment parameters (FOV = 4cm, blip width 0.8ms, and carbon gyromagnetic ratio) indicates a gradient amplitude $G = 0.58$ gauss/cm to jump one phase encode step Δk and 1.75 gauss/cm to jump 3 phase encode steps in the x7.53 accelerated design. For the small FOVs in animal experiments, narrower blip widths could easily push the gradients close to the 4 gauss/cm limit. Fortunately, FOVs in clinical applications would be about an order of magnitude larger, so gradient amplitude constraints would not pose major design limitations. In fact, in a clinical application, the blips could be made much narrower and be used with a symmetric instead of flyback echo-planar readout. The symmetric readout would have an SNR efficiency advantage over the flyback, especially given the low gyromagnetic ratio for carbon, though the flyback readout is inherently less sensitive to many hardware imperfections (12). The minimum spatial resolution achievable in the flyback dimension with our flyback readout was 5.4mm. Higher resolution would be possible with a symmetric readout, but it would probably not be needed in a clinical setting where 1 cm³ voxel sizes would likely be appropriate. Ultimately, a practical limitation on the resolution in a clinical setting might be set by another consideration—voxel SNR, which depends on the concentration of the substrate that can be safely administered.

5.4.3 Other Accelerated Imaging Extensions and Approaches

To achieve even faster scans with our echo-planar readout, other options exist, e.g. removing the double spin-echo and coping with field inhomogeneity effects. Another avenue actively being investigated for accelerated imaging is the combination of compressed sensing with parallel imaging. Although our work focused on an echo-planar compressed sensing scheme, other detection approaches exist that may ultimately prove clinically valuable, e.g. spiral readouts (30,31). One proposed approach that would allow for very rapid acquisitions relies on a multi-echo acquisition and matrix inversion reconstruction for parametric estimation of a known set of chemical species instead of using a full spectroscopic readout (78). Radial sampling incorporating a backprojection reconstruction (HYPR) (79) represents yet another possibility, though it may be most applicable to dynamic MRSI where a composite image exists.

5.4.4 Summary

Hyperpolarized technology for the measurement of ^{13}C metabolic flux has great potential as a clinically relevant imaging tool and has several advantages, including high SNR and no background signal. Significant preclinical evidence for the usefulness of the substrate $[1-^{13}\text{C}]$ pyruvate has already been shown (14-16,54). These results are not surprising given the Warburg hypothesis and the central role of lactate in the anaerobic metabolism characteristic of many cancers (19). Hyperpolarized technology also has flexibility in terms of the pathways that can be probed, as demonstrated by ongoing efforts to polarize new compounds (59,60,70).

The sequence development in this project applying compressed sensing should be generally applicable for other hyperpolarized agent imaging studies as well.

In conclusion, in this work, a method for applying compressed sensing to hyperpolarized ^{13}C 3D spectroscopic imaging was presented and validated in simulations, phantom experiments, and *in vivo* studies, with up to a factor of 7.53 in acceleration demonstrated. In addition, ^{13}C hyperpolarized data from a transgenic model of liver cancer were collected throughout the animal at higher spatial resolution (0.034 cm^3) than previous 3D-MRSI acquisitions.

Chapter 6: *In Vivo* Assessment of Disease Progression and Regression in a MYC Transgenic Mouse Model of Liver Cancer Using Hyperpolarized ^{13}C MRSI

The following chapter is adapted from: Hu et al. *In Vivo* Assessment of Disease Progression and Regression in a MYC Transgenic Mouse Model of Liver Cancer Using Hyperpolarized ^{13}C Magnetic Resonance Spectroscopic Imaging. Submission expected 10/2009.

6.1 Background

Liver Cancer is one of the leading causes of cancer mortality worldwide. By some estimates, as many as one million deaths occur annually, making liver cancer the third most deadly cancer in the world (80,81). There is a great need for novel drug therapies, and many are currently being developed, with the most dramatic success thus far being the multikinase inhibitor sorafenib (82). At the same time, as the field of personalized medicine advances, more sophisticated imaging modalities are needed to evaluate response to therapy. At present, clinical imaging of response to therapy for solid tumors is based mainly on measurement of tumor size reduction using magnetic resonance imaging (MRI) and computed tomography (CT) (83,84). However, metabolic biomarkers could be more rapid indicators of cancer regression than tumor size (84). Studies utilizing positron emission tomography (PET) measurements of ^{18}F -fluoro-2-deoxyglucose (^{18}F -FDG) uptake have demonstrated

the ability to identify early response to therapy for breast cancer (85), non-Hodgkin's lymphoma (86), esophageal cancer (87), non-small-cell lung carcinoma (88), and ovarian cancer (89). In ^{18}F -FDG PET, FDG is actively transported across the plasma membrane, phosphorylated to FDG-6-phosphate by hexokinase (HK), and "metabolically trapped" due to the ^{18}F label preventing phosphorylation by phosphoglucose isomerase, the next enzyme in the glycolytic pathway. The ^{18}F -labeled substrate can escape if FDG-6-phosphate is dephosphorylated back to FDG by glucose-6-phosphatase (G6P), but concentrations of G6P are low in most tissues (90). Metabolic imaging, as in the case of ^{18}F -FDG PET, succeeds across a wide range of cancers because hyperglycolysis, consisting of upregulation of glycolytic transporters and kinases, serves to satisfy the bioenergetic needs of proliferating cells and appears to be a common trait among tumors (18,19). Although ^{18}F -FDG PET is an attractive clinical metabolic imaging method for detection of response to therapy for many cancers, it is not ideal for others, including prostate cancer, where FDG uptake is low (91), and brain cancer, where high FDG uptake by normal brain tissue leads to significant background interference (92). For ^{18}F -FDG PET of hepatocellular carcinoma, high false-negative detection rates have been reported, with the likely cause being a high G6P to HK ratio in the liver, leading to leakage of FDG out of cells (93,94). In fact, G6P expression occurs primarily in the liver and kidneys—the organs where the glucose-6-phosphate to glucose back reaction is needed for gluconeogenesis (90). In addition, the lengthy scan times for PET, which far exceed those for CT and breath-held MRI, can lead to respiratory motion artifacts

that compromise spatial resolution and alignment with anatomical images (95). Thus, there is a need for new rapid metabolic imaging techniques for the liver.

In addition to the upregulation of glucose transporters and glycolytic kinases, another metabolic marker of cancer is increased pyruvate to lactate conversion mediated by lactate dehydrogenase (LDH) (18,19). Lactate is one of many metabolic biomarkers being used in clinical proton magnetic resonance spectroscopic imaging (^1H -MRSI) of cancer (20,21,96); however, ^1H -MRSI has limitations, which include low sensitivity and lipid contamination. Traditional carbon magnetic resonance spectroscopic imaging (^{13}C -MRSI) suffers from even lower sensitivity, caused by a lower gyromagnetic ratio for carbon and only 1.1% natural abundance of the MR detectable ^{13}C isotope. However, recent technological developments utilizing dynamic nuclear polarization (DNP) to dramatically enhance sensitivity of metabolic substrates (on the order of 50,000-fold) have generated excitement for the prospect of rapid, high signal-to-noise ratio (SNR) assessment of ^{13}C metabolism *in vivo* (9,10). In the DNP hyperpolarization technique, a ^{13}C -enriched sample of a metabolic substrate is placed in a static magnetic field, cooled to a temperature of ~ 1.3 Kelvin, and irradiated with microwaves to build up polarization. Then the solid state sample is dissolved rapidly to room temperature using a heated solvent to produce a hyperpolarized solution ready for injection and *in vivo* metabolic imaging (9,10). $[1\text{-}^{13}\text{C}]$ pyruvate, which converts to $[1\text{-}^{13}\text{C}]$ lactate, $[1\text{-}^{13}\text{C}]$ alanine, and ^{13}C -bicarbonate *in vivo*, has been the most researched molecular imaging agent thus far, with $[1\text{-}^{13}\text{C}]$ lactate shown to be a biomarker of cancer in preclinical studies involving prostate (15,16), lymphoma (14), and brain cancer (17) animal models.

In this work, we employed a transgenic mouse model of liver cancer where the expression of MYC in liver cells can be switched on to model disease progression and switched off to cause regression in which tumor cells differentiate into normal cells (the first model to demonstrate that oncogene inactivation could uncover pluripotent differentiation) (74). In general, MYC plays a crucial role in the regulation of cell proliferation, differentiation, and apoptosis (97). MYC is overexpressed in many liver cancers and has been linked to aberrant promoter methylation (98). In addition, cluster analysis has been used to group MYC mouse models with human liver cancer subtypes, demonstrating that these models recapitulate the main pathogenetic mechanisms of the human disease (99). MYC also acts as a transcription factor for many enzymes promoting cell growth, including LDH (100). Thus, because of this direct link between MYC and LDH expression, hyperpolarized spectroscopic imaging of ^{13}C -pyruvate to ^{13}C -lactate conversion tracks the consequences of a genetic initiator of disease in this model, showing the first application of hyperpolarized technology for probing a genetic event and linking a metabolic biomarker to genotype. In addition, it demonstrates that hyperpolarized technology can be used to measure response to a “therapy” targeted at a specific gene. In summary, in this preclinical work, we investigated the use of hyperpolarized ^{13}C -MRSI to monitor metabolic changes with liver cancer progression and regression *in vivo*.

6.2 Methods

6.2.1 Mouse Tumor Model

Tet-o-MYC/LAP-tTA double transgenic mice were obtained by crossing two transgenic FVB types (74). The first type contained the human MYC gene driven by a promoter to which a Tet-transactivator (tTA) could bind. The second contained a Tet-transactivator under the control of a liver activator protein (LAP) promoter. Under this system, the Tet-transactivator drove MYC expression only in the liver. In addition, MYC expression could be inactivated by giving tetracycline, or a derivative such as doxycycline, to bind and inactivate the Tet-transactivator. The Tet-o-MYC/LAP-tTA mice were weaned on doxycycline (200 mg/kg) until 3 weeks of age, and then doxycycline was removed from the diet to induce tumor formation. All animal studies were carried out under a protocol approved by the UCSF Institutional Animal Care and Use Committee.

6.2.2 DNP and Injection of Hyperpolarized Pyruvate

An aliquot of 24 μL of $[1-^{13}\text{C}]$ pyruvic acid with 15 mM OX63 trityl radical and 1.5 mM Dotarem® gadolinium were polarized for 1 hour in a 3.35T magnetic field at 1.35 Kelvin using a Hypersense™ DNP polarizer (Oxford Instruments, Abingdon, UK). The power of the microwave irradiation was 20 mW. The solvent used to dissolve the frozen solid state sample was an aqueous mixture containing 40 mM Tris, 80 mM NaOH, and 0.3 mM Na_2EDTA . The resulting pyruvate concentration was 80 mM, with a pH ~ 7.5 , and polarizations of greater than 30% upon dissolution. A 350 μL volume of the dissolved pyruvate, followed by a 150 μL saline flush, were

injected into mice through a tail vein catheter. The uptake of ^{13}C -pyruvate and conversion to ^{13}C -lactate and ^{13}C -alanine were monitored with 3D spectroscopic imaging as described below. Mice were anesthetized with isoflurane and kept warm with a circulating-water heating pad as described previously (15,16).

6.2.3 MRI and MRSI

All experiments were performed on a General Electric EXCITE 3T (Waukesha, WI) clinical scanner equipped with 40 mT/m, 150 mT/m/ms gradients and a broadband RF amplifier. The RF coil was a custom built, dual-tuned $^1\text{H}/^{13}\text{C}$ transmit/receive design used in previous studies (15,16). T_2 -weighted proton fast spin-echo (FSE) images were acquired and used as the anatomical reference on which ^{13}C spectra were overlaid and co-registered. The axial FSE imaging parameters were: FOV = 8cm, 192x192 matrix, 2mm slice thickness, and NEX = 6. Coronal FSE imaging parameters were the same except the FOV was 10cm and slice thickness was 1.5mm. Carbon-13 hyperpolarized spectra were acquired as a volumetric grid using a compressed sensing 3D-MRSI sequence (71,101). Acquisition parameters were: variable flip angle (15,71), TE = 140ms, TR = 215ms, 16x16 in-plane phase encodes, center out phase encode order (15,71), 2.5mm x 2.5mm in-plane resolution, flyback readout in z with 16 points and 5.4mm resolution, 581 Hz spectral bandwidth, and 9.8 Hz spectral resolution. The ^{13}C 3D-MRSI scan was started 30s after injection of the hyperpolarized ^{13}C -pyruvate and lasted 16s. To quantify metabolism in the ^{13}C spectra, the areas under the ^{13}C -lactate, ^{13}C -pyruvate-hydrate, ^{13}C -alanine, and ^{13}C -pyruvate peaks (total carbon-13

defined as the sum of all four) in magnitude spectra were calculated. The ratios lactate area to total carbon area (lac/tCar) and alanine area to total carbon (ala/tCar) were computed for each voxel and then averaged over all voxels of interest for each mouse to derive the final lac/tCar and ala/tCar values for statistical analysis.

6.2.4 Liver Histology and Immunohistochemistry

Standard Histology: The excised tissues were immediately fixed in 10% neutral buffered formalin. Fixed tissue specimens were subsequently transitioned into ethanol and embedded in paraffin blocks. Tissue blocks were cut into 4-5 μm thick slices on a Leica microtome. Sections were dried onto glass slides and stained using a standard hemotoxylin and eosin (H&E) protocol.

Immunohistochemistry: Polyclonal and monoclonal antibodies against murine Ki-67 and cleaved caspase-3 were obtained from commercial vendors. Paraffin-embedded and frozen sections were cut on a microtome at 4–5 μm thickness. Paraffin sections were deparaffinized according to standard protocols. Epitope retrieval was routinely carried out by microwave heating in a 10 mM citrate buffer. Frozen sections were generally fixed with paraformaldehyde and cold acetone with 3% H_2O_2 for quenching of endogenous peroxidases. DakoCytomation Biotin Block (or similar reagent) was used as a blocking solution. Primary antibodies were incubated with specimens overnight at 4 °C; the secondary antibody was usually an anti-IgG : biotin conjugate. Washings were carried out generally for 15 min with three changes of Tris-buffered saline with 0.5% Tween 20.

Detection was performed with streptavidin:horseradish peroxidase complex, using DAB with H₂O₂ for substrates. Specimens were counterstained with hematoxylin alone.

6.2.5 LDH Expression

A one-channel microarray analysis was performed where Cy3-labeled target was hybridized to Agilent whole mouse genome 4x44K Ink-jet arrays (Agilent). LDH-A gene expression in control mice expressing the Tet-transactivator (n = 4) and mice expressing the human MYC transgene (n= 4) were compared.

6.2.6 LDH Activity

Total LDH activity was measured through an NADH-linked spectrophotometric method by observing the decrease in absorbance of NADH at 339 nm after addition of varying concentrations of pyruvate. Around 0.2 grams of frozen tissue were thawed in 830 µl of lysis buffer containing 50 mM Tris (pH 8.2), 2mM DTT, 2mM EDTA, and 1% Triton x-100. The tissue was then homogenized using a Kimble Kontes tissue grinder. After about 10 strokes with the pestle, the resulting solution was centrifuged for 1 min at 7000 rpm at 4 °C. The supernatant was then removed and diluted appropriately so that the reduction of NADH was linear over the first ten minutes of the assay. In microplate wells, 3 µl of the cell lysate were mixed with 147 µl of reaction buffer containing varying concentrations of pyruvate, 80 mM Tris (pH 7.2), 200 mM NaCl, and 200 µM NADH that was heated to 30 °C. The assay was conducted immediately by monitoring the decrease in NADH

absorbance, at 339 nm, for ten minutes using an Infinite M200 spectrophotometer (Tecan). Each pyruvate concentration was assayed in triplicates.

The reaction rate was normalized to total protein concentration, measured through the Bradford protein quantification assay (Quick Start Bradford Protein Assay from BioRad Thermo Scientific). For the Bradford assay, 5 μ l of the correct dilution of cell lysate was mixed with 250 μ l of the Bradford dye reagent. A blank was made using lysis buffer and Bradford dye reagent. The sample was assayed in triplicates, at 595 nm, after incubating at room temperature for at least 5 minutes. The absorbance of the sample was then recorded, and protein concentration was calculated using a gamma-globulin standard curve. Once the sample's protein concentration had been acquired, it was used to calculate LDH reaction rate for the varying pyruvate concentrations. The LDH reaction rate, measured in μ M NADH/min/[protein], was plotted against pyruvate concentrations according to Michaelis–Menten kinetics. The maximum velocity (V_{\max}) and K_m values were then calculated using the Lineweaver–Burk plot.

6.2.7 Statistical Analysis

All statistical analysis was performed with the JMP® software package. For the ^{13}C MRSI statistical analysis, experimental data were divided into four groups: healthy (wild type FVB mice [n = 1], Tet-transactivator control mice [n=5], and Tet-o-MYC/LAP-tTA mice with MYC on < 30 days and no tumor on anatomic imaging [n=2]), early stage disease (Tet-o-MYC/LAP-tTA mice with MYC on > 30 days and no tumor on anatomic imaging [n=4]), later stage disease (Tet-o-MYC/LAP-tTA mice

with MYC on and tumor confirmed by anatomic imaging [n = 13]), and regressed disease (Tet-o-MYC/LAP-tTA mice that had tumor, after which MYC was switched off and regression observed on anatomic imaging [n=6]). For animals where repeat acquisitions were collected, e.g. two scans in a row to investigate reproducibility, the average of the measurements was used. The healthy, early stage disease, later stage disease, and regressed disease groups were compared with Tukey's test after a one-way analysis of variance (ANOVA) was performed. For the LDH expression comparison, a student's t-test was used, and for the LDH activity correlation, the Pearson product-moment was computed, after which the student's t-test was used to test for statistical significance.

6.3 Results

6.3.1 3D-MRSI of Disease Progression

Tet-o-MYC/LAP-tTA mice were serially imaged using co-registered conventional MRI and hyperpolarized ^{13}C 3D-MRSI. The hyperpolarized spectroscopic imaging was used to monitor the uptake of pyruvate and its conversion to lactate and alanine. Several changes in metabolism were observed as mice progressed from no MRI-detectable disease to obvious disease in which large tumors were readily apparent on anatomical images. Figure 6.1a – c shows a typical set of liver spectra from one mouse that was serially followed after MYC activation. Figure 6.1d shows a liver spectrum from a separate control mouse (LAP-tTA) that had the Tet-transactivator but not the MYC transgene. Each panel in Figure 6.1 shows a representative single spectrum whose voxel location and size are indicated

by the box on the anatomical reference image, and each spectrum contains lactate at a chemical shift of 183 ppm, pyruvate-hydrate at 179 ppm, alanine at 176 ppm, and pyruvate at 171 ppm. (Note: pyruvate-hydrate, the peak between lactate and alanine, is in chemical equilibrium with pyruvate and is not metabolically active. It is not labeled in this and subsequent plots.)

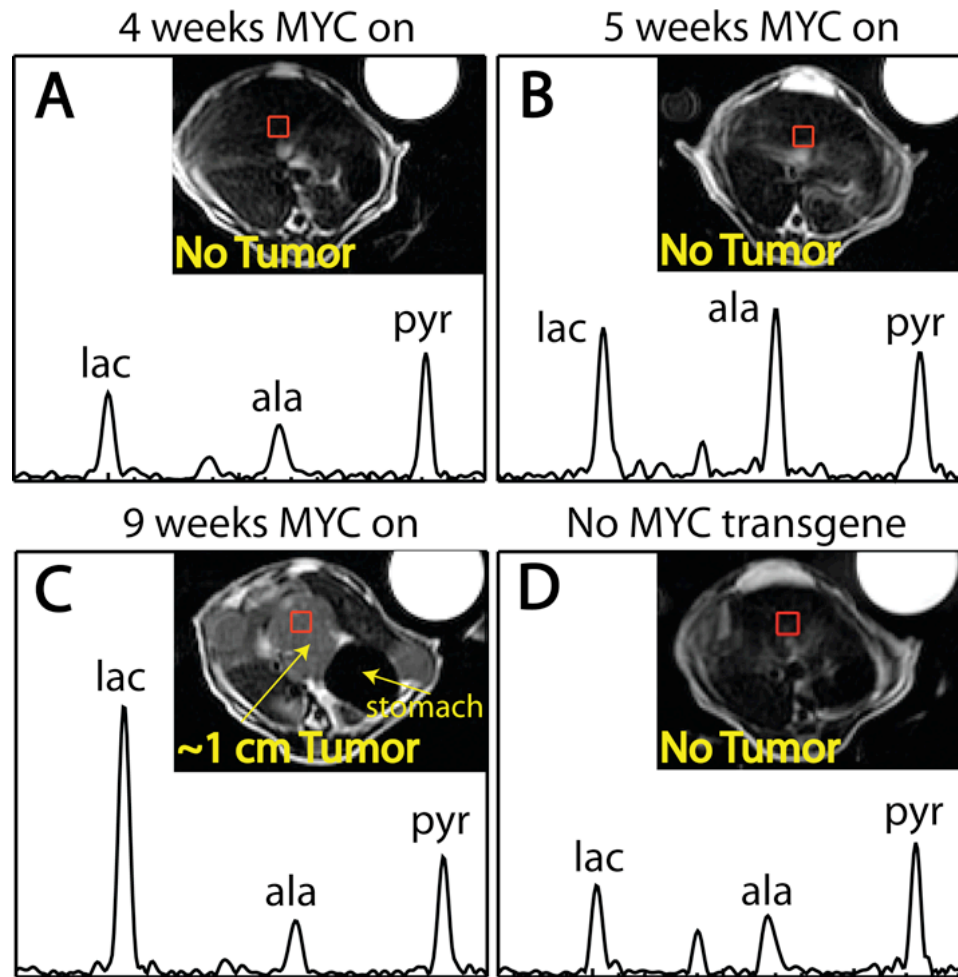


Figure 6.1: Representative set of disease progression spectra in Tet-o-MYC/LAP-tTA mice after MYC oncogene activation, with corresponding voxel locations indicated. Each spectrum was representative of the larger array of spectra collected during each spectroscopic imaging exam. Voxel size was 2.5mm x 2.5mm x 5.4mm. (A) No tumor

was detectable in the liver with anatomical imaging 4 weeks after oncogene activation, and lac/tCar and ala/tCar were low. (B) A week later in the same mouse, still no tumor was detectable on anatomical imaging, but an increase in ala/tCar was observed. (C) Eventually, a tumor was detected with anatomical imaging, and at this stage lac/tCar increased dramatically, signaling hyperglycolysis to meet the bioenergetic needs of a proliferating mass. (D) Control liver spectrum from a mouse that only expressed the Tet-transactivator and not the MYC transgene, showing low lac/tCar and ala/tCar similar to the spectrum shown in (A).

As shown in Figure 6.1c, the most dramatic change was the greatly elevated lactate found in tumor tissue. In addition, changes in alanine levels were also detected as disease progressed. As shown in Figure 6.1b, a rise in alanine was observed (compare with Figure 6.1a) before a tumor was detected on the anatomical imaging. Finally, as expected, the metabolic profile shown in the control mouse spectrum (Figure 6.1d) matched that from the MYC mouse in the healthy stage (Figure 6.1a).

Figure 6.2 highlights some of the technical capabilities of hyperpolarized ^{13}C 3D spectroscopic imaging, showing the same dataset from Figure 6.1c but demonstrating full volumetric coverage (0.034 cm^3 voxel resolution) achieved with a 16 second acquisition time. Metabolic data were acquired from the full length of the mouse, as depicted in Figure 6.2a, and axial cross sections from the tumor and kidney levels are shown in Figure 6.2b – c. Figure 6.2b shows the full spectral grid (overlaid on the anatomical reference) from which the spectrum in Figure 6.1c was selected as well as another tumor voxel spectrum enlarged to the right.

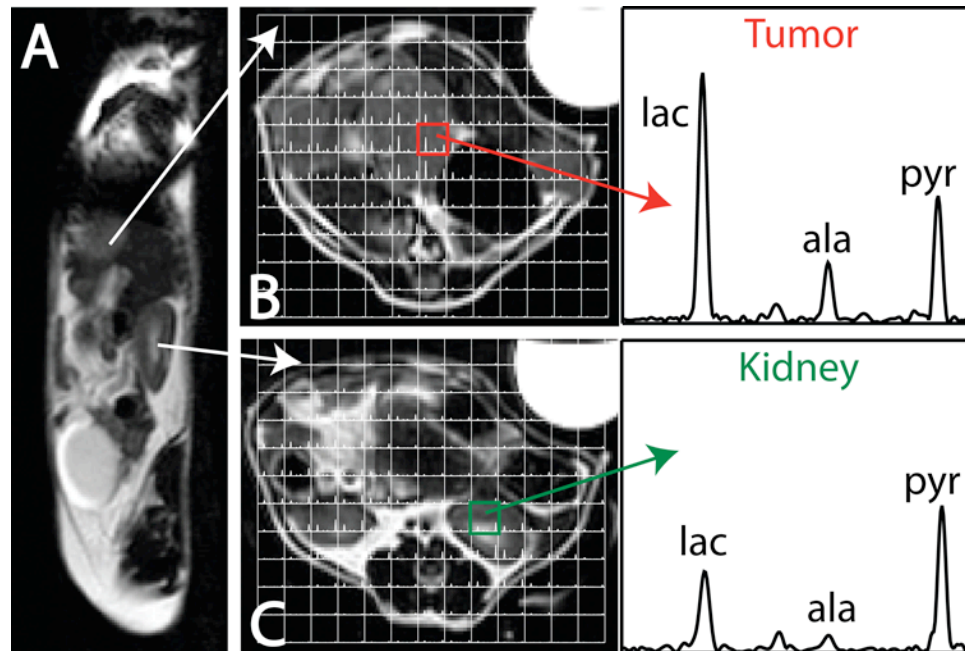


Figure 6.2: Alternate visualization of the 9 week MYC data from Figure 1, highlighting the volumetric coverage (16x16x16 matrix acquired in 16 seconds) achievable with 3D-MRSI. (A) Sagittal image showing the length across which spectra were collected. The arrows point to two specific axial cross sections at the tumor and kidney levels. (B) Set of axial spectra at the tumor level overlaid on top of the anatomical reference. High lac/tCar can be seen in multiple voxels covering the tumor, and low lac/tCar can be observed elsewhere. (C) Set of axial spectra at the kidney level overlaid on top of an anatomical reference. The kidney spectra differ dramatically from the tumor spectra, showing the metabolic heterogeneity across the entire animal. Full volumetric spectroscopic imaging has the advantage of allowing for intra-subject comparisons, e.g. among tumor, metastases, and other organs. Furthermore, spectra can be overlaid over anatomical references in any plane—axial, coronal, or sagittal.

The full volumetric acquisition ensures no anatomical locations are missed and allows for comparisons between tumor and other tissues in the same mouse. As demonstrated in Figure 6.2b – c, there were significant differences in metabolic profiles in tumor and kidney. Furthermore, because the data are acquired in 3D, spectra can be overlaid on any image plane—axial, coronal, or sagittal—if desired.

6.3.2 3D-MRSI of Disease Regression

Tet-o-MYC/LAP-tTA mice were also followed after MYC inactivation caused by using doxycycline to block the Tet-transactivator for MYC. As expected, based on previous reports using this model (74,75), MYC inactivation led to tumor regression, which was observed on both anatomical imaging and hyperpolarized ^{13}C 3D-MRSI. Figure 6.3 shows the metabolic changes associated with tumor regression, with the most dramatic change being the decrease in hyperpolarized lactate levels (Figure 6.3a – b). In the case of the mouse in Figure 6.3, changes were observed 2.5 days after MYC was inactivated. The metabolic profile 2.5 days after MYC inactivation was a healthy profile (see Figure 6.1a and 6.1d) and was similar to the profile a week after MYC inactivation when all signs of a tumor were gone. Also shown in Figure 6.3 for each panel are lactate and pyruvate color overlay maps generated from full spectral grids. The maps are a visualization tool to show the spatial distribution of the metabolites, and in the case of Figure 6.3 reiterates the decrease in lactate levels during tumor regression.

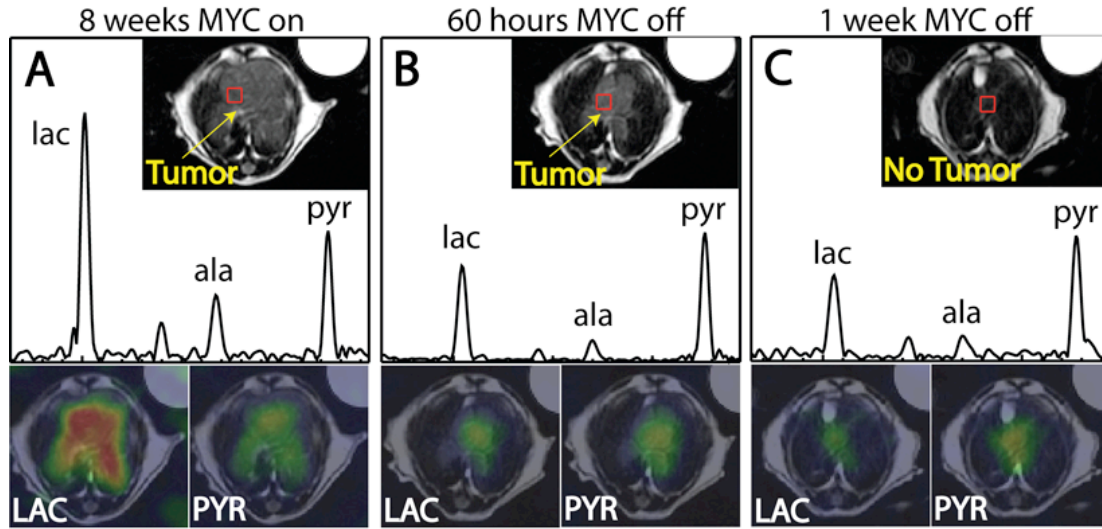


Figure 6.3: Representative set of spectra from a Tet-o-MYC/LAP-tTA mouse after doxycycline was used to block the Tet-transactivator, thereby inactivating the MYC oncogene. Each spectrum, selected from a larger array, has the corresponding voxel location highlighted. (A) High lac/tCar was observed in the baseline, pre-treatment case of a tumor after 8 weeks of MYC activation. The color overlay maps were generated from metabolite areas gathered from an axial array of spectra and serve as a visualization tool to demonstrate the spatial localization of lactate and pyruvate. The color overlay maps for (A) show high lactate across the tumor. (B) Lac/tCar dropped dramatically 60 hours after oncogene inactivation as shown by the representative spectrum as well as the color overlay maps. The metabolic profile had an appearance similar to that in Figure 6.1a and 6.1d. (C) The tumor completely regressed a week after oncogene inactivation, and the metabolic profile remained the same.

6.3.3 Progression and Regression Data over All Mice

Figure 6.4 shows the pooled hyperpolarized spectroscopic imaging data in which lac/tCar and ala/tCar for no disease, early stage disease, later stage disease, and regressed disease across every animal studied are plotted (boxes show median, minimum, maximum, and upper quartiles).

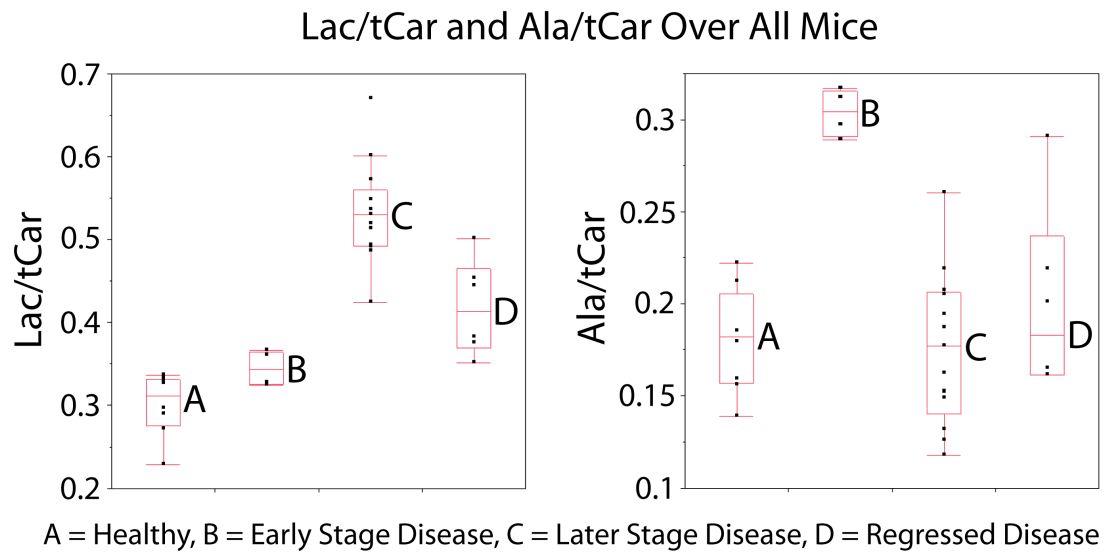


Figure 6.4: Lac/tCar and ala/tCar over all disease stages in mice examined with hyperpolarized ^{13}C 3D-MRSI. The groups A-D are healthy, early stage disease, later stage disease, and regressed disease respectively, and the plots show the minimum, maximum, and upper quartiles. As shown in the left-hand plot, lac/tCar rose dramatically as disease progressed and fell during regression, paralleling the examples shown in Figures 6.1 and 6.3. Multiple comparisons tests showed statistically significant differences ($P < 0.01$) between groups A and C, A and D, B and C, and C and D. The right-hand plot shows elevated ala/tCar in the early stage disease group ($P < 0.01$). Ala/tCar values were similar among the other groups.

Figure 6.4 recapitulates the patterns illustrated in Figures 6.1 and 6.3. In the left plot of Figure 6.4, lac/tCar is seen to rise as disease progresses and fall after regression (mean/stderr: A = 0.301 ± 0.018 , B = 0.3444 ± 0.026 , C = 0.533 ± 0.014 , D = 0.418 ± 0.021). The one-way ANOVA revealed a difference among groups ($P < 0.0001$), and the multiple comparisons showed statistically significant differences between groups A and C, A and D, B and C, and C and D ($P < 0.01$). In short, there were differences in lac/tCar among the healthy, later stage disease, and regressed disease groups. The plot on the right of Figure 6.4 shows elevated ala/tCar in the early stage disease group (means/stderr: A = 0.180 ± 0.014 , B = 0.304 ± 0.019 , C = 0.176 ± 0.011 , D = 0.200 ± 0.016). The one-way ANOVA revealed a difference among groups ($P < 0.0001$), and the multiple comparisons showed statistically significant differences between B and all other groups ($P < 0.01$). In other words, group B stood out from the rest in terms of ala/tCar.

6.3.4 Histology and Immunohistochemistry

To confirm that the morphological and metabolic changes observed with anatomical and hyperpolarized spectroscopic imaging resulted from imaging tumor versus non-tumor tissue, some mice ($n = 12$) were sacrificed for histochemical analysis. Upon dissection, nodules and masses of tumor similar to what was previously reported (74,75) were observed (lower left inset in Figure 6.5a).

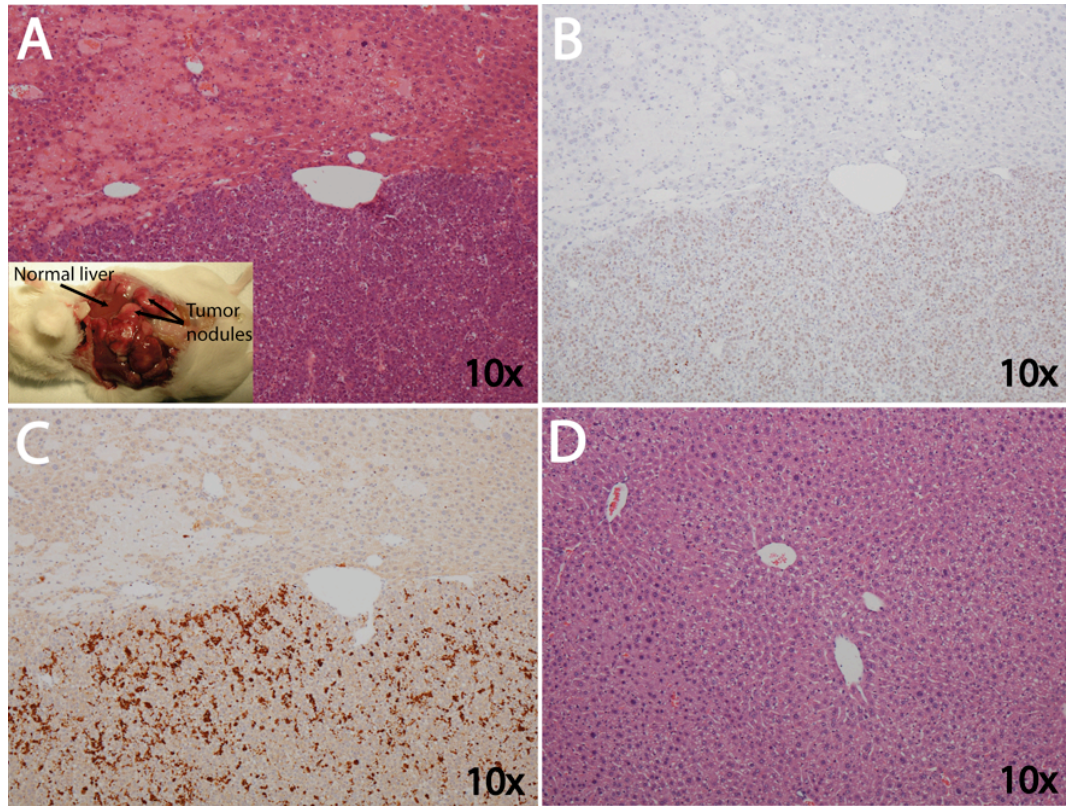


Figure 6.5: (A) H&E staining of tissue at the boundary of a tumor nodule. There was a clear demarcation between normal (upper half of image) and malignant (lower half of image) tissues, as evidenced by the higher density of darker staining and lower level of cellular organization in the tumor region. The mouse from which the sections for (A)-(C) were obtained is shown in the lower left inset, with normal liver tissue and representative tumor nodules marked by arrows. (B) The same section as (A) stained positive for Ki-67 in the tumor region, indicating a high proliferative index. (C) Accompanying the increased cell proliferation in (B) was increased apoptosis in this particular tumor example, as indicated by the positive caspase-3 staining. (D) A normal liver section from a Tet-transactivator control mouse (no MYC transgene) showed a low density of darker staining and a high level of cell organization, similar to the healthy regions in (A).

Figure 6.5a – c shows H&E, Ki-67, and caspase-3 stained sections from the edge of a representative tumor mass taken from the mouse shown in the lower left of Figure 6.5a. As shown in the H&E stained section in Figure 6.5a, there was a clear demarcation of the grossly normal side of the sample (upper half of Figure 6.5a) and the tumor mass (lower half of Figure 6.5a). The tumor side showed a much higher density of darker staining and a much lower level of cell organization than the healthy patches in the upper half of the section. Figure 6.5d shows a Tet-transactivator control liver H&E stained section for comparison. In addition, as shown by the Ki-67 stain (Figure 6.5b) of the same section as Figure 6.5a, the tumor tissue had a higher proliferative index than surrounding tissue. In the case of this tumor mass, but not in all tumor tissue analyzed, the heightened proliferative state was also accompanied by a higher rate of apoptosis than in surrounding tissue (Figure 6.5c). Overall, the histochemical analysis agreed with prior work with the same animal model (74,75) and verified that the differences observed with imaging resulted from examining different tissue types.

6.3.5 LDH Expression and Activity

In order to investigate further the elevated hyperpolarized lactate levels observed in cancer tissue, LDH expression and activity assays were performed. Tumor tissue from Tet-o-MYC/LAP-tTA mice and normal liver samples from Tet-transactivator control mice (n = 4 for each group) were used for the LDH expression comparison. As shown by Figure 6.6a, which shows the means and standard errors for the two groups, there was a significant difference in levels of expression ($P <$

0.002). The expected consequence of increased LDH expression would be increased levels of the LDH enzyme, leading to higher LDH activity and higher levels of hyperpolarized lactate.

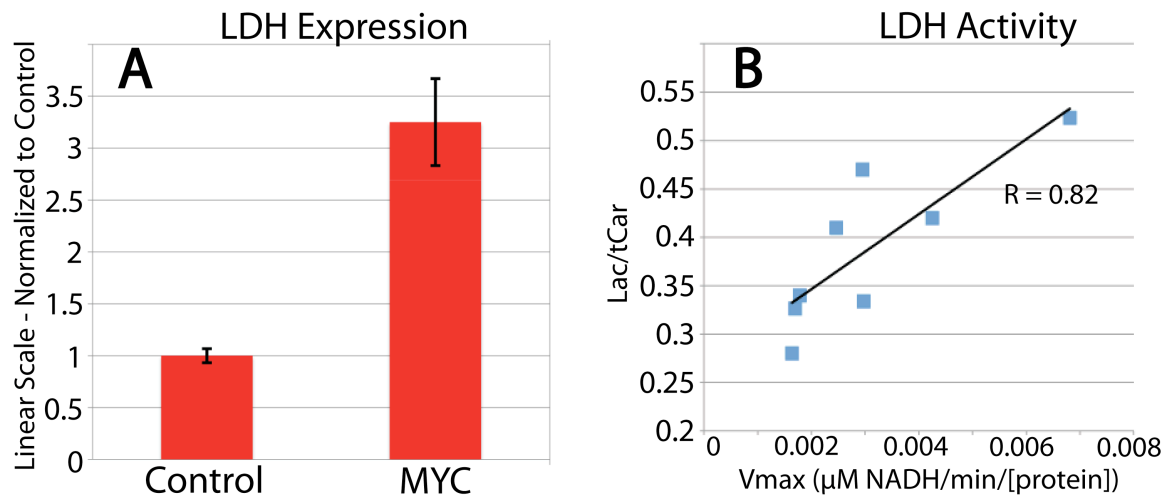


Figure 6.6: LDH expression and activity assays. (A) Microarray analysis was used to compare LDH-A expression between Tet-o-MYC/LAP-tTA and Tet-transactivator control mice ($n = 4$ for each group). Higher expression was found for the MYC group ($P < 0.002$, means and standard errors shown). (B) Regression analysis of lac/tCar and LDH activity (V_{max}). For mice that were dissected close to their last hyperpolarized exam, LDH activity assays were performed on normal and tumor liver tissues and compared with their lac/tCar values averaged over regions of interest identified from anatomical imaging. A statistically significant correlation ($r = 0.82$, $P < 0.02$, one outlier excluded) was observed.

Also LDH activity from extracted tissue was correlated with corresponding hyperpolarized lac/tCar measurements in those tissues before extraction. Figure

6.6b shows a Pearson product-moment $r = 0.82$ with $n = 6$. An outlier ($V_{\max} = 0.0029$, $\text{lac}/\text{tCar} = 0.62$) was excluded, and the significance of the correlation was $P < 0.02$.

6.4 Discussion

6.4.1 Advantages of Hyperpolarized Technology

In this report, we demonstrated a technique for rapid, non-invasive metabolic imaging of liver cancer, and we showed preclinical results for monitoring progression and regression in a MYC-oncogene driven transgenic animal model. Hyperpolarized ^{13}C spectroscopic imaging has many strengths that complement existing radiologic modalities. One advantage for liver applications is the ability to do very rapid, i.e. breath-held, metabolic imaging. Another advantage is the capability to examine glycolytic metabolism beyond uptake and the first enzymatic step, which has limitations in PET of the liver (93,94). Additionally, hyperpolarized imaging with pyruvate has advantages in terms of safety because of the use of a non-ionizing, endogenous compound in which the ^{13}C label is also naturally occurring and not much heavier than the more prevalent ^{12}C isotope (i.e. no heavy isotope effects as in the case of deuterium). Further advantages include very high SNR, which has been the traditional limitation in ^{13}C -labeled studies (50,52), virtually no background ^{13}C signal, allowing for high signal contrast, and large chemical shift dispersion, resulting in clear peak separation and simple post-processing. The major technical disadvantage is the rapid decay of the hyperpolarized signal, which necessitates fast acquisition strategies like those used in this project. The

abovementioned advantages and promising preclinical results in prostate cancer animal studies (15,16), have prompted the first human studies to be scheduled for prostate cancer patients with the hope of more studies to follow.

6.4.2 Biomarkers

In this current preclinical liver cancer work, we observed dramatic and statistically significant changes in the lactate and alanine biomarkers. The histology verified that these changes came from regions of cancerous tissue, with the H&E staining showing clear differences between malignant and normal tissues. In addition, cancer tissue stained positive for Ki-67, which corroborated previous work (74) and was not surprising given the key role MYC plays in cell cycle control and proliferation (97). Table 6.1 below lists histological and immunohistochemical data from all animals where tissue was collected.

Table 6.1: Histology and Immunohistochemistry from All Collected Samples
H&E, Ki-67, and caspase-3 staining results across all mice from which tissue were collected. Mice were either sacrificed or died from tumor burden and/or anesthesia complications related to tumor burden. The status of the MYC transgene (ON/OFF) is also given. All tumors stained positive for Ki-67, while the caspase-3 results were variable.

Mouse ID	MYC Transgene	H&E	Ki-67	Caspase-3
MSL1	ON 9 weeks	Mostly tumor	Positive in tumor	Positive in tumor

MSL2	ON 9 weeks	Mostly tumor	Positive in tumor	Positive in tumor
MSN2	None, wild type	Normal	NA	NA
MSN3	None, wild type	Normal	NA	NA
MSL4	ON > 10 weeks	Mostly tumor	Positive in tumor	Negative
MSL7	ON, then OFF, then back ON 7 weeks	Tumor with some necrosis	NA	NA
MSL8	ON, then OFF 2 days	Tumor and normal	Positive in tumor	Positive in tumor
MSL9	ON, then OFF 5 days	Mostly normal	Negative	Negative
MSL11	None, Tet-transactivator control	Normal	Negative	Negative
MSL16	ON, then OFF, then back ON 5 weeks	Mostly tumor with some necrosis and normal	Positive in tumor	Positive in tumor
MSL17	ON > 10 weeks	Tumor and normal	Positive in tumor	Negative
MSL19	ON, then OFF 8 days	Tumor and normal	Negative	Negative

The high levels of hyperpolarized lactate, the main finding in this work, matched previous observations in prostate cancer (15,16), lymphoma (14), and brain cancer (17) animal models, attesting to the ubiquity of increased glycolysis in cancer (18,19) and the importance of the lactate biomarker (20,21,96). Day et al. proposed that a high hyperpolarized lactate signal is at least in part due to a label exchange phenomenon in which LDH rapidly transfers the ^{13}C label from pyruvate to pre-existing lactate (14), with increased pre-existing lactate arising from increased LDH expression and activity. Our LDH assay data, showing higher expression in MYC mice, are compatible with this assertion. In addition, the high Pearson product-moment ($r = 0.82$, $P < 0.02$) in the activity measurements indicates a correlation between LDH activity and hyperpolarized lac/tCar. Overall, the data do not refute the working theory of the involvement of LDH in hyperpolarized lactate levels. In fact, the high lactate makes even more sense in our animal model because MYC is a transcription factor for LDH (100). In this instance where we are imaging a result of LDH expression, which is directly downstream of MYC, we are in effect imaging genotype. This is the first demonstration that a switchable genetic event can be correlated with hyperpolarized imaging and the first instance of detecting response after targeted inhibition of an oncogene.

Hyperpolarized alanine, which has been shown to be an indicator of metabolism in fasted rat liver studies (102), was the other biomarker of interest, but no correlations were found between hyperpolarized alanine levels and activity of ALT. However, only later stage disease mice were available for the activity assays while the highest ala/tCar ratios were observed in early stage disease mice. Alanine

was a biomarker of interest before the hyperpolarized studies were conducted because blood tests for elevated ALT levels are routinely used to detect possible liver disease, including hepatitis and fatty liver disease, with the presumed mechanism being leakage of ALT from damaged liver cells (62). A consequence of ALT leakage might be increased hyperpolarized alanine conversion happening outside of the cells. To investigate this idea, uptake inhibitor studies were performed to measure alanine levels when pyruvate transport was inhibited. In order to inhibit pyruvate transport into cells, the MCT inhibitor α -cyano-4-hydroxycinnamate (4-CIN) was used. Hyperpolarized 3D-MRSI (with the same parameters as for the progression/regression experiments) was performed twice—once to establish a baseline and then again 30 minutes after an intraperitoneal injection of 90 mg/kg of 4-CIN (dissolved in a pH 7.5 phosphate buffer). The results are shown in Figure 6.7 and Table 2 below. As shown by the data above, ala/tCar dropped after 4-CIN administration, suggesting that hyperpolarized alanine conversion occurs intracellularly, i.e. after uptake of pyruvate. However, the MCT inhibitor was probably not completely effective, as shown by the high amounts of hyperpolarized lactate. Another caveat is that 4-CIN also blocks lactate transport out of cells, thus preventing lactate from being cleared, which might explain the increases in lac/tCar in Table 6.2.

In view of all the assay experimental results, it is important to acknowledge that efforts to explain the precise mechanism for observations of hyperpolarized biomarker levels are ongoing, but nonetheless, valid and statistically significant biomarkers were found that warrant future investigation in animal and human studies.

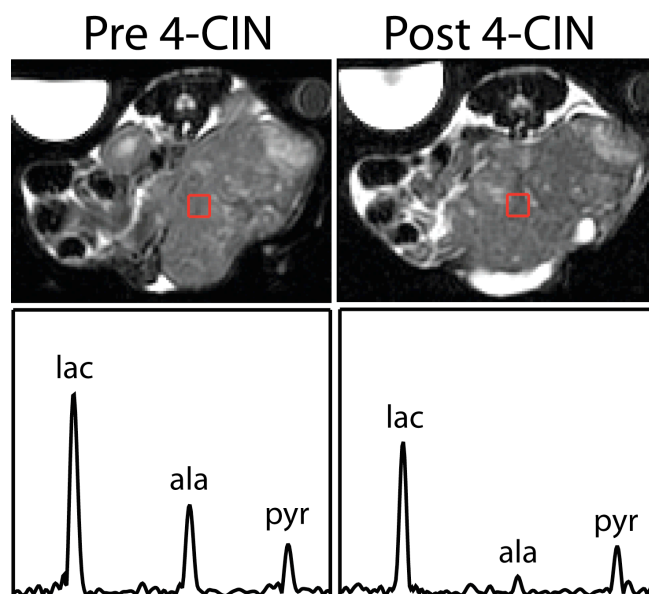


Figure 6.7: Effect of MCT inhibitor 4-CIN on hyperpolarized spectra from a tumor region. In this example, lactate levels dropped slightly, but alanine levels dropped dramatically after 4-CIN administration.

Table 6.2: Pyruvate Uptake Inhibition Results from Several Mice

Quantitation over all tumor (for MYC) and liver (for normal) voxels for mice ($n = 3$) in which MCT inhibition experiments were performed. Note: Pyr/tCar includes pyruvate and pyruvate-hydrate. As shown by the data below, in all cases, ala/tCar decreased after 4-CIN administration.

Mouse ID	Mouse Details	4-CIN Status	Lac/tCar	Ala/tCar	Pyr/tCar
MSL27	MYC, large tumor	Pre	0.67	0.12	0.21
		Post 30 min	0.77	0.09	0.14

MSL28	MYC, large tumor	Pre	0.63	0.21	0.16
		Post 30 min	0.67	0.08	0.25
MSL14	Tet-transactivator, normal	Pre	0.32	0.17	0.51
		Post 30 min	0.22	0.06	0.72

6.4.3 Future Work and Prospects

The MRSI techniques used in this work would most likely need optimization and improvement to meet the imaging requirements for the ultimate clinical application. To cover a human liver with a field of view of 36cm x 28cm and 1 cm³ resolution in the same time as the mouse acquisitions, the scans would need to be accelerated by an additional factor of 4, possibly by incorporating parallel imaging with compressed sensing. Alternatively, the acquisition (breath-hold time) could be lengthened by a factor of 4. Other future work includes further preclinical studies with the Tet-o-MYC/LAP-tTA mice. Transgenic models have advantages over xenograft models for recapitulating the natural course of hepatocarcinogenesis in general (103) and in particular with regard to heterotypic interactions and neovascularization of nascent tumors. Furthermore, this inducible model is ideal for response to treatment studies because of the ability to control the time of oncogene activation. With the effectiveness of hyperpolarized imaging in evaluating the response to the control therapy, i.e. oncogene inactivation, established by this study,

future studies can investigate imaging of response to novel targeted drug therapies (75).

There exists great clinical potential for ^{13}C hyperpolarized technology. First of all, hyperpolarized spectroscopy is an inherently rapid metabolic imaging modality, something needed for the liver. There has been a trend toward combining metabolic assessments with powerful anatomical imaging modalities, such as the established PET/CT and the more recent and developmental PET/MRI. Hyperpolarized technology offers the capability of delivering metabolic assessments and anatomical imaging in a completely MR based system. Furthermore, hyperpolarized ^{13}C spectroscopic imaging with $[1-^{13}\text{C}]$ pyruvate has advantages over ^{18}F -FDG PET for tumor imaging in organs where ^{18}F -FDG uptake is too low (prostate (91)), too high (brain (92)), or where glucose-6-phosphatase is present (liver (93,94)). Measurement of glycolysis in general, and specifically with pyruvate, is a powerful approach because if hyperglycolysis is a prerequisite for proliferation (18,19), then its reduction can be considered an early indicator of response. In this study, the reduction of metabolic activity coincided with a reduction in tumor size, but this could be associated with animal models in general where tumors occupy a disproportionately large space relative to the entire body. In prior studies with PET, a reduction in glycolytic metabolism was shown to be an indicator of response before reduction of tumor size (85-89). Beyond the glycolytic readout with pyruvate, many other possibilities exist with hyperpolarized technology. For example, polarizing ^{13}C -bicarbonate and measuring conversion to $^{13}\text{CO}_2$ gives a readout of pH (60), which is powerful in that many diseases, including cancer,

exhibit abnormal pH (61). Polarizing [5-¹³C]glutamine and examining conversion to [5-¹³C]glutamate also has possibilities for assessing proliferation (70).

Hyperpolarized ¹³C-urea has been used as a perfusion mapping agent (22). And recent early stage work has explored hyperpolarized fumarate as an indicator of necrosis (104) and hyperpolarized fructose as an uptake/single enzymatic step readout similar to ¹⁸F-FDG (105). Furthermore, there has been work to polarize more than one agent at the same time in order to create a single shot metabolic readout of multiple physiologic parameters, e.g. pyruvate with bicarbonate for simultaneous spatially localized assessment of glycolysis and pH.

In conclusion, we have shown the ability to monitor disease progression and regression in a switchable transgenic mouse model of liver cancer. This model appears to be a good platform for further preclinical imaging studies of liver cancer and response to targeted drug therapy. We have reported a new preclinical application of an emerging radiologic technology, thus laying the groundwork for eventual patient studies and the introduction of a clinical imaging tool for rapid metabolic assessment of liver cancer.

Chapter 7: Application of HSn Low Peak B₁ Adiabatic Refocusing Pulses to Hyperpolarized ¹³C Spectroscopic Imaging

7.1 Background

As mentioned in Chapter 2, adiabatic refocusing pulses were used in the animal hyperpolarized imaging studies. Adiabatic pulses are well known to be insensitive to B₁ inhomogeneities (4,106,107). In other words, variations in RF amplitude do not affect adiabatic pulses as much as they do other pulses. For non-adiabatic pulses, flip angle is determined by B₁ amplitude according to:

$$\theta = \gamma \int_0^T B_1(t) dt \quad [7.1]$$

Eqn. [7.1] indicates that flip angle is linearly proportional to B₁, meaning a 10% error in B₁ results in a 10% error in flip angle. However, for adiabatic pulses, if certain conditions are satisfied, flip angle does not change as B₁ varies since it depends on a frequency sweep (4,106,107). In this dissertation, a pair of adiabatic refocusing pulses was used to acquire full spin-echo data. The advantages of acquiring full spin-echo data are: insensitivity to T₂* effects (transverse relaxation not intrinsic to the molecule studied, e.g. due to B₀ inhomogeneity), higher signal from collecting both halves of *k*-space, and easier data processing due to the full echo magnitude spectra linewidth being the same as that from half echo phased spectra (11). Non-adiabatic pulses could also be used to acquire full spin-echo data,

but the insensitivity of adiabatic pulses to B_1 imperfections is a key advantage, especially for hyperpolarized applications where irretrievable loss of the hyperpolarized signal due to inaccurate flip angles would be unacceptable. The disadvantage of acquiring full spin-echo data is that echo time (delay until signal acquisition) increases, meaning more T_2 relaxation of the signal occurs. Fortunately, the ^{13}C T_2 values for pyruvate, lactate, and alanine are relatively long; thus, the longer echo time has a minimal effect on signal strength (13). For the adiabatic refocusing pulses, the most common pulse shape, the hyperbolic secant (HS), was used. However, these pulses require a relatively high peak B_1 amplitude (106), which is achievable for small animal coils, but not using human sized clinical coils. Specifically, the adiabatic refocusing pulses that were used had a nominal peak B_1 of 1.7 gauss, and the achievable peak B_1 on the clinical coil/amplifier combination planned for the first human hyperpolarized studies is approximately 0.5 gauss. To accommodate this design constraint, we implemented stretched hyperbolic secant (HSn) pulses, which have much lower peak B_1 (106).

7.2 Methods

7.2.1 Pulse Design and Validation

The specific pulse forms used for the HSn pulse envelope and instantaneous frequency, which have been described previously (108), were:

$$B_1(\tau) = (B_{1,\text{max}}) * \text{sech}(\beta\tau^n) \quad [7.2]$$

and

$$\omega(\tau) = AB \int_0^{\tau} \text{sech}^2(\beta(\tau')^n) d\tau' \quad [7.3]$$

where τ is the normalized time scale $[-1,1]$, $B_1 \text{max}$ is the nominal peak B_1 in gauss, n

is the stretch factor, $A = -\mu\beta$, and $B = \left[\int_0^1 \text{sech}^2(\beta\tau^n) d\tau \right]^{-1}$. This form reduces to a

standard hyperbolic secant for $n = 1$. A pulse designed to have a nominal B_1 of 0.4 gauss is shown in Figure 7.1.

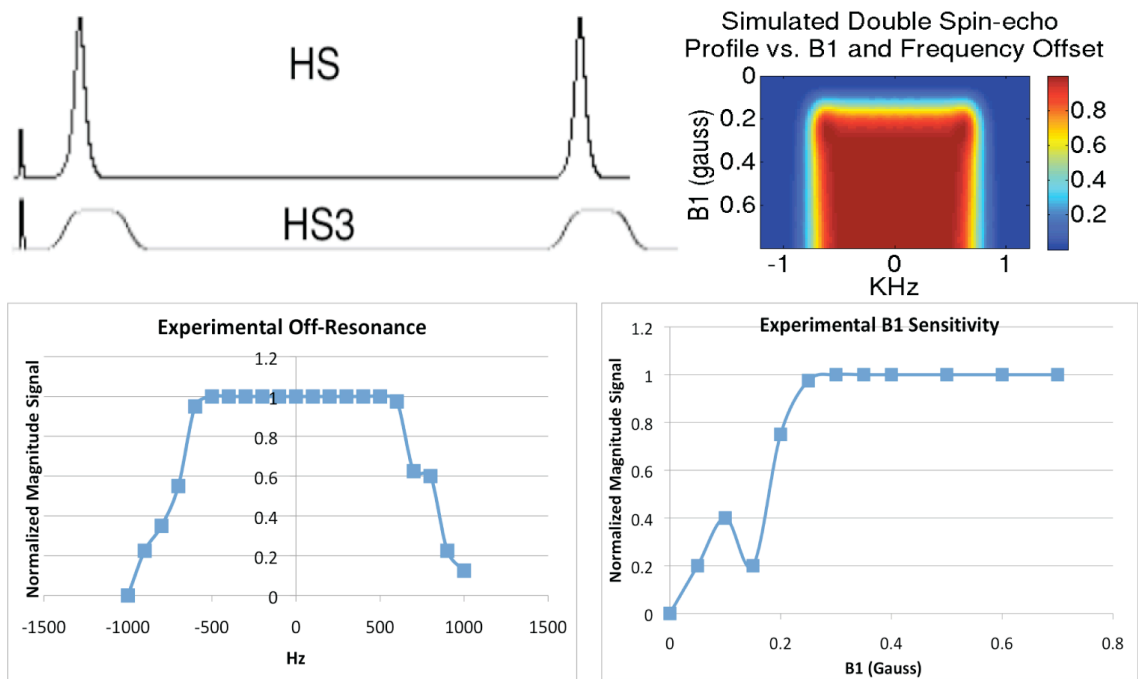


Figure 7.1: The top left shows the double spin-echo RF sequence (90-180-180) with the 1.7 gauss HS and 0.4 gauss HS3 pulses. Only the envelopes of the 180s are shown. The 0.4 gauss peak B_1 HS3 pulse has a duration of 15 ms. The top right shows the simulated off-resonance/ B_1 sensitivity map. The profile is uniform over a bandwidth of about 1 KHz and a B_1 down to about 0.25 gauss. The bottom left shows the experimental off-

resonance profile at 0.4 gauss. The bandwidth was about 1 KHz, matching simulations. The bottom right shows the experimental B_1 sensitivity profile on resonance, with the profile being uniform down to about 0.25 gauss, again matching simulations.

The design parameters were: $n = 3$ (HS3), $\mu = 8$, $\beta = 4.725$, and pulse length = 15 ms. As shown by the comparison with the standard HS pulses, the HS3 pulses have a stretched appearance and a much lower peak B_1 . Off-resonance and B_1 sensitivity simulations were performed with a Bloch simulator. As shown in Figure 7.1, the simulated profile was flat and equal to unity over a bandwidth of -500 Hz to 500 Hz and a B_1 down to about 0.25 gauss. Similar performance was observed for phantom experimental measurements of bandwidth and B_1 sensitivity at 3T, which are also shown in Figure 7.1 (done by measuring the signal from a syringe containing a single ^{13}C metabolite and varying the center frequency and B_1 amplitude manually).

7.2.2 C-13 Phantom and *In Vivo* Validation with Animal Coils

All experiments were performed on a General Electric EXCITE 3T (Waukesha, WI) MR scanner equipped with 40 mT/m, 150 mT/m/ms gradients and a broadband RF amplifier. A carbon-13 phantom containing pyruvate, lactate, and alanine spheres (as in previous studies) was used for the first set of experiments comparing the performance of the new HS3 pulses to the standard HS pulses. The double spin-echo sequence used throughout this dissertation was run with the following acquisition parameters: 10 degree flip angle, centric phase encoding order, TE = 140ms when HS pulses were used, TE = 150ms when HS3 pulses were

used, TR = 2s, in-plane FOV = 8x8 cm, and 1 cm³ isotropic voxel resolution. Performance comparison experiments were also performed *in vivo* on healthy mice. Those acquisition parameters were: variable flip angle, centric phase encoding order, TE/TR = 140/215 ms when HS pulses were used, TE/TR = 150/225 ms when HS3 pulses were used, in-plane FOV = 4x4 cm, and 5mm x 5mm x 5.4mm x/y/z voxel resolution. For the *in vivo* experiments, ~20% liquid state polarization of [l-¹³C]pyruvate (with 0.5 mM gadolinium) was achieved. ~350μL of pyruvate (~80 mM) were injected over 12 seconds followed by a saline flush, with acquisitions starting 35 seconds from the start of injection. Custom built, dual-tuned ¹H/¹³C transmit/receive coils were used for all spherical phantom and animal experiments.

7.2.3 Validation with Clinical Coil/Amplifier Configuration

The HS3 pulses were also tested with the coil/amplifier configuration to be used for human prostate hyperpolarized studies. As shown in Figure 7.2, this configuration included an endorectal coil for ¹³C and ¹H reception, a ¹H receive array, and a ¹³C transmit coil (¹H transmit done with the body coil). The ¹³C RF amplifier had a maximum transmit power of 8 kW, and all experiments were performed on a volunteer with the endorectal coil inserted. Embedded within the endorectal coil was a urea external standard used to test ¹³C received signal strength. The acquisition parameters were: TE = 125ms, TR = 1s, and 7mm x 7mm x 7mm voxel resolution.

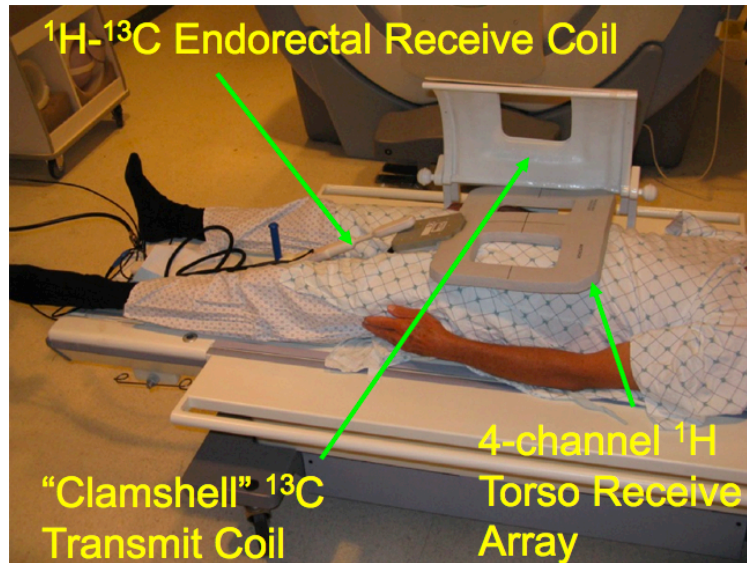


Figure 7.2: Human coil configuration for prostate cancer MR studies. An insertable endorectal coil is used for ^{13}C signal reception, and a specialized clamshell coil is used for excitation.

7.3 Results

7.3.1 C-13 Phantom

Figure 7.3 shows a 3D-MRSI phantom comparison between 1.7 gauss and 0.4 gauss acquisitions. The top part of Figure 7.3 shows a single slice comparison, and the bottom part of Figure 7.3 shows spectra summed over all signal-containing voxels. There was nearly perfect agreement between the two acquisitions.

7.3.2 Mouse

Figure 7.4 shows an *in vivo* comparison between 1.7 gauss and 0.4 gauss acquisitions. Once again, there was equally good spectral quality in the 0.4 gauss acquisition.

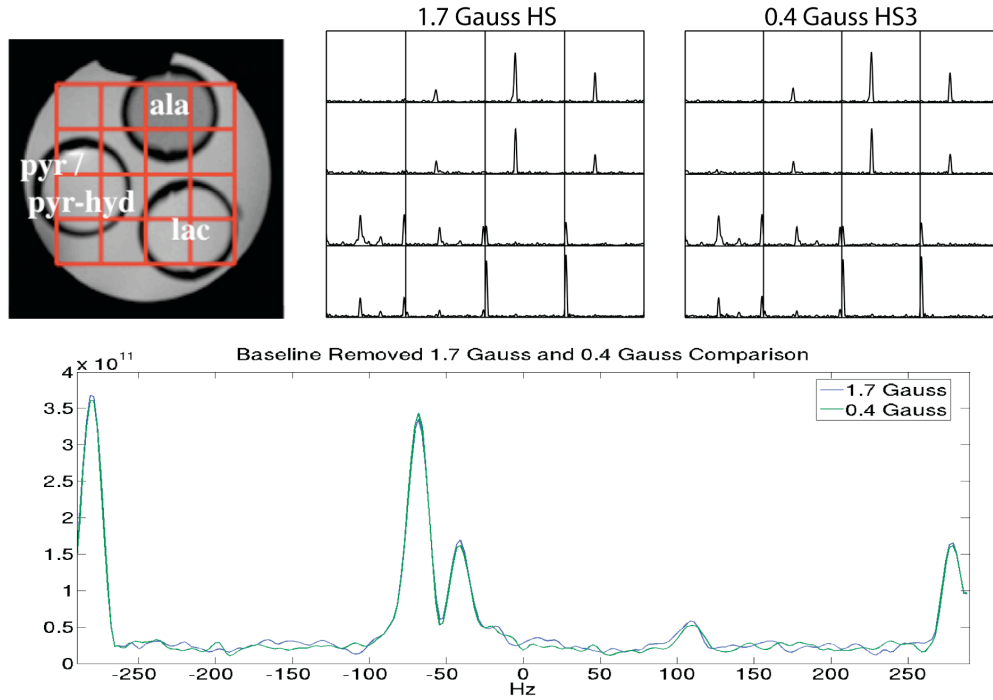


Figure 7.3: Phantom comparison between acquisitions with 1.7 gauss and 0.4 gauss pulses, showing close agreement between the two experiments. The top shows spectra from a single slice, and the bottom shows summed spectra over all voxels containing signal.

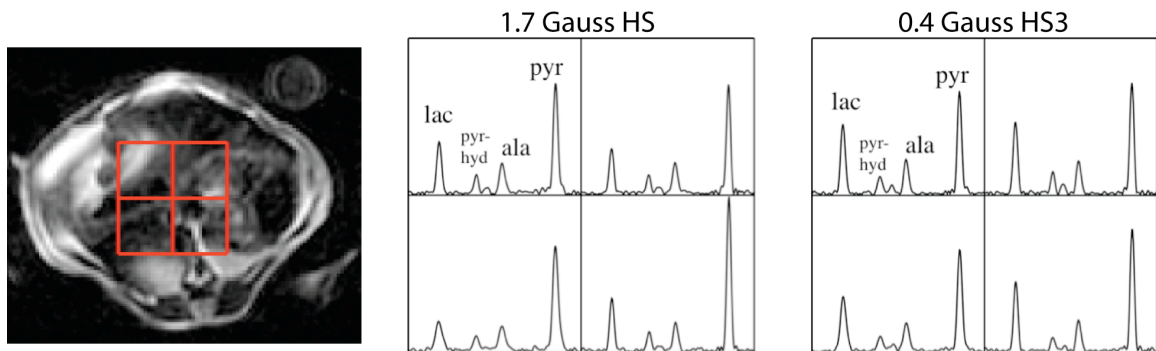


Figure 7.4: In vivo spectra from a normal mouse showing good spectral quality in both 1.7 gauss and 0.4 gauss acquisitions.

7.3.3 Volunteer

Figure 7.5 shows data from an acquisition using the prostate clinical setup of a clamshell ^{13}C transmit coil (capable of ~ 0.5 gauss with proper loading) and an endorectal receive coil. The voxels from the urea external standard in the endorectal coil were accurately localized, demonstrating little patient movement between the anatomical and spectroscopic acquisitions. Figure 7.5 shows the feasibility of a full spin-echo 3D-MRSI acquisition with the 0.4 gauss HS3 pulses under the realistic conditions of proper loading and using an insertable endorectal receive coil with a specialized ^{13}C transmit coil. Of course, it was not possible to compare the performance with the 1.7 gauss HS pulses because the high peak B_1 required by those pulses were not achievable with this coil setup.

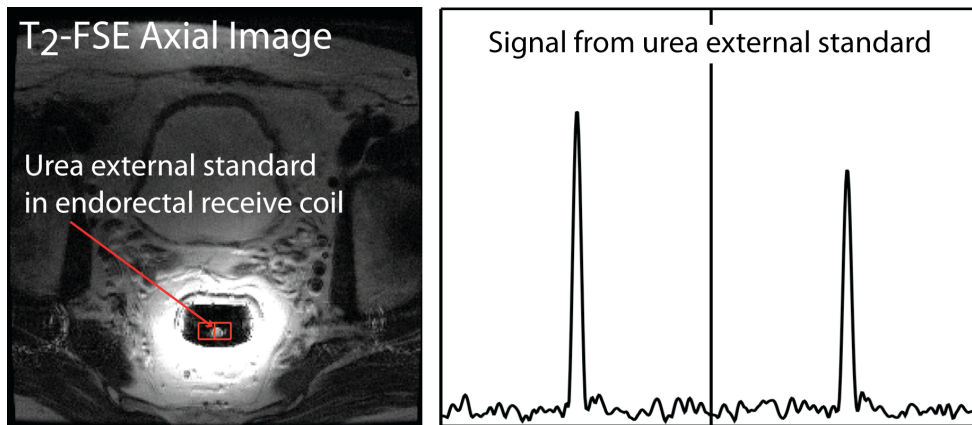


Figure 7.5: Feasibility data showing good localization and signal strength from a urea external standard embedded in an endorectal receive coil. The coil was inserted into a volunteer, and a specialized ^{13}C transmit coil was used.

7.4 Discussion

The simulation, phantom, and *in vivo* data suggest that the 0.4 gauss HS3 pulses performed as well as the previously reported 1.7 gauss HS pulses. Although the 1.7 gauss pulses do have a higher bandwidth (11), the new pulses' bandwidth is sufficient to cover pyruvate and its products, including bicarbonate but not CO₂. In general, the primary disadvantage of a spin-echo acquisition is signal loss for short T₂ species, but fortunately, the T₂s of pyruvate, lactate, and alanine are relatively long (13). In addition, a full echo requires a longer TR, but most of that extra time is used collecting data from the additional first half of the echo. For the human setup, we acquired data from reference samples and verified that sufficient B₁ could be attained and that the pulses worked with the hardware. Although the human studies have not started, with the newly designed HS_n pulses, spin-echo acquisitions as done in animal experiments are now an option.

Chapter 8: Summary

The topic of this dissertation was hyperpolarized ^{13}C MRSI, a new area of research in magnetic resonance imaging. This research involved both the technical development of new MR methods and their application to biologic research in preclinical liver studies. Chapter 3 focused on an initial design of a pulse sequence to adapt compressed sensing rapid imaging for hyperpolarized ^{13}C MRSI. Since hyperpolarized signals rapidly decay to their thermal equilibrium values, rapid imaging techniques are extremely beneficial. Compressed sensing is an excellent technique for hyperpolarized applications because hyperpolarized signals are inherently sparse and high in SNR. Chapter 4 presented the application of hyperpolarized MRS/MRSI to the study of liver metabolism, demonstrating that a change could be detected during the physiological perturbation of fasting. Chapter 5 advanced the compressed sensing methodology presented in Chapter 3 with designs for higher accelerations as well as systematic simulations for investigating the effects of noise and the limits of undersampling. The research presented in Chapter 6 demonstrated that metabolic changes were also detected during liver disease, specifically cancer. Finally, Chapter 7 presented a pulse sequence modification useful for human studies to facilitate clinical applications of hyperpolarized technology.

Hyperpolarized ^{13}C MRS/MRSI with $[1-^{13}\text{C}]$ pyruvate has the ability to detect metabolic changes associated with cancer and other disease states. An obvious future direction is to use $[1-^{13}\text{C}]$ pyruvate for MRS/MRSI in humans. Initial prostate

cancer studies are planned to start at UCSF in the near future, and their success would no doubt trigger clinical studies of various other diseases as well as development and optimization of new pulse sequences and hardware. As discussed before, ^{13}C technology has many advantages, including use of endogenous compounds as agents, no background signal interference, and the capability to do rapid, high SNR metabolic imaging. In addition, although this dissertation focused on $[1-^{13}\text{C}]$ pyruvate, other agents, as mentioned in a few of the chapters, have great potential as well and could benefit from the bioengineering developments accomplished through this research. For example, hyperpolarized bicarbonate for pH mapping could have a significant medical impact and the acceleration provided by compressed sensing methods could improve the speed, resolution and/or spatial coverage. Hyperpolarized carbon-13 is a flexible technology, and developing new hyperpolarized agents and applications will almost certainly be a major research focus in the future.

In conclusion, hyperpolarized carbon-13 is a rich, emerging research area with great clinical potential. Already, several groups worldwide have created a small but significant body of technical and preclinical research, to which the work presented in this dissertation contributes.

References

1. Levitt MH. Spin dynamics: basics of nuclear magnetic resonance. West Sussex, England: John Wiley & Sons Ltd; 2001.
2. Slichter CP. Principles of magnetic resonance. Berlin: Springer-Verlag; 1996.
3. Haacke ME, Brown RW, Thompson MR, Venkatesan R. Magnetic resonance imaging: physical principles and sequence design. New York: Wiley-Liss; 1999.
4. Bernstein MA, King KF, Zhou XJ. Handbook of MRI pulse sequences. Burlington, MA: Elsevier Academic Press; 2004.
5. Nishimura DG. Principles of Magnetic Resonance Imaging; 1996.
6. Pauly J, LeRoux P, Nishimura D, Macovski A. Parameter relations for the Shinnar-Le Roux selective excitation pulse design algorithm. IEEE T Med Imaging 1991;10:53-65.
7. Pauly J, Nishimura D, Macovski A. A k-space analysis of small-tip-angle excitation. J Magn Reson 1989;81:43-56.
8. Abragam A, Goldman M. Principles of dynamic nuclear polarisation. Rep Prog Phys 1978;41:395-467.
9. Ardenkjaer-Larsen JH, Fridlund B, Gram A, Hansson G, Hansson L, Lerche MH, Servin R, Thaning M, Golman K. Increase in signal-to-noise ratio of > 10,000 times in liquid-state NMR. Proc Natl Acad Sci USA 2003;100:10158-10163.
10. Wolber J, Ellner F, Fridlund B, Gram A, Johannesson H, Hansson G, Hansson LH, Lerche MH, Mansson S, Servin R, Thaning M, Golman K, Ardenkjaer-Larsen JH. Generating highly polarized nuclear spins in solution using dynamic nuclear polarization. Nucl Instr Meth Phys Res A 2004;526:173-181.
11. Cunningham CH, Chen AP, Albers MJ, Kurhanewicz J, Hurd RE, Yen Y, Pauly JM, Nelson SJ, Vigneron DB. Double spin-echo sequence for rapid spectroscopic imaging of hyperpolarized ^{13}C . J Magn Reson 2007;187:357-362.
12. Cunningham CH, Vigneron DB, Chen AP, Xu D, Nelson SJ, Hurd RE, Kelley DA, Pauly JM. Design of flyback echo-planar readout gradients for magnetic resonance spectroscopic imaging. Magn Reson Med 2005;54:1286-1289.
13. Yen Y, LeRoux P, Bok R, Tropp J, Chen A, Zhang V, Zierhut M, Albers M, Park I, Nelson S, Vigneron D, Kurhanewicz J, Hurd R. Apparent T_2 of ^{13}C -labeled metabolites *in vivo*. 2008; Toronto. Proc Intl Soc Magn Reson Med.
14. Day SE, Kettunen MI, Gallagher FA, Hu DE, Lerche M, Wolber J, Golman K, Ardenkjaer-Larsen JH, Brindle KM. Detecting tumor response to treatment using hyperpolarized ^{13}C magnetic resonance imaging and spectroscopy. Nat Med 2007;13:1382-1387.
15. Chen AP, Albers MJ, Cunningham CH, Kohler SJ, Yen Y-F, Hurd RE, Tropp J, Bok R, Pauly JM, Nelson SJ, Kurhanewicz J, Vigneron DB. Hyperpolarized C-13 spectroscopic imaging of the TRAMP mouse at 3T—initial experience. Magn Reson Med 2007;58:1099-1106.
16. Albers MJ, Bok R, Chen AP, Cunningham CH, Zierhut ML, Zhang VY, Kohler SJ, Tropp J, Hurd RE, Yen Y-F, Nelson SJ, Vigneron DB, Kurhanewicz J.

- Hyperpolarized ^{13}C lactate, pyruvate, and alanine: noninvasive biomarkers for prostate cancer detection and grading. *Cancer Res* 2008;68:8607-8615.
17. Park I, Larson PEZ, Zierhut ML, Hu S, Bok R, Ozawa T, Kurhanewicz J, Vigneron DB, VandenBerg SR, James CD, Nelson SJ. Hyperpolarized ^{13}C MR metabolic imaging: application to brain tumors. *Neuro-oncology* 2009;(In Press).
 18. Gatenby RA, Gillies RJ. Why do cancers have high aerobic glycolysis? *Nat Rev Cancer* 2004;4:891-899.
 19. DeBerardinis RJ, Lum JJ, Hatzivassiliou G, Thompson CB. The biology of cancer: metabolic reprogramming fuels cell growth and proliferation. *Cell Metab* 2008;7:11-20.
 20. Li X, Vigneron DB, Cha S, Graves EE, Crawford F, Chang SM, Nelson SJ. Relationship of MR-derived lactate, mobile lipids, and relative blood volume for gliomas *in vivo*. *AJNR Am J Neuroradiol* 2005;26:760-769.
 21. Saraswathy S, Crawford FW, Lamborn KR, Pirzkall A, Chang S, Cha S, Nelson SJ. Evaluation of MR markers that predict survival in patients with newly diagnosed GBM prior to adjuvant therapy. *J Neurooncol* 2009;91:69-81.
 22. Golman K, Ardenkjaer-Larsen JH, Petersson JS, Mansson S, Leunbach I. Molecular imaging with endogenous substances. *Proc Natl Acad Sci USA* 2003;100:10435-10439.
 23. Golman K, Zandt R, Thaning M. Real-time metabolic imaging. *Proc Natl Acad Sci USA* 2006;103:11270-11275.
 24. Kohler SJ, Yen Y, Wolber J, Chen AP, Albers MJ, Bok R, Zhang V, Tropp J, Nelson SJ, Vigneron DB, Kurhanewicz J, Hurd RE. *In vivo* ^{13}C carbon metabolic imaging at 3T with hyperpolarized ^{13}C -1-pyruvate. *Magn Reson Med* 2007;58:65-69.
 25. Candes E, Romberg J, Tao T. Robust uncertainty principles: exact reconstruction from highly incomplete information. *IEEE Trans Inform Theory* 2006;52:489-509.
 26. Donoho DL. Compressed sensing. *IEEE Trans Inform Theory* 2006;52:1289-1306.
 27. Candes E, Romberg J. Signal recovery from random projections. *Proc SPIE-IS&T* 2005;5674:76-86.
 28. Tsaig Y, Donoho DL. Extensions of compressed sensing. *Signal Processing* 2006;86:549-571.
 29. Lustig M, Donoho DL, Pauly JM. Sparse MRI: the application of compressed sensing for rapid MR imaging. *Magn Reson Med* 2007;58:1182-1195.
 30. Mayer D, Levin YS, Hurd RE, Glover GH, Spielman DM. Fast metabolic imaging of systems with sparse spectra: application for hyperpolarized ^{13}C imaging. *Magn Reson Med* 2006;56:932-937.
 31. Levin YS, Mayer D, Hurd RE, Spielman DM. Optimization of fast spiral chemical shift imaging using least squares reconstruction: application for hyperpolarized ^{13}C metabolic imaging. *Magn Reson Med* 2007(58):245-252.
 32. Gull SF, Daniell GJ. Image reconstruction from incomplete and noisy data. *Nature* 1978;272:686-690.

33. Hoch JC, Stern AC. Maximum entropy reconstruction in NMR. In: Grant DM, Harris RK, editors. Encyclopedia of NMR. New York: John Wiley and Sons; 1996.
34. Newman RH. Maximization of entropy and minimization of area as criteria for NMR signal processing. *J Magn Reson* 1988;79:448-460.
35. Stern AS, Donoho DL, Hoch JC. NMR data processing using iterative thresholding and minimum l1-norm reconstruction. *J Magn Reson* 2007;188:295-300.
36. Lustig M, Santos JM, Donoho DL, Pauly JM. k-t Sparse: high frame rate dynamic MRI exploiting spatio-temporal sparsity. 2006; Seattle. Proceedings of the International Society of Magnetic Resonance in Medicine.
37. Jung H, Ye J, Kim EY. Improved k-t BLAST and k-t SENSE using FOCUSS. *Phys Med Biol* 2007;52:3201-3226.
38. Duyn JH, Yang Y, Frank JA, vanderVeen JW. Simple correction method for k-space trajectory deviations in MRI. *J Magn Reson* 1998;132:150-153.
39. Kerr A, Pauly J, Nishimura D. Eddy current characterization and compensation in spiral and echo-planar imaging. 1996; New York. Proc Intl Soc Magn Reson Med.
40. Zhao L, Mulkern R, Tseng C, Williamson D, Patz S, Kraft R, Walsworth RL, Jolesz FA, Albert MS. Gradient-echo imaging considerations for hyperpolarized ^{129}Xe MR. *J Magn Reson B* 1996;113:179-183.
41. Nelson SJ. Analysis of volume MRI and MR spectroscopic imaging data for the evaluation of patients with brain tumors. *Magn Reson Med* 2001;46:228-239.
42. Greenberg NM, DeMayo F, Finegold MJ, Medina D, Tilley WD, Aspinall JO, Cunha GR, Donjacour AA, Matusik RJ, Rosen JM. Prostate cancer in a transgenic mouse. *Proc Natl Acad Sci USA* 1995;92:3439-3443.
43. Kaplan-Lefko PJ, Chen TM, Ittmann MM, Barrios RJ, Ayala GE, Huss WJ, Maddison LA, Foster BA, Greenberg NM. Pathobiology of autochthonous prostate cancer in a pre-clinical transgenic mouse model. *Prostate* 1993;55:219-237.
44. Chen S, Donoho DL, Saunders M. Atomic decomposition by basis pursuit. *SIAM J Sci Comput* 1999;20:33-61.
45. Ahmed OA. New denoising scheme for magnetic resonance spectroscopy signals. *IEEE T Med Imaging* 2005;24:809-816.
46. Trbovic N, Dancea F, Langer T, Gunther U. Using wavelet de-noised spectra in NMR screening. *J Magn Reson* 2005;173:280-287.
47. Dancea F, Gunther U. Automated protein NMR structure determination using wavelet de-noised NOESY spectra. *J Biomol NMR* 2005;33:139-152.
48. Candes EJ, Romberg JK, Tao T. Stable signal recovery from incomplete and inaccurate measurements. *Commun Pur Appl Math* 2006;59:1207-1223.
49. Haupt J, Nowak R. Signal reconstruction from noisy random projections. *IEEE Trans Inform Theory* 2006;52:4036-4048.
50. Gruetter R, Adriany G, Choi I-Y, Henry P-G, Lei H, Oz G. Localized in vivo ^{13}C NMR spectroscopy of the brain. *NMR Biomed* 2003;16:313-338.
51. deGraaf RA, Mason GF, Patel AB, Behar KL, Rothman DL. *In vivo* ^1H - ^{13}C -NMR spectroscopy of cerebral metabolism. *NMR Biomed* 2003;16:339-357.

52. Ross B, Lin A, Harris K, Bhattacharya P, Schweinsburg B. Clinical experience with ^{13}C MRS *in vivo*. NMR Biomed 2003;16:358-369.
53. Johansson E, Mansson S, Wirestam R, Svensson J, Petersson JS, Golman K, Stahlberg F. Cerebral perfusion assessment by bolus tracking using hyperpolarized ^{13}C . Magn Reson Med 2004;51:464-472.
54. Golman K, Zandt RI, Lerche M, Pehrson R, Ardenkjaer-Larsen JH. Metabolic imaging by hyperpolarized ^{13}C magnetic resonance imaging for *in vivo* tumor diagnosis. Cancer Res 2006;66:10855-10860.
55. Board M, Humm S, Newsholme E. Maximum activities of key enzymes of glycolysis, glutaminolysis, pentose phosphate pathway and tricarboxylic acid cycle in normal, neoplastic and suppressed cells. Biochem J 1990;265:503-509.
56. Merritt ME, Harrison C, Storey C, Jeffrey FM, Sherry AD, Malloy CR. Hyperpolarized ^{13}C allows a direct measure of flux through a single enzyme-catalyzed step by NMR. Proc Natl Acad Sci USA 2007;104:19773-19777.
57. Schroeder MA, Cochlin LE, Heather LC, Clarke K, Radda GK, Tyler DJ. *In vivo* assessment of pyruvate dehydrogenase flux in the heart using hyperpolarized carbon-13 magnetic resonance. Proc Natl Acad Sci USA 2008;105:12051-12056.
58. Golman K, Peterson JS. Metabolic imaging and other applications of hyperpolarized ^{13}C . Acad Radiol 2006;13:932-942.
59. Chen AP, Kurhanewicz J, Bok R, Xu D, Joun D, Zhang V, Nelson SJ, Hurd RE, Vigneron DB. Feasibility of using hyperpolarized [^{13}C]lactate as a substrate for *in vivo* metabolic ^{13}C MRSI studies. Magn Reson Imaging 2008;26:721-726.
60. Gallagher FA, Kettunen MI, Day SE, Hu D-E, Ardenkjaer-Larsen JH, Zandt Rit, Jensen PR, Karlsson M, Golman K, Lerche MH, Brindle KM. Magnetic resonance imaging of pH *in vivo* using hyperpolarized ^{13}C -labelled bicarbonate. Nature 2008;453:940-944.
61. Gillies RJ, Raghunand N, Garcia-Martin ML, Gatenby RA. pH imaging: a review of pH measurement methods and applications in cancers. IEEE Eng Med Biol 2004;23:57-64.
62. Reddy KR, Faust T. The clinician's guide to liver disease. Thorofare, NJ: SLACK Incorporated; 2006.
63. Derby K, Tropp J, Hawryszko C. Design and evaluation of a novel dual-tuned resonator for spectroscopic imaging. J Magn Reson 1990;86:645-651.
64. Felig P. The glucose-alanine cycle. Metab 1973;22:179-207.
65. Cohen SM. ^{13}C and ^{31}P NMR study of gluconeogenesis: utilization of ^{13}C -labeled substrates by perfused liver from streptozotocin-diabetic and untreated rats. Biochem 1987;26:563-572.
66. Cohen SE. ^{13}C NMR study of effects of fasting and diabetes on the metabolism of pyruvate in the tricarboxylic acid cycle and of the utilization of pyruvate and ethanol in lipogenesis in perfused rat liver. Biochem 1987;26:581-589.
67. Stromski ME, Arias-Mendoza F, Alger JR, Shulman RG. Hepatic gluconeogenesis from alanine: ^{13}C nuclear magnetic resonance methodology for *in vivo* studies. Magn Reson Med 1986;3:24-32.

68. Giboney PT. Mildly elevated liver transaminase levels in the asymptomatic patient. *Am Fam Physician* 2005;71:1105-1110.
69. Merritt ME, Harrison C, Storey C, Sherry AD, Malloy CR. Inhibition of Carbohydrate Oxidation During the First Minute of Reperfusion After Brief Ischemia: NMR Detection of Hyperpolarized $^{13}\text{CO}_2$ and $\text{H}^{13}\text{CO}_3^-$. *Magn Reson Med* 2008;60:1029-1036.
70. Gallagher FA, Kettunen MI, Day SE, Lerche M, Brindle KM. ^{13}C MR spectroscopy measurements of glutaminase activity in human hepatocellular carcinoma cells using hyperpolarized ^{13}C -labeled glutamine. *Magn Reson Med* 2008;60:253-257.
71. Hu S, Lustig M, Chen AP, Crane J, Kerr A, Kelley DAC, Hurd R, Kurhanewicz J, Nelson SJ, Pauly JM, Vigneron DB. Compressed sensing for resolution enhancement of hyperpolarized ^{13}C flyback 3D-MRSI. *J Magn Reson* 2008;192:258-264.
72. Candes EJ, Wakin MB, Boyd SP. Enhancing sparsity by reweighted l1 minimization. *J Fourier Anal Appl* 2008;14:877-905.
73. Ardenkjaer-Larsen JH, Macholl S, Johannesson H. Dynamic nuclear polarization with Trityls at 1.2 K. *Appl Magn Reson* 2008;34:509-522.
74. Shachaf CM, Kopelman AM, Arvanitis C, Karlsson A, Beer S, Mandl S, Bachmann MH, Borowsky AD, Ruebner B, Cardiff RD, Yang Q, Bishop JM, Contag CH, Felsher DW. MYC inactivation uncovers pluripotent differentiation and tumour dormancy in hepatocellular cancer. *Nature* 2004;431:1112-1117.
75. Goga A, Yang D, Tward AD, Morgan DO, Bishop JM. Inhibition of CDK1 as a potential therapy for tumors over-expressing MYC. *Nature Med* 2007;13:820-827.
76. Carr BI. *Hepatocellular Cancer*. Totowa, New Jersey: Humana Press; 2005.
77. Tommasi S, Pinto R, Pilato B, Paradiso A. Molecular pathways and related target therapies in liver carcinoma. *Current Pharmaceutical Design* 2007;13:3279-3287.
78. Leupold J, Mansson S, Petersson JS, Hennig J, Wieben O. Fast multiecho balanced SSFP metabolite mapping of ^1H and hyperpolarized ^{13}C compounds. *Magn Reson Mater Phy* 2009.
79. Mistretta CA, Wieben O, Velikina J, Block W, Perry J, Wu Y, Johnson K, Wu Y. Highly constrained backprojection for time-resolved MRI. *Magn Reson Med* 2006;55:30-40.
80. Mazzanti R, Gramantieri L, Bolondi L. Hepatocellular carcinoma: epidemiology and clinical aspects. *Mol Aspects of Med* 2008;29:130-143.
81. El-Serag HB, Rudolph KL. Hepatocellular carcinoma: epidemiology and molecular carcinogenesis. *Gastroenterology* 2007;132:2557-2576.
82. Llovet JM, Bruix J. Molecular targeted therapies in hepatocellular carcinoma. *Hepatology* 2008;48:1312-1327.
83. Therasse P, Arbuck SG, Eisenhauer EA, Wanders J, Kaplan RS, Rubinstein L, Verweij J, Glabbeke MV, Oosterom ATv, Christian MC, Gwyther SG. New guidelines to evaluate the response to treatment in solid tumors. *J Natl Cancer Inst* 2000;92:205-216.

84. Brindle K. New approaches for imaging tumour responses to treatment. *Nat Rev Cancer* 2008;8:94-107.
85. Schelling M, Avril N, Nahrig J, Kuhn W, Romer W, Sattler D, Werner M, Dose J, Janicke F, Graeff H, Schwaiger M. Positron emission tomography using [¹⁸F]fluorodeoxyglucose for monitoring primary chemotherapy in breast cancer. *J Clin Oncol* 2000;18:1689-1695.
86. Spaepen K, Stroobants S, Dupont P, Steenweghen SV, Thomas J, Vandenberghe P, Vanuytsel L, Bormans G, Balzarini J, Wolf-Peeters CD, Mortelmans L, Verhoef G. Prognostic value of positron emission tomography (PET) with fluorine-18 fluorodeoxyglucose ([¹⁸F]FDG) after first-line chemotherapy in non-Hodgkin's lymphoma: is [¹⁸F]FDG-PET a valid alternative to conventional diagnostic methods? *J Clin Oncol* 2001;19:414-419.
87. Weber WA, Ott K, Becker K, Dittler H-J, Helmberger H, Avril NE, Meisetschlager G, Busch R, Siewert J-R, Schwaiger M, Fink U. Prediction of response to preoperative chemotherapy in adenocarcinomas of the esophagogastric junction by metabolic imaging. *J Clin Oncol* 2001;19:3058-3065.
88. Weber WA, Petersen V, Schmidt B, Tyndale-Hines L, Link T, Peschel C, Schwaiger M. Positron emission tomography in non-small-cell lung cancer: prediction of response to chemotherapy by quantitative assessment of glucose use. *J Clin Oncol* 2003;21:2651-2657.
89. Avril N, Sassen S, Schmalfeldt B, Naehrig J, Rutke S, Weber WA, Werner M, Graeff H, Schwaiger M, Kuhn W. Prediction of response to neoadjuvant chemotherapy by sequential F-18-fluorodeoxyglucose positron emission tomography in patients with advanced-stage ovarian cancer. *J Clin Oncol* 2005;23:7445-7453.
90. Schaftingen EV, Gerin I. The glucose-6-phosphatase system. *Biochem J* 2002;362:513-532.
91. Takahashi N, Inoue T, Lee J, Yamaguchi T, Shizukuishi K. The roles of PET and PET/CT in the diagnosis and management of prostate cancer. *Oncology* 2007;72:226-233.
92. Chen W, Cloughesy T, Kamdar N, Satyamurthy N, Bergsneider M, Liao L, Mischel P, Czernin J, Phelps ME, Silverman DHS. Imaging proliferation in brain tumors with ¹⁸F-FLT PET: comparison with ¹⁸F-FDG. *J Nucl Med* 2005;46:945-952.
93. Okazumi S, Isono K, Enomoto K, Kikuchi T, Ozaki M, Yamamoto H, Hayashi H, Asano T, Ryu M. Evaluation of liver tumors using fluorine- 18-fluorodeoxyglucose PET: characterization of tumor and assessment of effect of treatment. *J Nucl Med* 1992;33:333-339.
94. Khan MA, Combs CS, Brunt EM, Lowe VJ, Wolverson MK, Solomon H, Collins BT, Bisceglie AMD. Positron emission tomography scanning in the evaluation of hepatocellular carcinoma. *J Hepatol* 2000;32:792-797.
95. Sureshbabu W, Mawlawi O. PET/CT imaging artifacts. *J Nucl Med Technol* 2005;33:156-161.

96. Kurhanewicz J, Vigneron DB, Nelson SJ. Three-dimensional magnetic resonance spectroscopic imaging of brain and prostate cancer. *Neoplasia* 2000;2:166-189.
97. Wierstra I, Alves J. The c-myc promoter: still MysterY and challenge. *Adv Cancer Res* 2008;99:113-333.
98. Thorgeirsson SS, Grisham JW. Molecular pathogenesis of human hepatocellular carcinoma. *Nat Genet* 2002;31:339-346.
99. Lee J-S, Chu I-S, Mikaelyan A, Calvisi DF, Heo J, Reddy JK, Thorgeirsson SS. Application of comparative functional genomics to identify best-fit mouse models to study human cancer. *Nat Genet* 2004;36:1306-1311.
100. Shim H, Dolde C, Lewis BC, Wu CS, Dang G, Jungmann RA, Dalla-Favera R, Dang CV. c-Myc transactivation of LDH-A: Implications for tumor metabolism and growth. *Proc Natl Acad Sci USA* 1997;94:6658-6663.
101. Hu S, Lustig M, Balakrishnan A, Larson PEZ, Bok R, Kurhanewicz J, Nelson SJ, Goga A, John M. Pauly, Vigneron DB. 3D Compressed Sensing for Highly Accelerated Hyperpolarized ^{13}C MRSI with *In Vivo* Applications to Transgenic Mouse Models of Cancer. *Magn Reson Med* 2009;In Press.
102. Hu S, Chen AP, Zierhut ML, Bok R, Yen Y-F, Schroeder MA, Hurd RE, Nelson SJ, Kurhanewicz J, Vigneron DB. *In vivo* carbon-13 dynamic MRS and MRSI of normal and fasted rat liver with hyperpolarized ^{13}C -pyruvate. *Mol Imaging Biol* 2009.
103. Newell P, Villanueva A, Friedman SL, Koike K, Llovet JM. Experimental models of hepatocellular carcinoma. *J Hepatol* 2008;48:858-879.
104. Zandt R, Kettunen M, Karlsson M, Jensen PR, Gisselsson A, Gallagher F, Hu D, Hansson G, Brindle K, Lerch M. ^{13}C -Labeled Malate as a Treatment Response Marker in a Murine Lymphoma Model *In Vivo*. 2009; Honolulu. *Proc Intl Soc Magn Reson Med*.
105. Keshari KR, Wilson DM, Chen AP, Bok R, Larson PEZ, Hu S, Macdonald JM, Vigneron DB, Kurhanewicz J. Hyperpolarized [2- ^{13}C]-Fructose: A New DNP Substrate for *In Vivo* Metabolic Imaging. (Manuscript to be Submitted) 2009.
106. Tannus A, Garwood M. Adiabatic pulses. *NMR Biomed* 1997;10:423-434.
107. Norris DG. Adiabatic radiofrequency pulse forms in biomedical nuclear magnetic resonance. *Concept Magn Reson* 2002;14:89-101.
108. Park J, DelaBarre L, Garwood M. Improved gradient-echo 3D magnetic resonance imaging using pseudo-echoes created by frequency-swept pulses. *Magn Reson Med* 2006;55:848-857.

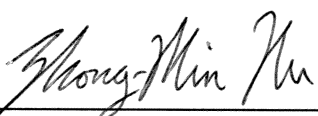
UCSF Library Release

Publishing Agreement

It is the policy of the University to encourage the distribution of all theses and dissertations. Copies of all UCSF theses and dissertations will be routed to the library via the Graduate Division. The library will make all theses and dissertations accessible to the public and will preserve these to the best of their abilities, in perpetuity.

Please sign the following statement:

I hereby grant permission to the Graduate Division of the University of California, San Francisco to release copies of my thesis or dissertation to the Campus Library to provide access and preservation, in whole or in part, in perpetuity.



Author Signature

10/1/09
Date